MECHANISTIC MODELING OF EVAPORATING THIN LIQUID FILM INSTABILITY ON A BWR FUEL ROD WITH PARALLEL AND CROSS VAPOR FLOW

A Thesis
Presented to
The Academic Faculty

by

Chih-Chieh Hu

In Partial Fulfillment
of the Requirements for the Degree
Doctor of Philosophy in the
School of Mechanical Engineering

Georgia Institute of Technology
May 2009

MECHANISTIC MODELING OF EVAPORATING THIN LIQUID FILM INSTABILITY ON A BWR FUEL ROD WITH PARALLEL AND CROSS VAPOR FLOW

Approved by:

Dr. Said I. Abdel-Khalik, Advisor
School of Mechanical Engineering
Georgia Institute of Technology

Dr. S. Mostafa Ghiaasiaan
School of Mechanical Engineering
Georgia Institute of Technology

Dr. Nolan E. Hertel
School of Mechanical Engineering
Georgia Institute of Technology

Dr. Yingjie Liu
School of Mathematics
Georgia Institute of Technology

Dr. Mostafa H. Ammar
College of Computing
Georgia Institute of Technology

Date Approved: December 8, 2008

To my family, teachers, and friends

ACKNOWLEDGEMENTS

I deeply appreciate my advisor, Dr. Said Abdel-Khalik, for the invaluable advice and support that I received from him. I admire his wisdom and vision for education. I would like to thank Dr. Seungwon Shin for his advice, endless help, and encouragement. He provided his computers so that I could finish the simulation. He also deserves recognition for developing the Level Contour Reconstruction Method. I would also like to thank Dr. Yinjie Liu for sharing his Back and Forth Error Compensation and Correction method along with many other numerical schemes. In addition, I am grateful to Dr. S. Mostafa Ghiaasiaan for valuable comments and assistance in the two-phase model. I would like to thank the other members of my thesis committee, Dr. Mostafa H. Ammar and Dr. Nolan E. Hertel, for their recommendations.

Martin Sanchez-Rocha, Drs. Shenq-Yuh Jaw, Roberto Verzicco, Mark K. Smith, and David Wilcox provided very valuable information about the CFD models.

I am very grateful to Mr. Dennis L. Sadowski for his encouragement. I would also like to thank my laboratory colleagues, Dr. Lorenzo Crosatti, Libby Gayton, Joshua Hawkes, Frank Hope, Dr. Tim Koehler, Dr. Celine Lascar, Bo Lu, Dr. Vladimir Novak, and Brandon Weathers, who made this journey enjoyable. Ms. Jane Chisholm and Dr. Jeffery A. Donnell provided valuable assistance in the writing of the thesis. Many thanks go out to the staff in mechanical engineering.

I wish to express my deep appreciation to my parents and all my relatives. I would like to thank my wife, Lan Wu, for her love, understanding, and care. Without her

support, this dissertation would not have been possible. I am grateful to my daughter, Megan, who brings immerse joy to our family.

TABLE OF CONTENTS

LIST OF TABLES

LIST OF FIGURES

Page

NOMENCLATURE

c	specific heat (J/kg k)
D	diameter
g	gravity
I	indicator function
I_{opt}	optimum value of reconstruction
k	turbulent kinetic energy
$\dot{m}_f$	interfacial mass flux
n	normal vector
P	pressure
q	heat flux
r	radial coordinate
Re	Reynolds number
T	temperature
t	time (s)
tk	thermal conductivity (W/mk)
u	fluid velocity vector
u	velocity in r direction
v	velocity in θ direction
w	velocity in z direction
z	axial coordinate

Greek Letters

μ	dynamic viscosity

σ	surface tension (N/m)
ρ	density (kg/m^3)
δ	dirac delta function
κ	curvature
τ	liquid film thickness

Superscript

+	non-dimensional quantity

SUMMARY

This work has been aimed at developing a mechanistic, transient, 3-D numerical model to predict the behavior of an evaporating thin liquid film on a non-uniformly heated cylindrical rod with simultaneous parallel and cross flow of vapor. Interest in this problem has been motivated by the fact that the liquid film on a full-length boiling water reactor fuel rod may experience significant axial and azimuthal heat flux gradients and cross flow due to variations in the thermal-hydraulic conditions in surrounding subchannels caused by proximity to inserted control blade tip and/or the top of part-length fuel rods. Such heat flux gradients coupled with localized cross flow may cause the liquid film on the fuel rod surface to rupture, thereby forming a dry hot spot. These localized dryout phenomena can not be accurately predicted by traditional subchannel analysis methods in conjunction with empirical dryout correlations. To this end, a numerical model based on the Level Contour Reconstruction Method was developed. The Standard k-ε turbulence model is included. A cylindrical coordinate system has been used to enhance the resolution of the Level Contour Reconstruction Model. Satisfactory agreement has been achieved between the model predictions and experimental data.

A model of this type is necessary to supplement current state-of-the-art BWR core thermal-hydraulic design methods based on subchannel analysis techniques coupled with empirical dry out correlations. In essence, such a model would provide the core designer with a "magnifying glass" by which the behavior of the liquid film at specific locations within the core (specific axial node on specific location within a specific bundle in the subchannel analysis model) can be closely examined. A tool of this type would allow the

designer to examine the effectiveness of possible design changes and/or modified control strategies to prevent conditions leading to localized film instability and possible fuel failure.

CHAPTER 1

INTRODUCTION

1.1 Overview

Multi-phase flow is a ubiquitous process with many important engineering applications. A variety of numerical techniques have been inspired by, and developed for, the direct simulation of such flows. The use of a fixed Eulerian grid to represent the velocity field with additional advection schemes to preserve the sharpness of interfacial fronts has become increasingly popular. Numerical approaches developed to mechanistically model the behavior of two-phase flow include the volume-of-fluid (VOF), level set, and front tracking methods. Recent comprehensive reviews of these numerical techniques can be found in Glimm et al.(1998), Scardovelli and Zaleski (1999), Osher and Fedkiw (2001), Jamet et al.(2001), and Tryggvason et al.(2001). These methods have been widely used to model a variety of two-phase flows involving drops, bubbles, and particles. Each of them has some advantage over the others and has offered varying degrees of success in modeling general multiphase problems. During the past several years, efforts at Georgia Tech have focused on the development of a simplified front tracking method, called the Level Contour Reconstruction Method (LCRM) (Shin and Juric, 2002, Shin et al., 2005a, 2005b, Shin and Abdel-Khalik, 2007), which does not have logical connectivity and thus eliminates the associated algorithmic burden in the original front tracking method while retaining the accuracy and advantages of explicit

Lagrangian surface tracking. A primary advantage of the Level Contour Reconstruction Method is the ability to naturally and automatically handle interface merging and breakup in 3D flows which was extremely difficult in the original front tracking method.

The behavior of a thin liquid film flowing along a solid wall has numerous engineering applications ranging from surface coating to cooling of nuclear reactor cores. The problem is readily amenable to analysis using LCRM. Our interest in this problem derives from earlier work on modeling of annular two-phase flow in boiling water reactors (BWRs). A boiling water reactor contains several hundred fuel assemblies. Fuel assemblies may contain several part length fuel rods to enhance moderation in the upper regions of the core and improve fuel utilization (Figure 1.1) depending on venders. The active length of full length fuel rods is about 3.6 meters. It has been hypothesized that some recent BWR fuel failures following control rod maneuvers may have been caused by liquid film instability in regions of localized cross flow and high heat flux gradients. Specifically, the liquid film flowing upwards along a full-length fuel rod in the upper regions of the core may experience significant azimuthal and axial heat flux gradients and cross flow caused by variations in the thermal-hydraulic conditions in the surrounding subchannels caused by proximity to an inserted control blade tip and/or sudden change in geometry at the top of neighboring part-length rods. The heat flux gradients and cross flow may cause the liquid water film on the fuel rod surface to rupture, thereby forming a dry hot spot (Figure 1.2). Such localized dryout phenomena cannot be accurately predicted by current core design methods based on subchannel analysis techniques coupled with empirical dryout correlations.

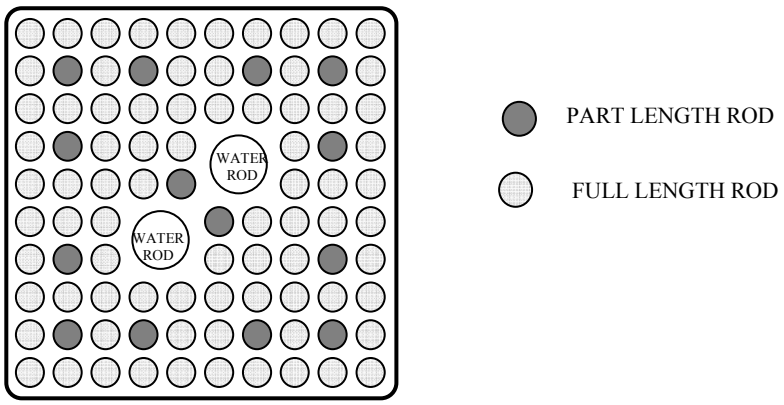

Figure 1.1: Schematic of a BWR fuel assembly cross section

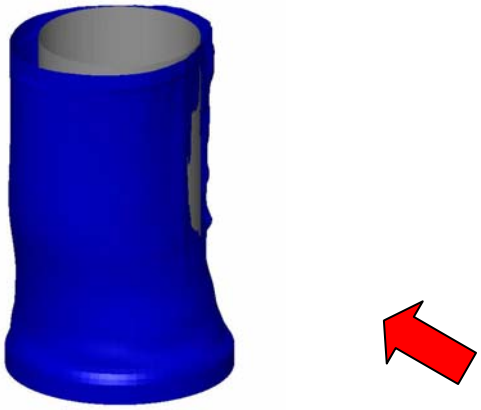

Figure 1.2: Liquid film dry patch formation under cross flow and high local heat flux conditions

To this end, this research has been undertaken to develop a numerical model by which the detailed three-dimensional behavior of the liquid film along a specific axial node of a specific fuel rod can be mechanistically modeled (Figure 1.3). The simulation region of LCRM encompasses one computational node in a subchannel analysis code (10

cm long subchannel). The model would supplement current subchannel analysis methods by allowing core designers to focus closely on specific areas of potential concern.

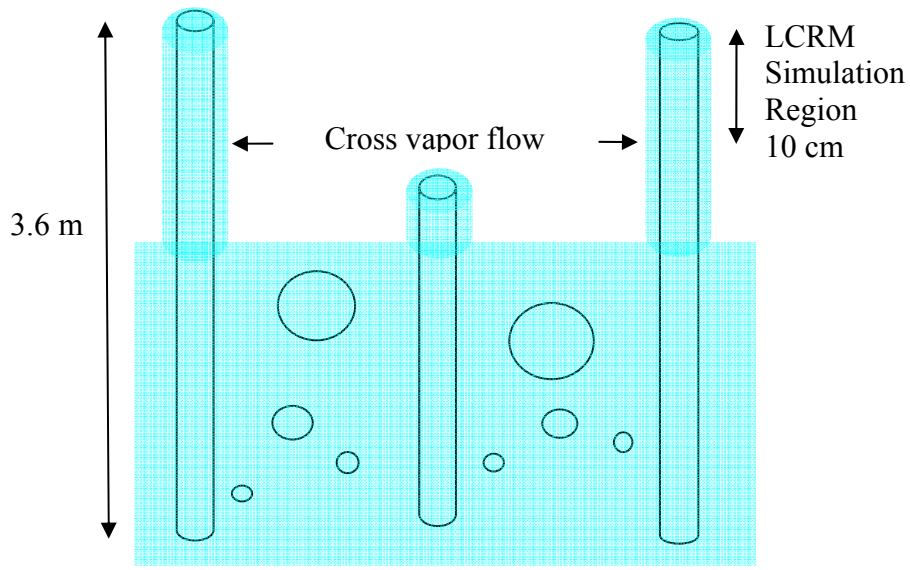

Figure 1.3: LCRM simulation region encompassing one subchannel analysis code computational node

Among the challenges presented by this problem is the ability to accurately represent the evolving liquid film interface despite the relatively coarse grid resolution necessitated by the three-dimensional nature of the problem. Additionally, operating conditions in current boiling water reactor cores produce turbulent flow in both the vapor core and liquid film in the upper regions of the core. Hence it is necessary to incorporate turbulent effects in the model. In this study, we present an algorithm for modeling the liquid-film-covered fuel rod geometry using a cylindrical coordinate system, in combination with Standard $k-\varepsilon$ turbulence model. The aim is to develop the means to

realistically simulate the behavior of an evaporating thin film on a cylindrical nuclear fuel rod surface using LCRM.

1.2 Critical Heat Flux

The critical heat flux (CHF) in a boiling system is the heat flux above which the surface temperature of the heated surface is expected to rapidly rise due to either departure from nucleate boiling (DNB) or liquid film dryout. If operated above the critical heat flux, fuel rod cladding in a nuclear reactor core would be damaged due to such high temperatures. Thus the critical heat flux has become one of the most important operational limits for nuclear reactor cores.

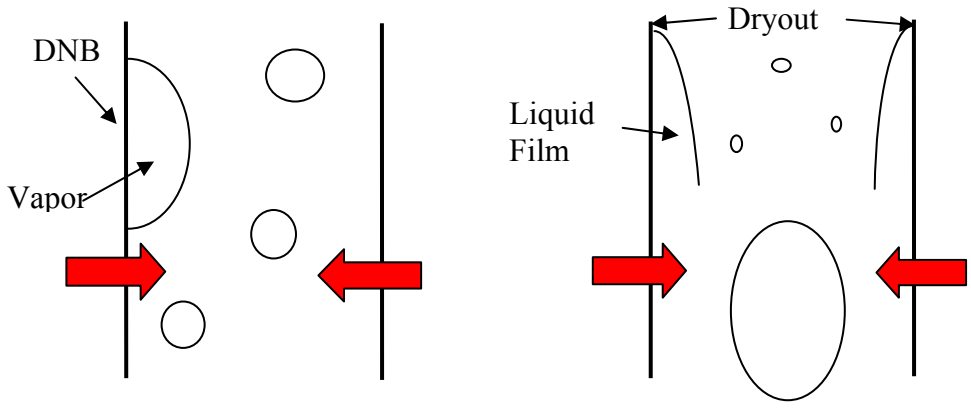

(a) DNB (b) Dryout

Figure 1.4: Schematic diagram of CHF (a) Departure from nucleate boiling (DNB) (b) Dryout.

It is generally agreed that there are two CHF mechanisms: departure from nucleate boiling (DNB) and dryout, as presented in Figures 1.4 (a) and (b), respectively. DNB can take place in either subcooled or saturated flow boiling at low vapor quality

(e.g. PWR hot channels), while dryout occurs in saturated flow boiling at high vapor quality (e.g. upper region of BWR cores). In DNB, a vapor film forms on the wall separating the liquid water from the heated surface, thereby increasing the wall temperature. Dryout, on the other hand, occurs in annular two-phase flow, where the thickness of the liquid film on the wall becomes very small due to evaporation so that it can no longer transfer the heat effectively from the wall.

Different models have been proposed to predict the critical heat flux. Kataoka et al. (1997) proposed a prediction model for DNB and dryout. Other dryout prediction models can be found in the work of Hewitt (1990) and Okawa (2003). In general, however, core designers rely on empirical correlations based on experimental data for the exact bundle geometries to be used. These correlations, however, may not fully capture the actual range of operating conditions, including axial and azimuthal variations in heat flux due to proximity of control rods as well as cross flow due to sudden geometry changes near the top of part length rods. Hence in this study we attempt to mechanistically model dryout using LCRM. LCRM allows us to track the liquid film evolution for different velocity and heat flux boundary conditions. This provides a way of predicting CHF under vapor cross flow and heat flux gradient.

1.3 Turbulence Modeling

Turbulent flow exists in numerous engineering applications including PWR and BWR reactors. Turbulent flow is dissipative. In turbulent flow, there are numerous eddies in the flow ranging in size from “large” eddies to “small” eddies (Figure 1.5). Large eddies transfer energy to smaller eddies. Smaller eddies break up and transfer energy to even smaller eddies. This process is repeated until the smallest scale, where the energy is

dissipated to heat by molecular viscosity. This process is often referred to energy cascade. In addition to the eddies, large scale motion exists in turbulent flow. The large scale motion with complex movement greatly influences the far field downstream conditions. The complex movement present in turbulent flow greatly enhances the transport of mass, momentum and energy, well above the rates achieved in laminar flow.

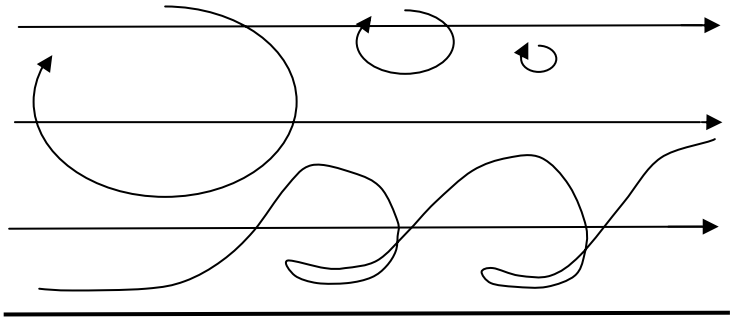

Figure 1.5: Turbulent flow contains large eddies and small eddies with varies length scale with complex movement

To understand turbulent flow, both simulation and experimental approaches are used. However, in many cases, experiments are limited by the ability to fully diagnose the conditions within a turbulent flow field. Some parameters of turbulent flow, for example the fluctuating pressure, are difficult to measure even by the most advanced equipment. Additionally, many experiments are costly. Hence, simulation has become an important approach for engineers to understand the behavior of turbulent flows.

Over the past few decades, several numerical methods have been developed for turbulent flow simulation, including direct numerical simulation (DNS), large-eddy simulation (LES), and solution of the Reynolds Averaged Navier-Stokes (RANS)

equations etc. In addition, statistical models of turbulent flow have been proposed (Pope, 2000). DNS solves the Navier-Stokes equations directly from large eddies to the smallest eddies. On the other hand, LES mainly simulates the large eddies while making some approximations for smaller eddies. Both DNS and LES need significant computer resources to run the calculation. For many engineering applications, the RANS method is adequate. The RANS model provides useful information while requiring considerably less time and resources. Hence, in this study, we employ the RANS method as the basis for our turbulence model.

Reynolds Averaged Navier-Stokes equations (RANS) are the averaged Navier-Stokes equations. In the averaging process, new parameters are introduced and additional turbulent flow information needs to be provided to close the equations. Zero-equation model, one-half-equation model, one-equation model, and two-equation model have been developed to provide the turbulent flow information according to the number of addition partial differential equations to be solved. The zero-equation model is built by assuming similarity of molecular motion and turbulent eddies. More recent work, however, uses one or two PDEs to model the turbulence. The most popular two-equation model is the Standard $k-\varepsilon$ Model, which was based on the work of Jones and Launder (1972) and Launder and Sharma (1974). The model includes two equations, one for "k", the turbulent kinetic energy, one for "ε", the dissipation rate, to close the RANS equations. Turbulent kinetic energy is related to the velocity scale, while the dissipation rate is related to the length scale. Generally one needs two scales to describe turbulence. Other two-equation turbulent flow models include the $k-\omega$ model (Wilcox, 1988) and SST model (Menter, 1992), which are used widely in aerospace engineering.

In the turbulent boundary layer, numerous experiments show that the time-smoothed velocity varies logarithmically with the normal distance from the wall (Wilcox, 2006). This "law of the wall" (Figure 1.6) is usually employed to resolve the velocity near the wall in the simulation without enough grid resolution. In our model, we use the law of the wall to set up the boundary conditions of turbulence kinetic energy and dissipation rate near the wall. Detail description of the numerical method for the Standard $k-\varepsilon$ Model will be presented in Chapter 3.

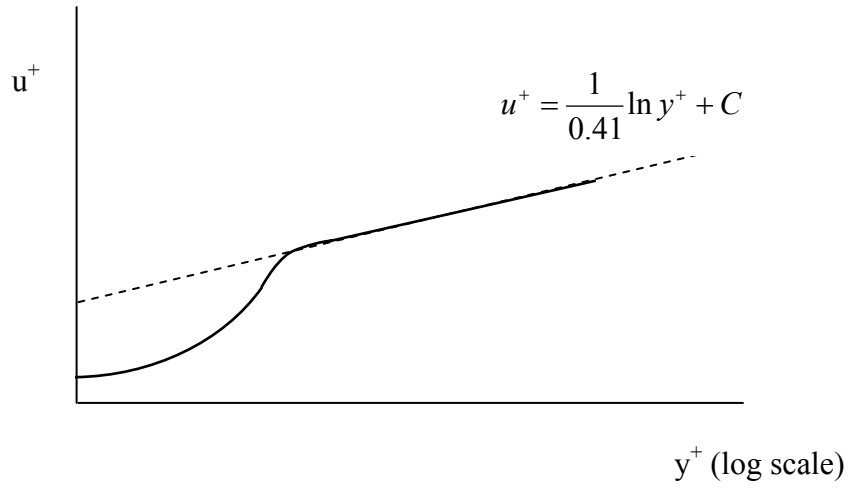

Figure 1.6: Law of the wall in turbulent flow

1.4 Objectives

The primary objective of this thesis project is to develop an experimentally-validated simulation tool to mechanically model the behavior of the evaporating liquid film surrounding a cylindrical fuel rod in a BWR using the Level Contour Reconstruction Method. This work builts on the work of Shin and Abdel-Khalik (2007) by changing the coordinate system of the fixed Eulerian grid in the LCRM to cylindrical coordinates in order to enhance the model resolution. More importantly, turbulence effects are included to more accurately simulate the velocity and temperature distributions at prototypical BWR operational conditions. Comparison is made between the model predictions and experimental data of critical heat flux on internally heated annuli. In addition to quantifying the effects of geometric and boundary conditions on dryout, the mechanistic model developed in this investigation allows one to quantify the effects of transient conditions on CHF. In nearly all transient analysis performed for reactor core design, steady state dryout correlations are used to establish the safety limits. This approach is used even in BWR stability transients where both reactor power and core flow undergo rapid oscillatory behavior. This practice is usually justified by the assertion that the use of such steady state correlation should yield conservative results. Data supporting such an assertion are not available. Therefore the model developed in this investigation will be used to examine the validity of such assertion.

The remainder of this thesis is organized as follows. Chapter 2 provides a literature review of numerical schemes used to model two-phase flow. The algorithm for solving the governing equations and description of Level Contour Reconstruction Method

are presented in Chapter 3. Chapter 4 provides the calculations performed to validate the model including comparisons with experimental data along with the results and discussion. Chapter 5 summarizes the conclusions of this thesis and offers suggestions for future research.

CHAPTER 2

LITERATURE REVIEW

Successful computational fluid dynamic (CFD) simulation requires an understanding of the numerical methods and physics of the flow, both of which cover a wide range of topics. Numerical methods include multiphase flow simulation, numerical solution of PDEs, grid generation, and turbulence simulation; the physics of the flow includes fluid mechanics, heat transfer, turbulent flow, and multiphase flow. The primary objective of this thesis is to develop an experimentally-validated simulation tool to mechanistically model the behavior of the evaporating liquid film surrounding a cylindrical rod in a BWR using the Level Contour Reconstruction Method. The literature review to be summarized in this chapter will cover some important topics relating to the simulation of the evaporating liquid film which leads to dryout in boiling water reactors.

2.1 Numerical Methods of Multiphase Flow Simulation

Direct simulation of multiphase flows is a very challenging problem. The multiphase flow behavior is highly dependent on the simultaneous coupling of unsteady mass, momentum, and energy transport with interfacial physics of surface tension, latent heat exchange, interphase mass transfer, discontinuous material properties, and complicated liquid-vapor interface dynamics. Over the past several decades, numerous techniques have been developed to simulate multiphase flow. These techniques include the volume-of-fluid (VOF), level set, and front tracking schemes. Recent comprehensive

reviews of these numerical techniques can be found in Scardovelli and Zaleski (1999), Osher and Fedkiw (2001), Jamet et al. (2001), Tryggvason et al. (2001), and Glimm et al. (1998). These methods have been widely used to model a variety of two-phase flows involving drops, bubbles, and particles. Each of them has some advantage over the others and has offered varying degrees of success in modeling general multiphase problems. A simple classification scheme of these methods can be made based on their computational grids. The volume-of-fluid (VOF) and level set method (LSM) employ a stationary grid to capture the interface. On the other hand, both front tracking and Level Contour Reconstruction Method (LCRM) use a Largrangian grid to track the interface, along with another stationary (Eulerian) grid for the fluid. As discussed in Tryggvason et al. (2001) front tracking has enjoyed considerable success in direct simulation of 2D, axisymmetric and 3D flow of drop and bubble dynamics. The Level Contour Reconstruction Method (LCRM) is essentially a hybrid between the level set and front tracking methods combining characteristics of both methods. In the following sections, we briefly review some of the main numerical schemes.

2.1.1 Volume-of-Fluid Method

The volume-of-fluid technique was introduced by Noh and Woodward (1976). This technique is often referred to by other names such as “the cell method” and “the method of partial fraction”. The basic idea is presented here. Referring to Figure 2.1a, a fixed grid on a two dimensional plane is shown with a curve representing the interface between the liquid and vapor. A number between 0 and 1 is assigned to each cell according to the volume fraction of that cell containing liquid inside the interface. A value of unity is assigned to the cells completely within the liquid area, while a value of

zero is assigned to the cells completely within the vapor area. Other cells encompassing the interface are assigned values between 0 and 1 depending on the volume fractions of the two phases. As the interface evolves, the volume fractions in the boundary nodes are adjusted as schematically shown in Figure 2.1b.

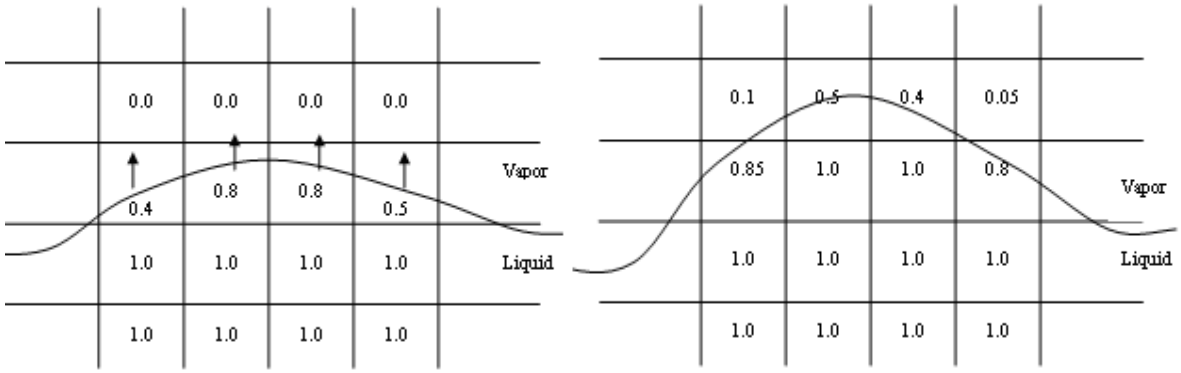

(a) (b)

Figure 2.1: Schematic representation of the volume-of-fluid method

Volume-of-fluid method preserves the mass of the fluid. The basic concept is easy to understand. However, it usually needs many cells to simulate the front since the volume fraction is not sufficiently accurate to capture the front. It is also hard to calculate the curvature and normal direction by volume fraction (Sethian, 1999). Much work is required to develope a higher order version. Readers are referred to Chorin (1980), Sethian (1984), and Puckett (1991) for additional details regarding volume-of-fluid methods.

2.1.2 Level Set Method (LSM)

The level set method (LSM) was first developed by Osher and Sethian in 1988. Since that time several review articles (Osher 2001) and books (Osher 2003, Sethian

1999) describing this technique have been published. One of the earliest attempts at using the LSM to solve two-phase flow problems was reported by Sussman et al. in 1994. Since that time this method has become increasingly popular due to its simplicity. Referring to Figure 2.2, consider a closed surface in two dimensions separating the entire domain into two regions, namely, inside and outside. In the level set method, the level set of a variable ϕ is used to represent the interface by ϕ =0.5. The region outside the boundary can be defined by ϕ =1, while the region inside the boundary is defined by ϕ =0. The variable ϕ is continuous and smooth. By solving the Navier-Stokes equation, the calculated velocity field can be used to advect the variable ϕ using the convection/advection equation.

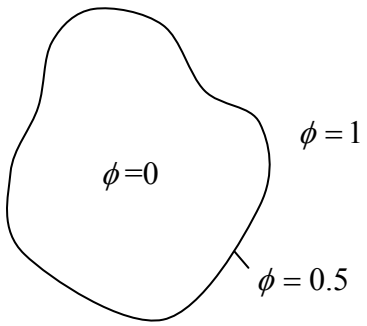

Figure 2.2: Schematic representation of the level set method

Solving the convection equation for ϕ allows the interface to be tracked. However, unlike the VOF method, the level set method is not naturally conservative, thus an extra mass conservation condition is required. Referring to Figure 2.3, the level set method is used to simulate a rising bubble. However without mass conservation, the

bubble shrinks as it continually loses mass. An additional mass conservation technique is needed to mitigate this mass loss problem. One simple mass conservation technique has been developed by Fukano et al. (2003). In addition to the convection equation, Eq. 2.1 is solved to a steady state.

$$\frac{\partial}{\partial t}\phi - (1 - \frac{A(t)}{A_o})|\nabla\phi| = 0\,. \qquad (2.1)$$

Here, A_0 denotes the total mass in the whole domain, while $A(t)$ is the total mass at time t. In Figure 2.4, the technique by Fukano and Inatomi (2003) is used to conserve the mass of a rising bubble.

The mass loss problem of the level set method stems from incorrectly deleting the characteristic information at some locations. In 2002, Enright et al. proposed the "particle level set method" to deal with the mass loss problem. This allows the level set method to obtain subgird scale accuracy near the interface and better mass conservation properties in under-resolved regions. The lack of connectivity between marker points makes the implementation much easier than front tracking and unsatisfactory description of the interface geometry can be obtained by using the level set function which maintains nice geometric properties. In Enright's method, marker points are placed randomly at inner and outer sides of the interface. The marker points are advected using the velocity field of the flow. Usually these marker points should not cross over the interface, from inner side to outer side or vice versa. However, when some marker points cross over the interface, it shows that the characteristic information has been deleted incorrectly. At that

time, the interface is reconstructed locally using the information associated with these marker points.

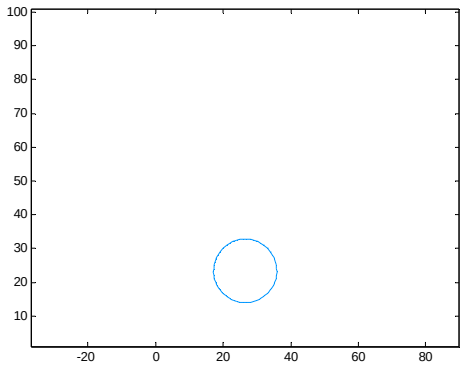

time 0 sec

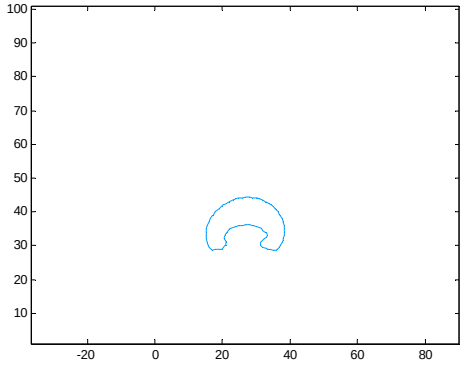

time 0.2 sec

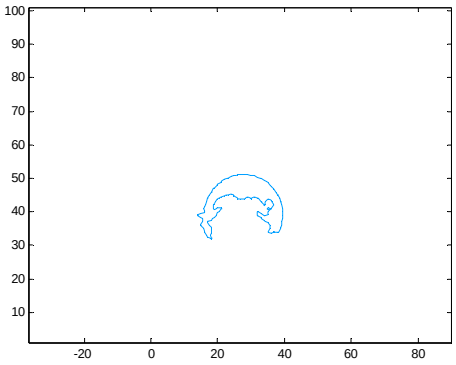

time 0.3 sec

Figure 2.3: Bubble rising simulation by level set method without mass conservation.

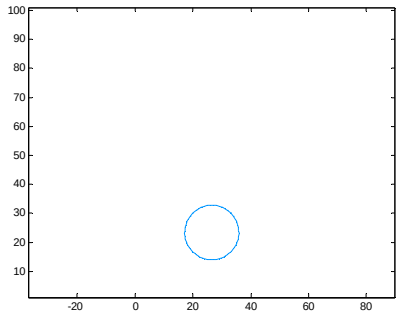

time 0 sec

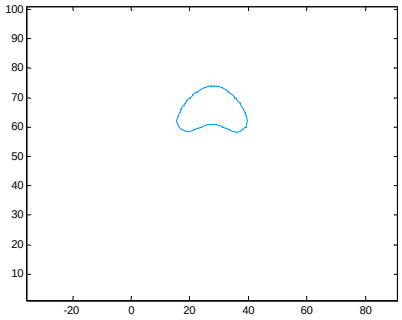

time 0.5 sec

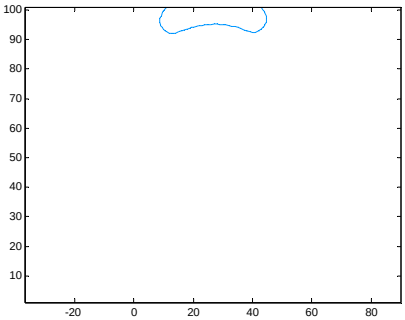

time 1 sec

Figure 2.4: Bubble rising simulation using level set method with mass conservation technique (Fukano and Inatomi, 2003)

This reconstruction is done by changing the level set value at each node near these marker points to correctly restore the interface. The "particle level set" method compares favorably with VOF and front tracking in mass conservation and interface resolution, respectively.

2.1.3 Front Tracking Method

In the front tracking method, the front is discretized into many marker points whose position is used to construct the interface as shown in Figure 2.5. Numerous articles describing this method have been published (see, for example, Glimm et al., 1998 and Tryggvason et al., 2001). In this method, a stationary Eulerian grid is used to describe the fluid flow, while the interface is tracked by a Lagrangian grid of lower dimension. At each time step, the Navier-Stokes equation is solved on the Eulerian grid; the velocity information is then transferred to the Lagrangian grid to advect the interface. The resulting interface information provided by the Lagrangian grid is, in turn, passed to the Eulerian grid so that the Navier-Stokes equation could be solved for the next time step.

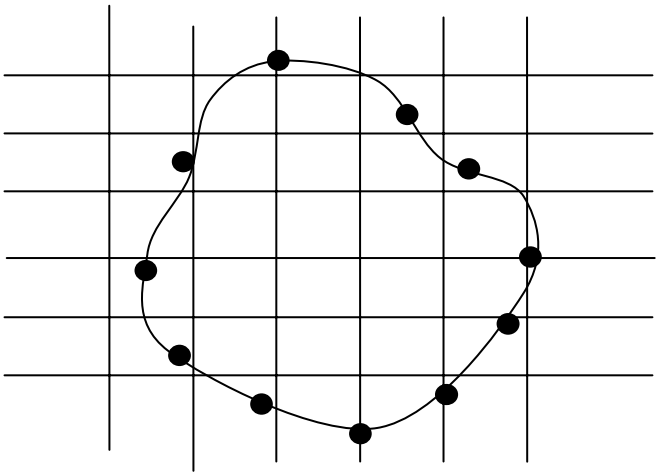

Figure 2.5: Schematic representation of the front tracking method

Front tracking has many advantages; among them is the lack of numerical diffusion, ease, and accuracy with which interfacial physics can be described on a subgrid level. It is found that tracking often does not require as highly refined grids and that grid orientation does not affect the numerical solution, i.e. there is no grid anisotropy (Glimm *et al.*, 1998). Tracking affords a precise description of the location and geometry of the interface and thereby the surface tension force (and other interface sources) can be very accurately computed directly on the interface.

Front tracking also has shortcomings; the most often cited shortcoming is its algorithmic complexity in tracking surfaces in 3D flows and its difficulty in robustly handling interface merging and breakup particularly in 3D. These difficulties arise from the need to logically connect the interface elements and "bookkeep" changes in connectivity during interface modifications, namely, element addition, deletion or reconnection. In two-dimensions these issues are relatively minor and the implementation of a robust connectivity algorithm is fairly straightforward. However, in moving to three-dimensions, the algorithmic complexity of connectivity increases dramatically, particularly for interface reconnection during topology change. To give an example of element addition, in Figure 2.6, the interface is tracked by marker points 1, 2 and 3. After some time steps, the interface deforms considerably which necessitates the addition of another marker point (point 4) between 2 and 3, so that the interface can be simulated properly. Between point 2 and 4, the interface is represented by the dashed line. To add or delete maker points, each point must "know" its neighboring points by pointers, which presents a great computational burden in three dimensional computations.

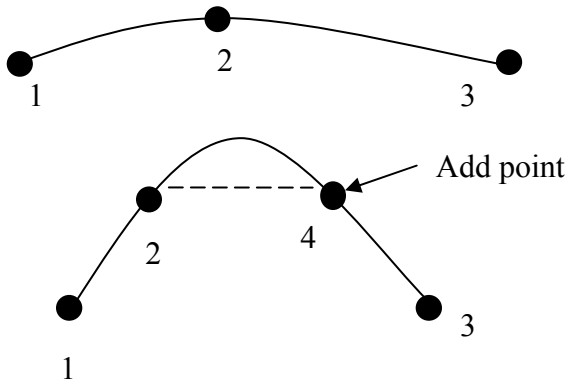

Figure 2.6: Schematic representation for the addition of a point in the front tracking method. Point 4 is added between point 2 and point 3.

Torres and Brackbill (2000) have implemented a front tracking method that eliminates the need of connectivity. They use what they call the point set method to construct a Heaviside function on the fixed grid from a set of unconnected interface points. Their Heaviside function is calculated in several steps. First, by setting an approximate indicator function equal to one in cells which contain unconnected interface points, they solve a Laplace Equation for this approximate indication function to allow them to distinguish crudely between interior and exterior cells. A second smoothed and continuous indicator function is then calculated by interpolating using tensor product of one-dimensional B-splines. Finally, they calculate a correction to this smoothed function so that contours of the indicator function coincide with the interface. Normals and curvatures required at the interface points are calculated similarly as in the level set method by using gradients of this indicator function. To obtain the surface area required for calculation of the surface tension force they construct a circular element around each interface point. The B-spline weighted area of this circle is divided by the number of

interfacial point whose distance to the center is less than a circle of a certain specified radius. Periodic interface reconstruction in their method is accomplished by using an auxiliary refined mesh and probing from this mesh to the interface contour of the indicator function. In this point regeneration algorithm, care must be taken to regenerate points from the inside or outside depending on whether the interface is undergoing coalescence or breakup. They test the accuracy of their calculations on various geometries and demonstrate the coalescence of 2D and 3D droplets in zero gravity. In essence, Torres and Brackbill (2000) are the first to "unchain" the front tracking method from its dependence on logical interface points. However, in contrast to the Level Contour Reconstruction Method that we will describe here, the approach in theirs appears to be more cumbersome when dealing with quantities such as construction of the indicator function, surface area, normals and cuavature. Interface point regeneration seems to require a relatively complex and non-general algorithm as well. The authors also admit that their method is more computationally costly than standard front tracking.

2.1.4 Level Contour Reconstruction Method

Invented by Shin and Juric (2002), the Level Contour Reconstruction Method is a simplified front tracking method. As discussed in the previous section, one drawback of the front tracking method is that each marker point must keep track of its neighbor marker points by pointers. The Level Contour Reconstruction Method (LCRM) (Shin and Juric, 2002, Shin and Abdel-Khalik, 2007) is a simplified front tracking method that eliminates the logical connectivity between discrete interface elements which represented a huge algorithmic burden in the original front tracking method, where neighbor element connectivity was maintained to facilitate calculation of the interface geometry (interface

normal and curvature), and for bookkeeping during element addition/deletion and topology change procedures. This becomes extremely complex particularly in three-dimensional simulations where interface merging and/or break up is frequent and important. The associated algorithmic burden has been obviated in the LCRM while the accuracy and advantages of explicit Lagrangian surface tracking are retained. The customary stationary volumetric mesh is supplemented by a moving interface mesh which is used to explicitly track the interface. This interface mesh is composed of non-stationary, Lagrangian computational points connected to form a two-dimensional surface (one-dimensional line for 2D problems). With this technique, the infinitely thin interface is approximated by a smooth distribution function that is used to distribute sources at the interface over several grid points near the interface. In this way, the front is given a finite thickness on the order of the mesh size to provide stability and smoothness. There is also no numerical diffusion since this thickness remains constant for all time.

A primary advantage of the Level Contour Reconstruction method is the ability to naturally and automatically handle interface merging and breakup in 3D flows. The interface elements are periodically discarded and then reconstructed on a level contour of the characteristic indicator function, $I(\mathbf{x},t)$. The newly reconstructed interface elements automatically take on the topological characteristics of the indicator function, thus the operations of element deletion, addition and reconnection are accomplished simultaneously and automatically in one step and without the need for element connectivity. Furthermore, once the elements are constructed, interface normals and element areas are easily defined and surface tension forces are accurately computed directly on the interface for each element independently.

A more detailed and complete description of LCRM can be found in Shin and Juric, 2002 and Shin and Abdel-Khalik, 2007. The method has been updated by using a local indicator function value for reconstruction instead of a constant contour value in order to mitigate the mass redistribution problem. The surface tension force has been modified using a hybrid surface tension force formulation which decreases the parasitic currents to a significantly smaller level (Shin et al., 2005). More detailed descriptions of these modification can be found in (Shin et al., 2005).

The above mentioned methods have been widely implemented and have found success in computing a variety of two-phase flows involving drops, bubbles and particles. Nowadays 2D computations are commonplace and 3D nearly so. Until very recently these methods have not been applied to the more general problem of flows with phase change such as boiling flows which are indeed inherently three-dimensional, very dynamic and exhibit repeated merging and breakup of liquid-vapor interfaces. Phase change flows are among the most difficult challenges for direct numerical simulation and only recently have numerical methods begun to offer the promise of helping to provide accurate prediction of the detailed small scale physical processes involved. Recent 2D computations of boiling flows include those of Juric and Tryggvason (1998) using an extension of front tracking, Welch and Wilson (2000) with VOF method and Son and Dhir (1998) using level sets. Qian, Tryggvason and Law (1998) have developed a 2D method of tracking the motion of premixed flames closely based on ideas in Juric and Tryggvson (1998) for boiling flows. Helenbrook et al. (1999) preformed similar computations of premixed flames using level set method for 2D incompressible, invisid flow that allows sharp discontinuities in fluid properties.

A number of hybrid methods have appeared in recent years. Sussman and Puckett (2000) proposed a coupled Level Set/Volume-of-fluid (VOF-CLS) method in order to alleviate some of the geometrical problems of the VOF method. It combines the accuracy in mass conservation of VOF and convenient description of topologically complex interfaces of the Level Set function. The resulting scheme still remains Eulerican, not incorporating any of the Front Tracking characteristic and still not accurate in under-resolved regions by blindly applying the VOF local mass constraint.

Aulisa et al. (2003) present a new hybrid method which combines marker and Volume-of-Fluid algorithms. Two distinct markers of grid intersection and mass conservation have been used to describe the interface. Both markers are advected numerically to update the volume fraction. The conservation markers inside each cell keep the local volume fraction to the reference value while the intersection markers, which locate the interface on the grid lines, eliminate the necessity of remeshing the system. Thus they obtain both smooth motion of the interface by marker methods and good mass conservation as in the standard VOF method.

Our specific focus here is an extension of the phase change/front tracking method of Juric and Tryggvason (1998), Shin and Abdel-Khalik (2007), and Shin and Juric (2002) to enable full 3D simulations of turbulent multiphase problems including phase change.

2.2 Prediction of Dryout

Prediction of dryout in boiling channels is a challenging problem of wide practical interest, particularly for boiling water reactors. Along a boiling channel, different flow patterns can exist before dryout is reached: single-phase liquid flow, bubbly flow, slug

flow and annular flow (Figure 2.7). Generally speaking, there are three methods for predicting dryout for BWR fuel assemblies (Mitsutake et al. 1990): (1) liquid film dryout model, (2) subchannel analysis, and (3) experimental correlations. In the experimental correlation approach, the cross section averaged variables of a fuel assembly are used in the correlation based on experimental data. In the subchannel analysis approach, a fuel assembly is divided into subchannels (Figure 2.8). For each subchannel, the governing conservation equations are solved in conjunction with experimental correlations for mass, momentum, and energy exchange between the phases to predict dryout based on subchannel averaged variable. In the liquid film dryout model, assuming annular flow, mass conservation equation is used to calculate the film mass flux at each elevation by estimating the evaporation rate, entrainment rate and deposition rate (Figure 2.9) through the use of experimental correlations.

Okawa et al. (2003) and Hewitt and Govan (1990) proposed liquid film dryout models by solving the mass conservation equation. The mass conservation equation in the annular flow region is

$$\frac{dm_f}{dz} = C\left(m_d - m_v - m_e\right) . \qquad (2.2)$$

Where m_f is the liquid film flow rate, m_v the evaporation rate, m_e the entrainment rate, m_d the deposition rate, and C a constant. The value of m_f at each elevation can be determined by calculating m_v , m_e , and m_d from experimental correlations. Dryout happens when the liquid film flow rate becomes very small. Clearly

accuracy and validity of the experimental correlations for m_v , m_e , and m_d play an important role in this liquid film dryout model.

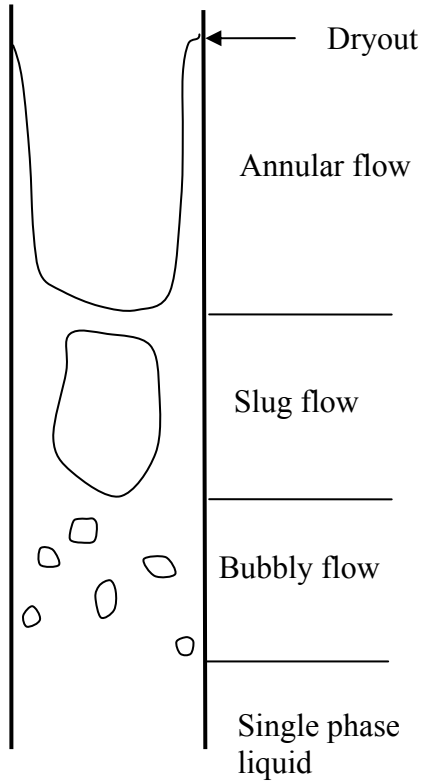

Figure 2.7: Schematic flow regime along a channel

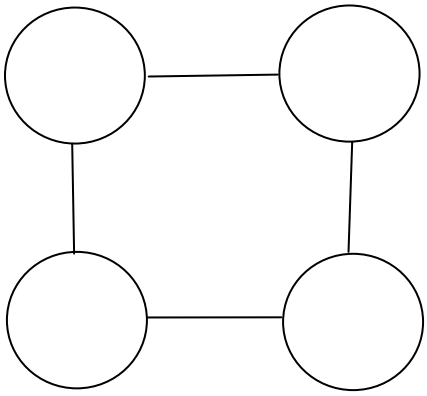

Figure 2.8: Schematic representation of a subchannel in a fuel assembly

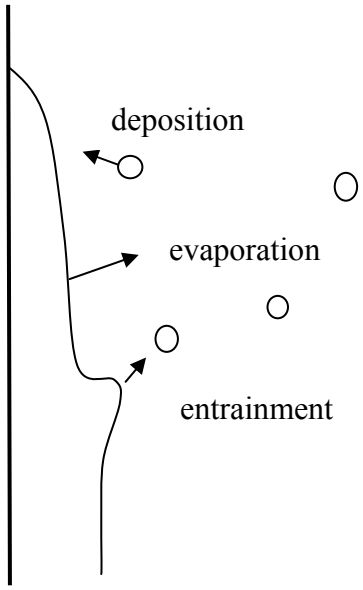

Figure 2.9: Schematic representation of deposition, evaporation and entrainment

Sugawara et al. (1990) developed a subchannel analysis code, FIDAS to estimate dryout in boiling channels. The procedure includes several steps. They first divided the assembly into many subchannels. Separate sets of the governing equations of continuity, momentum, and energy for the liquid film, vapor and entrained droplets were solved for each subchannel. By employing some experimental correlations, the FIDAS code can simulate flow regime evolution in the subchannels: single-phase liquid flow, bubbly/slug flow, annular flow, drop flow and single-phase vapor flow. Between subchannels, the exchange of mass, momentum and energy are evaluated by Prandtl's mixing length model. Other equations are used to calculate the wall shear stress, drop size, vapor-liquid interfacial drag forces, convective heat transfer, radiation heat transfer, vapor-liquid interfacial heat transfer, and vapor-droplet interfacial heat transfer. FIDAS can be used to predict dryout for round tubes and rod bundles.

Naitoh et al. (2002) developed a subchannel analysis code, CAPE-BWR, for dryout predition for fuel bundles. This code performs subchannel, liquid film flow, and spacer effect analysis. Spacers cause the flow change direction and enhance the turbulence. These effects are taken into account in their code. Turbulence is calculated by $k-\varepsilon$ model. Knabe et al. (1995) developed a subchannel analysis code, RINGS, with the similar capability as CAPE-BWR.

2.3 RANS Turbulence Models

In this section, we review some Reynolds Averaged Navier-Stokes (RANS) turbulence models for incompressible flow. This is an engineering approach for turbulence modeling. While the RANS model is not as accurate, it is much simpler than either DNS or LES models. Readers are referred to Wilcox (2006) and Ferziger and Peric (2002) for more information.

Turbulent flow is unsteady. By ensemble averaging, the velocity is decomposed as the average part and the fluctuating part.

$$u_i(x,t) = U_i(x,t) + u'_i(x,t). \tag{2.3}$$

$$U_i(x,t) = \lim_{N\to\infty} \sum_{n=1}^{N} U_i^n(x,t). \tag{2.4}$$

Averaging the governing equation leads to the Reynolds-Averaged Navier-Stokes (RANS) equation

$$\frac{\partial U_i}{\partial x_i} = 0 . \tag{2.5}$$

$$\rho \frac{\partial U_i}{\partial t} + \rho \frac{\partial}{\partial x_j}(U_j U_i) = -\frac{\partial P}{\partial x_i} + \frac{\partial}{\partial x_j}(2\mu S_{ji} - \rho \overline{u'_i u'_j}) . \tag{2.6}$$

Where $-\rho \overline{u'_i u'_j}$ is the Reynolds-stress tensor, $\tau_{ij} = \overline{u'_i u'_j}$ the specific Reynolds stress tensor. Following Boussinesq's approximation, assuming that the Reynolds-stress can be expressed by

$$\tau_{ij} = \nu_T (\frac{\partial u_i}{\partial x_j} + \frac{\partial u_j}{\partial x_i}) \ . \tag{2.7}$$

The turbulence effect is represented by the eddy viscosity ν_T . Prandtl proposed the mixing length hypothesis since eddy viscosity is related to the length scale from dimentional analysis. In two dimensions, his model can be expressed by

$$\tau_{xy} = \nu_T \frac{dU}{dy} . \tag{2.8}$$

Prandtl's mixing length hypothesis

$$\nu_T = l_{mix}^2 \left| \frac{dU}{dy} \right| . \tag{2.9}$$

Here, l_{mix} is the mixing length which is very similar to the mean free path of the molecular momentum transport. Prandtl proposed that the mixing length is proportional to the distance from the wall.

To calculate the mixing length more accurately, several algebraic (zero-equation) models have been proposed including Van Driest (1956), Cebeci-Smith (1967), and Baldwin-Lomax(1978). In the Van Driest model, the mixing length is given by:

$$l_{mix} = \kappa y\left(1 - e^{-y^+ / A^+_o}\right). \tag{2.10}$$

Cebeci-Smith Model and Baldwin-Lomax Model are classified as two-layer models. In the inner layer and outer layer, different expressions are used for the eddy viscosity.

The zero-equation models mentioned above do not perform well in separated flows thus limiting their applicability. Prandtl proposed to calculate the turbulence kinetic energy k to determine the eddy viscosity since k is related to the velocity scale. This leads to Prandtl's One-Equation Model.

$$k = \frac{1}{2}\left(\overline{u'^2} + \overline{v'^2} + \overline{w'^2}\right). \tag{2.11}$$

$$\frac{\partial k}{\partial t} + U_j \frac{\partial k}{\partial x_j} = \tau_{ij} \frac{\partial U_i}{\partial x_j} - C_D \frac{k^{3/2}}{l} + \frac{\partial}{\partial x_j}\left[\left(\nu + \nu_T / \sigma_k\right)\frac{\partial k}{\partial x_j}\right]. \tag{2.12}$$

$$\nu_T = k^{1/2} l. \tag{2.13}$$

Other one-equation models can be found in Spalart and Allmaras (1992) and Menter (1994).

To describe eddy viscosity, one might need two scales, a velocity scale and a length scale. The time scale can be derived from the velocity scale and length scale. From

Prandtl's one-equation model, we already have one equation to calculate the turbulence kinetic energy which is related to the velocity scale; we need to find another equation to describe the length scale. The most widely known two-equation models are $k-\varepsilon$ and $k-\omega$ model, where ε, ω are calculated to describe the length scale. They are related to the length scale by the following relationships:

$$\varepsilon \sim k^{3/2}/l \text{, and } \omega \sim k^{1/2}/l \,. \tag{2.14}$$

The Standard $k-\varepsilon$ Model is

$$\nu_T = C_\mu k^2/\varepsilon \,.$$

$$\frac{\partial k}{\partial t} + U_j \frac{\partial k}{\partial x_j} = \frac{1}{\rho}\tau_{ij}\frac{\partial U_i}{\partial x_j} - \varepsilon + \frac{\partial}{\partial x_j}\left[\left(\nu + \nu_T/\sigma_k\right)\frac{\partial k}{\partial x_j}\right]. \tag{2.15}$$

$$\frac{\partial \varepsilon}{\partial t} + U_j \frac{\partial \varepsilon}{\partial x_j} = C_{\varepsilon 1}\frac{1}{\rho}\frac{\varepsilon}{k}\tau_{ij}\frac{\partial U_i}{\partial x_j} - C_{\varepsilon 2}\frac{\varepsilon^2}{k} + \frac{\partial}{\partial x_j}\left[\left(\nu + \nu_T/\sigma_\varepsilon\right)\frac{\partial \varepsilon}{\partial x_j}\right]. \tag{2.16}$$

$$C_{\varepsilon 1} = 1.44, C_{\varepsilon 2} = 1.92, C_\mu = 0.09, \sigma_k = 1.0, \sigma_\varepsilon = 1.3 \,.$$

The most popular $k-\omega$ model is proposed by Wilcox (1988).

$$\frac{\partial \rho k}{\partial t} + \frac{\partial \rho u_j k}{\partial x_j} = P_k - \beta^* \rho \omega k + \frac{\partial}{\partial x_j}\left[\left(\mu + \sigma_{k1}\mu_t\right)\frac{\partial k}{\partial x_j}\right]. \tag{2.17}$$

$$\frac{\partial \rho \omega}{\partial t} + \frac{\partial \rho u_j \omega}{\partial x_j} = \gamma_1 P_\omega - \beta_1 \rho \omega^2 + \frac{\partial}{\partial x_j}\left[\left(\mu + \sigma_{\omega 1}\mu_t\right)\frac{\partial \omega}{\partial x_j}\right]. \tag{2.18}$$

$$P_k = \mu_t \frac{\partial u_i}{\partial x_j}(\frac{\partial u_i}{\partial x_j} + \frac{\partial u_j}{\partial x_i}) - \frac{2}{3}\rho k \delta_{ij} \frac{\partial u_i}{\partial x_j}. \tag{2.19}$$

$$P_\omega = \rho \frac{\partial u_i}{\partial x_j}(\frac{\partial u_i}{\partial x_j} + \frac{\partial u_j}{\partial x_i}) - \frac{2}{3}\rho \omega \delta_{ij} \frac{\partial u_i}{\partial x_j}. \tag{2.20}$$

$$\begin{aligned} &\sigma_{k1} = 0.5, \sigma_{\omega 1} = 0.5, \beta_1 = 0.075 \\ &\beta^* = 0.09, \kappa = 0.41, \gamma_1 = \beta_1 / \beta^* - \sigma_{\omega 1}\kappa^2 / \sqrt{\beta^*} \end{aligned} \tag{2.21}$$

In 2006, Wilcox modified the $k-\omega$ model which includes "cross diffusion" and "stress limiter" terms. This improves the simulation accuracy in some complex separated flows.

Both the $k-\varepsilon$ and $k-\omega$ models has some shortcomings. The $k-\varepsilon$ model does not perform well in flows with an adverse pressure gradient and within the near wall region, while the $k-\omega$ model does not perform well in the outer region. In view of this, Menter (1992) proposed a model to combine the $k-\varepsilon$ and $k-\omega$ models. The basic idea is to use the $k-\omega$ model near the wall and change to the $k-\varepsilon$ model in the outer region, thus combining the strength of these two models. A blending function F_1 varying from zero to one is defined to achieve this goal. This model is very popular in aerospace engineering.

$$\frac{\partial \rho k}{\partial t} + \frac{\partial \rho u_j k}{\partial x_j} = P_k - \beta^* \rho \omega k + \frac{\partial}{\partial x_j}\left[(\mu + \sigma_{k1}\mu_t)\frac{\partial k}{\partial x_j}\right]. \tag{2.22}$$

$$\frac{\partial \rho \omega}{\partial t} + \frac{\partial \rho u_j \omega}{\partial x_j} = \gamma P_\omega - \beta \rho \omega^2 + 2\rho(1-F_1)\sigma_{\omega 2}\frac{1}{\omega}\frac{\partial k}{\partial x_j}\frac{\partial \omega}{\partial x_j} + \frac{\partial}{\partial x_j}\left[(\mu + \sigma_\omega \mu_t)\frac{\partial \omega}{\partial x_j}\right]. \tag{2.23}$$

CHAPTER 3

ALGORITHM DEVELOPMENT

3.1 Introduction

In this chapter, the solver algorithm for using the Level Contour Reconstruction Method (LCRM) to simulate an evaporating thin liquid film on a BWR fuel rod is presented. The main contributions presented here involve expansion of the method to include turbulence effects and use of cylindrical coordinates for the fixed Eulerian grid. These modifications are necessary for proper modeling of the problem of interest, namely prediction of dryout on a BWR fuel rod with axial and azimuthal heat flux gradients and cross flow from neighboring subchannels. In a BWR reactor core, the Reynolds number of the flow is nearly 10^6; hence, the flow is highly turbulent. To model the physics of the flow and dryout on a fuel rod, it is important to account for the turbulent effects. Indeed, turbulence has a large impact on the critical heat flux calculation as will be seen in the next chapter. Without accounting for turbulence, the calculated dryout heat flux will likely be considerably higher than the actual value, i.e. non-conservative. The governing equation for turbulent flow to be used in this investigation is the RANS equation rather than the original Navier-Stokes equation. Standard $k-\varepsilon$ model will be used to close the RANS equation.

In addition to simulating the turbulent effects, we solve the governing equations and construct the interface using a cylindrical coordinate system rather than the Cartesian

coordinate system used in the original LCRM development (Shin and Juric, 2002). Using a Cartesian coordinate system to simulate a cylindrical BWR fuel rod requires use of an immersed boundary method to approximate the boundary condition on the rod surface. While numerical schemes such as the immersed boundary method have gained some success in the past, the use of cylindrical coordinates for the problem at hand makes it considerably easier to specify the boundary conditions without any approximation. This is particularly important to our simulation since the liquid film on the rod is expected to be very thin and its movement is very sensitive to the boundary condition on the surface. Using a cylindrical coordinate system eliminates any unnecessary approximations.

The main steps in the model are:

1. solve the RANS equations for velocity and pressure
2. solve the k, ε equations for k, ε, and eddy viscosity
3. solve the energy conservation equation for temperature
4. advect the marker points on the interface using LCRM
5. go to step 1 for the next time step
6. reconstruct the interface every 10 time steps using LCRM

In the following sections, we will present our governing equations, numerical methods and LCRM in more detail. Sections 3.2, 3.3 and 3.4 are devoted to the governing equations, grid structure, and numerical methods, respectively. Section 3.5 describes the Level Contour Reconstruction Method, while Section 3.6 presents higher order Level Contour Reconstruction Method. Section 3.7 introduces the method used to compute the surface tension force, while Sections 3.8 to 3.10 deals with the sharp interface temperature method, boundary conditions, and wall functions.

3.2 Governing Equations

The liquid-vapor phase change problem involves both fluid flow and heat transfer and requires the solution of the governing equations coupled with appropriate interface boundary conditions. Isothermal flow without phase change is a special case of the formulation presented here. We write one set of transport equations valid for both phases. This local, single field formulation incorporates the effect of the interface in the equations as delta function source terms, which act only at the interface. The Navier-Stokes equation in vector form is:

$$\frac{\partial \mathbf{u}}{\partial t} + \mathbf{u} \cdot \nabla \mathbf{u} = -\frac{1}{\rho}\nabla p + \mathbf{g} + \frac{1}{\rho}\nabla \cdot \mu(\nabla \mathbf{u} + \nabla \mathbf{u}^T) + \mathbf{F}. \tag{3.1}$$

Here in the left hand side are the unsteady and advection terms, while the right hand side includes the pressure term, gravity term, viscous term, and surface tension force term **F**.

The Reynolds Averaged Navier-Stokes (RANS) equation for turbulent flow is very similar to the original Navier-Stokes Eq. (3.1) except for the viscosity term. The turbulent eddy viscosity μ_T is added to the viscosity term. Turbulent eddy viscosity is a property of the flow and will be calculated from the Standard $k-\varepsilon$ model. We can write the RANS equation in cylindrical coordinate system for velocity *u, v* and *w* as:

$$\frac{\partial u}{\partial t} + u\frac{\partial u}{\partial r} + \frac{v}{r}\frac{\partial u}{\partial \theta} - \frac{v^2}{r} + w\frac{\partial u}{\partial z} = \frac{1}{\rho}\left[\frac{1}{r}\frac{\partial}{\partial r}(r\tau_{rr}) + \frac{1}{r}\frac{\partial}{\partial \theta}\tau_{\theta r} + \frac{\partial}{\partial z}\tau_{zr} - \frac{\tau_{\theta\theta}}{r}\right] - \frac{1}{\rho}\frac{\partial P}{\partial r} + g_r + F_r \tag{3.2}$$

$$\frac{\partial v}{\partial t}+u\frac{\partial v}{\partial r}+\frac{v}{r}\frac{\partial v}{\partial \theta}+\frac{uv}{r}+w\frac{\partial w}{\partial z}=\frac{1}{\rho}\left[\frac{1}{r^2}\frac{\partial}{\partial r}(r^2\tau_{r\theta})+\frac{1}{r}\frac{\partial}{\partial \theta}\tau_{\theta\theta}+\frac{\partial}{\partial z}\tau_{z\theta}+\frac{\tau_{\theta r}-\tau_{r\theta}}{r}\right]. \quad (3.3)$$
$$-\frac{1}{r\rho}\frac{\partial P}{\partial \theta}+g_\theta+F_\theta$$

$$\frac{\partial w}{\partial t}+u\frac{\partial w}{\partial r}+\frac{v}{r}\frac{\partial w}{\partial \theta}+w\frac{\partial w}{\partial z}=\frac{1}{\rho}\left[\frac{1}{r}\frac{\partial}{\partial r}(r\tau_{rz})+\frac{1}{r}\frac{\partial}{\partial \theta}\tau_{\theta z}+\frac{\partial}{\partial z}\tau_{zz}\right]. \quad (3.4)$$
$$-\frac{1}{\rho}\frac{\partial P}{\partial z}+g_z+F_z$$

The following equations define the shear stress terms in the RANS equations (3.2), (3.3), and (3.4), which include both the turbulent eddy viscosity μ_T and molecular viscosity μ_L of the fluid.

$$\begin{aligned}
\tau_{rr} &= (\mu_L+\mu_T)\left[2\frac{\partial u}{\partial r}\right] \\
\tau_{\theta\theta} &= (\mu_L+\mu_T)\left[2\left(\frac{1}{r}\frac{\partial v}{\partial \theta}+\frac{u}{r}\right)\right] \\
\tau_{zz} &= (\mu_L+\mu_T)\left[2\frac{\partial w}{\partial z}\right] \\
\tau_{r\theta} &= \tau_{\theta r} = (\mu_L+\mu_T)\left[r\frac{\partial}{\partial r}(\frac{v}{r})+\frac{1}{r}\frac{\partial u}{\partial \theta}\right] \\
\tau_{\theta z} &= \tau_{z\theta} = (\mu_L+\mu_T)\left[\frac{\partial v}{\partial z}+\frac{1}{r}\frac{\partial w}{\partial \theta}\right] \\
\tau_{zr} &= \tau_{rz} = (\mu_L+\mu_T)\left[\frac{\partial w}{\partial r}+\frac{\partial u}{\partial z}\right]
\end{aligned} \quad . \quad (3.5)$$

The turbulent eddy viscosity μ_T can be calculated from the Standard $k-\varepsilon$ equation.

To account for surface evaporation at the interface, the following equation is used,

$$\boldsymbol{M} = \nabla \cdot \mathbf{u} = \int_{A} (\frac{1}{\rho_L} - \frac{1}{\rho_G}) \dot{\boldsymbol{m}}_f \delta(\mathbf{x} - \mathbf{x}_f) \boldsymbol{dA} \,. \tag{3.6}$$

The energy equation is given by:

$$\frac{\partial T}{\partial t} + u\frac{\partial T}{\partial r} + \frac{v}{r}\frac{\partial T}{\partial \theta} + w\frac{\partial T}{\partial z} = (\alpha + \alpha_T)\nabla^2 T \begin{pmatrix} \alpha = \alpha_L & in & liquid & phase \\ \alpha = \alpha_G & in & vapor & phase \end{pmatrix} . \tag{3.7}$$

where $\nabla^2 T = \frac{1}{r}\frac{\partial}{\partial r}\left(r\frac{\partial T}{\partial r}\right) + \frac{1}{r^2}\frac{\partial^2 T}{\partial \theta^2} + \frac{\partial^2 T}{\partial z^2}$.

The Standard $k-\varepsilon$ equation is described by the following equations (Wilcox, 2006):

$$\nu_T = C_\mu k^2 / \varepsilon \,. \tag{3.8}$$

$$\frac{\partial k}{\partial t} + U_j \frac{\partial k}{\partial x_j} = \tau_{ij}\frac{\partial U_i}{\partial x_j} - \varepsilon + \frac{\partial}{\partial x_j}\left[(\nu_L + \nu_T / \sigma_k)\frac{\partial k}{\partial x_j}\right] . \tag{3.9}$$

$$\frac{\partial \varepsilon}{\partial t} + U_j \frac{\partial \varepsilon}{\partial x_j} = \tau_{ij}\frac{\partial U_i}{\partial x_j} C_{\varepsilon 1}\frac{\varepsilon}{k} - C_{\varepsilon 2}\frac{\varepsilon^2}{k} + \frac{\partial}{\partial x_j}\left[(\nu_L + \nu_T / \sigma_\varepsilon)\frac{\partial \varepsilon}{\partial x_j}\right] . \tag{3.10}$$

$C_{\varepsilon 1} = 1.44, C_{\varepsilon 2} = 1.92, C_\mu = 0.09, \sigma_k = 1.0, \sigma_\varepsilon = 1.3$.

The first term on the right-hand side of Eq. (3.9) is the production of turbulence kinetic energy term, while the second term is the dissipation rate, at which rate the turbulent kinetic energy is converted to thermal energy by viscosity. The third term is the

diffusion term.

For cylindrical coordinates, Eqs. (3.9) and (3.10) are given by:

$$\begin{aligned}
&\frac{\partial k}{\partial t}+u\frac{\partial k}{\partial r}+\frac{v}{r}\frac{\partial k}{\partial \theta}+w\frac{\partial k}{\partial z}=\left(2\nu_T\frac{\partial u}{\partial r}-\frac{2}{3}k\right)\frac{\partial u}{\partial r}\\
&+\nu_T\left[r\frac{\partial}{\partial r}\left(\frac{v}{r}\right)+\frac{1}{r}\frac{\partial u}{\partial \theta}\right]\left(\frac{1}{r}\frac{\partial u}{\partial \theta}-\frac{v}{r}\right)+\nu_T\left(\frac{\partial w}{\partial r}+\frac{\partial u}{\partial z}\right)\left(\frac{\partial u}{\partial z}\right)\\
&+\nu_T\left[r\frac{\partial}{\partial r}\left(\frac{v}{r}\right)+\frac{1}{r}\frac{\partial u}{\partial \theta}\right]\left(\frac{\partial v}{\partial r}\right)+\left[2\nu_T\left(\frac{1}{r}\frac{\partial v}{\partial \theta}+\frac{u}{r}\right)-\frac{2}{3}k\right]\left(\frac{1}{r}\frac{\partial v}{\partial \theta}+\frac{u}{r}\right)\\
&+\nu_T\left[\frac{\partial v}{\partial z}+\frac{1}{r}\frac{\partial w}{\partial \theta}\right]\left(\frac{\partial v}{\partial z}\right)+\nu_T\left[\frac{\partial w}{\partial r}+\frac{\partial u}{\partial z}\right]\left(\frac{\partial w}{\partial r}\right)+\nu_T\left[\frac{\partial v}{\partial z}+\frac{1}{r}\frac{\partial w}{\partial \theta}\right]\left(\frac{1}{r}\frac{\partial w}{\partial \theta}\right)\\
&+\left(2\nu_T\frac{\partial w}{\partial z}-\frac{2}{3}k\right)\left(\frac{\partial w}{\partial z}\right)-\varepsilon+\frac{1}{r}\frac{\partial}{\partial r}\left[r\left(\nu_L+\nu_T/\sigma_k\right)\frac{\partial k}{\partial r}\right]\\
&+\frac{1}{r}\frac{\partial}{\partial \theta}\left[\frac{1}{r}\left(\nu_L+\nu_T/\sigma_k\right)\frac{\partial k}{\partial \theta}\right]+\frac{\partial}{\partial z}\left[\left(\nu_L+\nu_T/\sigma_k\right)\frac{\partial k}{\partial z}\right]
\end{aligned} \tag{3.11}$$

$$\begin{aligned}
&\frac{\partial \varepsilon}{\partial t}+u\frac{\partial \varepsilon}{\partial r}+\frac{v}{r}\frac{\partial \varepsilon}{\partial \theta}+w\frac{\partial \varepsilon}{\partial z}=\left(2\nu_T\frac{\partial u}{\partial r}-\frac{2}{3}k\right)\frac{\partial u}{\partial r}C_{\varepsilon 1}\frac{\varepsilon}{k}\\
&+\nu_T\left[r\frac{\partial}{\partial r}\left(\frac{v}{r}\right)+\frac{1}{r}\frac{\partial u}{\partial \theta}\right]\left(\frac{1}{r}\frac{\partial u}{\partial \theta}-\frac{v}{r}\right)C_{\varepsilon 1}\frac{\varepsilon}{k}\\
&+\nu_T\left(\frac{\partial w}{\partial r}+\frac{\partial u}{\partial z}\right)\left(\frac{\partial u}{\partial z}\right)C_{\varepsilon 1}\frac{\varepsilon}{k}+\nu_T\left[r\frac{\partial}{\partial r}\left(\frac{v}{r}\right)+\frac{1}{r}\frac{\partial u}{\partial \theta}\right]\left(\frac{\partial v}{\partial r}\right)C_{\varepsilon 1}\frac{\varepsilon}{k}\\
&+\nu_T\left[2\left(\frac{1}{r}\frac{\partial v}{\partial \theta}+\frac{u}{r}\right)-\frac{2}{3}k\right]\left(\frac{1}{r}\frac{\partial v}{\partial \theta}+\frac{u}{r}\right)C_{\varepsilon 1}\frac{\varepsilon}{k}\\
&+\nu_T\left[\frac{\partial v}{\partial z}+\frac{1}{r}\frac{\partial w}{\partial \theta}\right]\left(\frac{\partial v}{\partial z}\right)C_{\varepsilon 1}\frac{\varepsilon}{k}+\nu_T\left[\frac{\partial w}{\partial r}+\frac{\partial u}{\partial z}\right]\left(\frac{\partial w}{\partial r}\right)C_{\varepsilon 1}\frac{\varepsilon}{k}
\end{aligned} \tag{3.12}$$

$$
\begin{aligned}
&+\nu_T\left[\frac{\partial v}{\partial z}+\frac{1}{r}\frac{\partial w}{\partial \theta}\right]\left(\frac{1}{r}\frac{\partial w}{\partial \theta}\right)C_{\varepsilon 1}\frac{\varepsilon}{k}\\
&+\nu_T\left(2\frac{\partial w}{\partial z}-\frac{2}{3}k\right)\left(\frac{\partial w}{\partial z}\right)C_{\varepsilon 1}\frac{\varepsilon}{k}-\frac{\varepsilon^2}{k}C_{\varepsilon 2}\\
&+\frac{1}{r}\frac{\partial}{\partial r}\left[r\left(\nu_L+\nu_T/\sigma_k\right)\frac{\partial \varepsilon}{\partial r}\right]+\frac{1}{r}\frac{\partial}{\partial \theta}\left[\frac{1}{r}\left(\nu_L+\nu_T/\sigma_k\right)\frac{\partial \varepsilon}{\partial \theta}\right]\\
&+\frac{\partial}{\partial z}\left[\left(\nu_L+\nu_T/\sigma_k\right)\frac{\partial \varepsilon}{\partial z}\right]
\end{aligned}
\qquad (3.12)
$$

These governing equations are discretized and solved using a cylindrical coordinate system; detailed steps are presented in sections 3.3 and 3.4. Boundary conditions are introduced in section 3.9. Near the wall, wall functions are used for turbulence kinetic energy, dissipation rate and temperature. The wall functions will be presented in section 3.10.

3.3 Grid Structure and Finite Difference Discretization

In our study, a staggered grid in a cylindrical coordinate system which stores velocity at the edge and scalar quantities at the center of the cell is used (see Fig. 3.1). The advantages of using a staggered grid include treating derivatives more naturally and enhancing the stability of the numerical scheme, while the main disadvantage is complexity.

For the problem of interest, the length scale in the axial (z) direction is considerably larger than the rod diameter and film thickness. Nevertheless, the grid should not be overly stretched in the axial direction. In our simulations, the value of Δz

is limited to less than four times Δr, if Δz is larger than about four Δr, the numerical solution diverges.

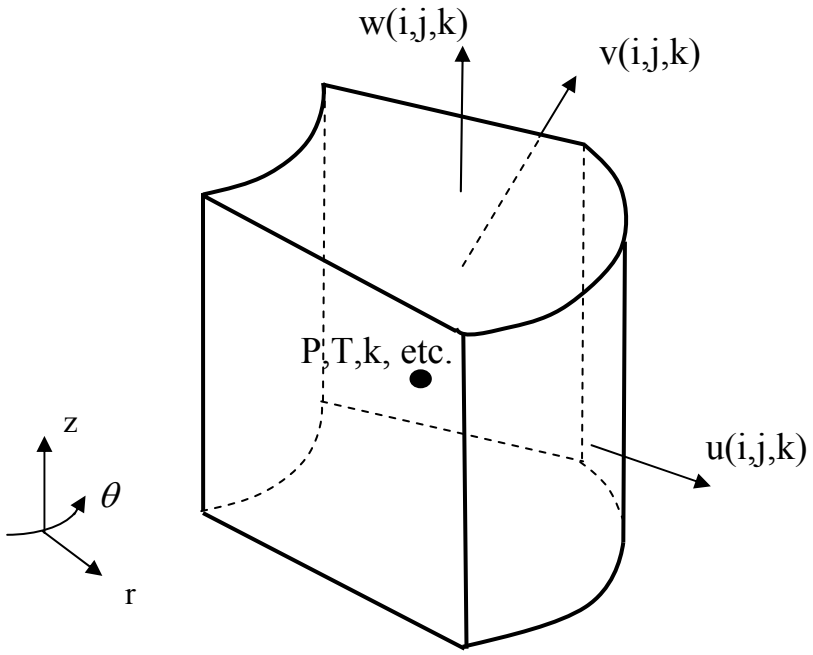

Figure 3.1: Staggered grid for cell (i,j,k) in cylindrical coordinate system

The common central difference scheme to discretize the governing equations is employed. This central difference scheme is introduced by the following examples on the r-θ plane.

Example 3.1: Finite difference discretization $\left.\frac{1}{r}\frac{\partial}{\partial r}(r\cdot\tau_{rr})\right|_A = \left.\frac{1}{r}\frac{\partial}{\partial r}(r\cdot\mu\cdot 2\frac{\partial u}{\partial r})\right|_A$

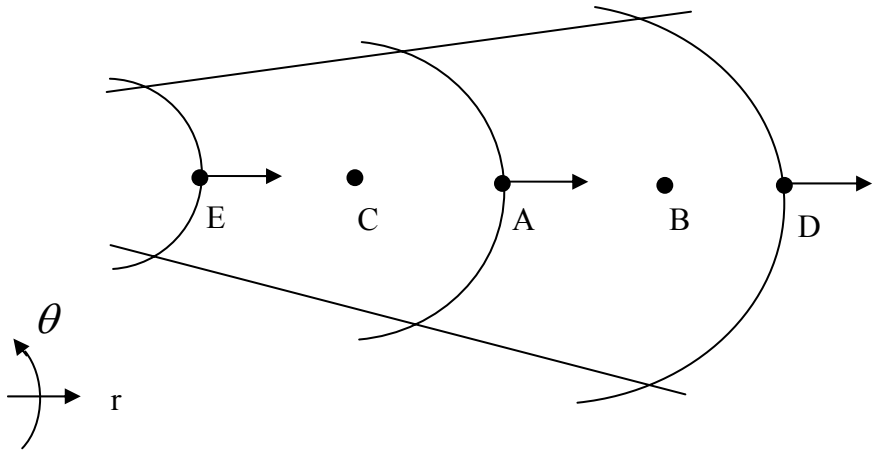

Figure 3.2: Finite difference scheme of Example 3.1

$$\left.\frac{1}{r}\frac{\partial}{\partial r}(r\cdot\mu\cdot 2\frac{\partial u}{\partial r})\right|_A \approx$$

$$\frac{1}{r(A)}\frac{1}{\Delta r}\left\{r(B)\cdot\mu(B)\cdot 2\cdot\frac{u(D)-u(A)}{\Delta r}\right.$$

$$\left.-\,r(C)\cdot\mu(C)\cdot 2\frac{u(A)-uE)}{\Delta r}\right\} \qquad (3.13)$$

Example 3.2

Finite difference discretization

$$\frac{1}{r^2}\frac{\partial}{\partial r}\left\{r^2\tau_{r\theta}\right\}\Big|_A = \frac{1}{r^2}\frac{\partial}{\partial r}\left\{r^2\mu\left[r\frac{\partial}{\partial r}\left(\frac{v}{r}\right)+\frac{1}{r}\frac{\partial u}{\partial \theta}\right]\right\}\Big|_A$$

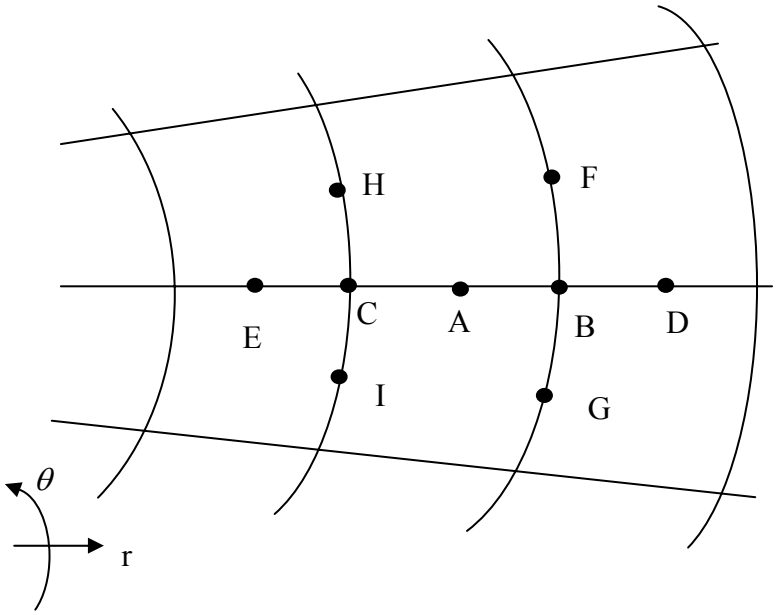

Figure 3.3: Finite difference scheme of Example 3.2

$$\frac{1}{r^2}\frac{\partial}{\partial r}\left\{r^2\mu\left[r\frac{\partial}{\partial r}\left(\frac{v}{r}\right)+\frac{1}{r}\frac{\partial u}{\partial \theta}\right]\right\}\Big|_A$$

$$\approx \frac{1}{r(A)^2}\frac{1}{\Delta r}\left\{r^2\mu\left[r\frac{\partial}{\partial r}\left(\frac{v}{r}\right)+\frac{1}{r}\frac{\partial u}{\partial \theta}\right]\Big|_B - r^2\mu\left[r\frac{\partial}{\partial r}\left(\frac{v}{r}\right)+\frac{1}{r}\frac{\partial u}{\partial \theta}\right]\Big|_C\right\}$$

$$\approx \frac{1}{r(A)^2}\frac{1}{\Delta r}\left\{\begin{array}{l} r^2(B)\mu(B)\left[r(B)\dfrac{1}{\Delta r}\left(\dfrac{v(D)}{r(D)}-\dfrac{v(A)}{r(A)}\right)+\dfrac{1}{r(B)}\dfrac{1}{\Delta\theta}\left(u(F)-u(G)\right)\right] \\ -r^2(C)\mu(C)\left[r(C)\dfrac{1}{\Delta r}\left(\dfrac{v(A)}{r(A)}-\dfrac{v(E)}{r(E)}\right)+\dfrac{1}{r(C)}\dfrac{1}{\Delta\theta}\left(u(H)-u(I)\right)\right] \end{array}\right\} \quad (3.14)$$

3.4 Projection method

The RANS equation is solved using Chorin's projection method (Chorin, 1968). The discrete form of Equation 3.2, 3.3 and 3.4 can be written as

$$\frac{\mathbf{u}^{n+1}-\mathbf{u}^{n}}{\Delta t}+\mathbf{A}\mathbf{u}^{n}=\frac{1}{\rho}\mathbf{A}^{n}+\mathbf{F}^{n}-\frac{1}{\rho}\nabla_{h}P. \tag{3.15}$$

Where, for ease of discussion, the viscous and gravitational terms are lumped into $\mathbf{A}^{n}$. $\mathbf{A}\mathbf{u}^{n}$ is the advection term. The subscript *h* implies a spatially discrete operator, while $\mathbf{F}^{n}$ is the surface tension force term.

We split the RANS equation into three equations.

$$\frac{\tilde{\mathbf{u}}-\mathbf{u}^{n}}{\Delta t}+\mathbf{A}\mathbf{u}^{n}=0. \tag{3.16}$$

$$\frac{\breve{\mathbf{u}}-\tilde{\mathbf{u}}}{\Delta t}=\frac{1}{\rho}\mathbf{A}^{n}+\mathbf{F}^{n}. \tag{3.17}$$

and

$$\frac{\mathbf{u}^{n+1}-\breve{\mathbf{u}}}{\Delta t}=-\frac{1}{\rho}\nabla_{h}P. \tag{3.18}$$

where $\tilde{\mathbf{u}}$ and $\breve{\mathbf{u}}$ are the intermediate terms. Note that if we sum up the three equations 3.16, 3.17, and 3.18, $\tilde{\mathbf{u}}$ and $\breve{\mathbf{u}}$ will be canceled. Equation 3.16 is solved by the Courant-Isaacson-Rees method (CIR) (Courant et al., 1952), which simply track the characteristic

information backward (Figure 3.4). More information about CIR scheme can be found in (Dupont and Liu, 2003)

$$\tilde{\mathbf{u}} = \mathbf{u}^n\left(r - u\cdot\Delta t, \theta - \frac{v}{r}\cdot\Delta t, z - w\cdot\Delta t\right) . \tag{3.19}$$

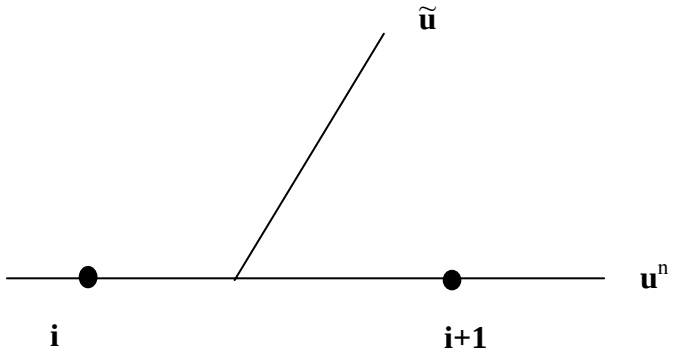

Figure 3.4: Schematic presentations for CIR method. The characteristic information is tracked backward. $\tilde{\mathbf{u}}$ is calculated by interpolation of $\mathbf{u}_i^n$ and $\mathbf{u}_{i+1}^n$

Then for equation 3.17,

$$\breve{\mathbf{u}} = \tilde{\mathbf{u}} + \frac{\Delta t}{\rho}\mathbf{A}^n + \Delta t\cdot\mathbf{F}^n . \tag{3.20}$$

The pressure is found by taking the divergence of 3.18 and enforcing the mass balance equation $\nabla\cdot\mathbf{u}^{n+1} = 0$. This leads to a Poisson equation for the pressure.

$$\nabla_h\cdot\left(\frac{1}{\rho}\nabla_h P\right) = \frac{\nabla\cdot\breve{\mathbf{u}}}{\Delta t} . \tag{3.21}$$

Equation 3.21 is solved for pressure by the biconjugate gradient stabilizer iteration (Bi-CGSTAB) method (H.A. van der Vorst, 1992).

The updated velocity field is finally found from 3.18

$$\mathbf{u}^{n+1} = \breve{\mathbf{u}} - \frac{\Delta t}{\rho} \nabla_h P \,. \tag{3.22}$$

Next step is to solve the $k-\varepsilon$ model and temperature equation following the scheme in the projection method. For the turbulent kinetic energy equation 3.11, we discretize the equation as

$$\frac{k^{n+1} - k^n}{\Delta t} + Ak^n = Rhs^n \,. \tag{3.23}$$

$$Rhs^n = \left(\tau_{ij} \frac{\partial U_i}{\partial x_j} \right)^n - \varepsilon^n + \left\{ \frac{\partial}{\partial x_j} \left[(\nu_L + \nu_T / \sigma_k) \frac{\partial k}{\partial x_j} \right] \right\}^n \,. \tag{3.24}$$

where Ak^n is the advection term, and Rhs^n is the discretize form of all the right hand side terms in equation 3.11. We split the turbulence kinetic energy equation into two equations.

$$\frac{\widetilde{k} - k^n}{\Delta t} + Ak^n = 0 \,. \tag{3.25}$$

$$\frac{k^{n+1} - \widetilde{k}}{\Delta t} = Rhs^n \,. \tag{3.26}$$

where $\widetilde{k}$ is the intermediate term. Using the CIR method, $\widetilde{k}$ is evaluated:

$$\widetilde{k} = k^n(r - u\cdot\Delta t, \theta - \frac{v}{r}\cdot\Delta t, z - w\cdot\Delta t)\,. \tag{3.27}$$

After finding $\widetilde{k}$, k^{n+1} is evaluated using the relation:

$$k^{n+1} = \widetilde{k} + Rhs^n\cdot\Delta t\,. \tag{3.28}$$

The dissipation rate equation 3.12 can also be split into two equations, which can be solved following the same steps used for turbulent kinetic energy.

$$\frac{\widetilde{\varepsilon} - \varepsilon^n}{\Delta t} + A\varepsilon^n = 0\,. \tag{3.29}$$

$$\frac{\varepsilon^{n+1} - \widetilde{\varepsilon}}{\Delta t} = Rhs^n\,. \tag{3.30}$$

$$Rhs^n = \left(\tau_{ij}\frac{\partial U_i}{\partial x_j}C_{\varepsilon 1}\frac{\varepsilon}{k}\right)^n - \left(C_{\varepsilon 2}\frac{\varepsilon^2}{k}\right)^n + \left\{\frac{\partial}{\partial x_j}\left[(\nu_L + \nu_T/\sigma_k)\frac{\partial k}{\partial x_j}\right]\right\}^n \tag{3.31}$$

Using the CIR method, $\widetilde{\varepsilon}$ is evaluated:

$$\widetilde{\varepsilon} = \varepsilon^n(r - u\cdot\Delta t, \theta - \frac{v}{r}\cdot\Delta t, z - w\cdot\Delta t) \tag{3.32}$$

After finding $\widetilde{\varepsilon}$, ε^{n+1} is determined using the relation:

$$\varepsilon^{n+1} = \widetilde{\varepsilon} + Rhs^n\cdot\Delta t \tag{3.33}$$

The k, ε equations are "stiff". Large time step and mesh may lead to non-physical values. It usually takes several attempts to identify the proper time step and mesh resolution.

The energy equation is solved separately for each phase. We split the energy equation into two equations for each phase and solve using the same procedure used for the turbulent kinetic energy and dissipation rate.

$$\frac{\widetilde{T} - T^n}{\Delta t} + AT^n = 0 . \tag{3.34}$$

$$\frac{T^{n+1} - \widetilde{T}}{\Delta t} = \left\{(\alpha + \alpha_T)\nabla^2 T\right\}^n . \tag{3.35}$$

The CIR method is a first order method. To get second order accuracy in space and time, Dupont and Liu proposed the use of Back and Forth Error Compensation and Correction method (BFECC, Dupont and Liu, 2003). Basically, BFECC uses CIR scheme for three times.

CIR$(u,v,w,\psi^n,\widetilde{\psi})$

CIR$(-u,-v,-w,\widetilde{\psi},\overline{\psi})$

$\widetilde{\psi} = \psi^n + e$

$e = (\psi^n - \overline{\psi})/2$

CIR$(u,v,w,\widetilde{\psi},\psi^{n+1})$

Where ψ can be *u, v, w, k,* ε, or T in the governing equations, and *e* is the error

compensation term.

The velocity field in turbulent flow may contain singularities; using BFECC at these locations may produce artifacts impacting the solution. To remedy this issue, at these singularities, one simply turns off BFECC. Even though this approach decreases accuracy, it is the simplest way to deal with such artifacts. For the velocity u, v, and w, the detector suggested by (Kim and Carlson, 2007) is used, while the detector suggested by (Dupond and Liu, 2003) is used for k, ε, and T, The detailed steps are,

---

Condition 1 $\left|u_{i+1,j,k} - 2u_{i,j,k} + u_{i-1,j,k}\right| \le \min(\left|u_{i+1,j,k} - u_{i,j,k}\right|, \left|u_{i,j,k} - u_{i-1,j,k}\right|)$

Condition 2 $\left|v_{i,j+1,k} - 2v_{i,j,k} + v_{i,j-1,k}\right| \le \min(\left|v_{i,j+1,k} - v_{i,j,k}\right|, \left|v_{i,j,k} - v_{i,j-1,k}\right|)$

Condition 3 $\left|w_{i,j,k+1} - 2w_{i,j,k} + w_{i,j,k-1}\right| \le \min(\left|w_{i,j,k+1} - w_{i,j,k}\right|, \left|w_{i,j,k} - w_{i,j,k-1}\right|)$

For velocity u,

If Condition 1 is satisfied, use BFECC; otherwise set *e* to zero.

For velocity v

If Condition 2 is satisfied, use BFECC; otherwise set *e* to zero.

For velocity w,

If Condition 3 is satisfied, use BFECC; otherwise set *e* to zero.

For k, ε, and T,

If (Condition1), (Condition 2), and (Condition 3) are satisfied simultaneously, use BFECC; otherwise set *e* to zero.

3.5 Level Contour Reconstruction Method

The Level Contour Reconstruction Method was briefly introduced in Chapter 2. It represents a hybrid between the front tracking method and the level set method to eliminate the need for logical connectivity. Additional details are given below

3.5.1 Indicator Function

The material properties for the two phases are considered to be constant, but not generally equally for each phase. As a consequence, the bulk fluids are incompressible. Equations for the material property fields can be written for the entire domain using a Heaviside function which we will call the indicator function, $I(\mathbf{x},t)$. Here $I(\mathbf{x},t)$ takes the value 1 in one phase and 0 in the other phase. The values of the material property fields at every location can then be given by

$$b(\mathbf{x},t) = b_1 + (b_2 - b_1)I(\mathbf{x},t), \tag{3.36}$$

where the subscripts 1 and 2 refer to the respective phases and "*b*"stands for density, ρ, viscosity, μ, specific heat, c, or thermal conductivity, tk .

$I(\mathbf{x},t)$ is found by solving the Poisson equation

$$\nabla^2 I = \nabla \cdot \int_{\Gamma(t)} \mathbf{n}\delta(\mathbf{x} - \mathbf{x}_f)ds, \tag{3.37}$$

where $\mathbf{n}$ is the unit normal to the interface and $\mathbf{x}_f = \mathbf{x}(s,t)$ is a parameterization of the interface $\Gamma(t)$ .The three-dimensional delta function $\delta(\mathbf{x} - \mathbf{x}_f)$ is non zero only when

$\mathbf{x} = \mathbf{x}_f$. Note that the right-hand side of this Poisson equation is a function only of the known interface position, a fact we use to advantage in our numerical implementation. Readers are referred to Juric and Tryggvason (1998) for more information about Eq. (3.37).

3.5.2 Transfer of Information between the Interface and the Fixed Grid

There are two grids in our LCRM model, namely an Eulerican grid in a cylindrical coordinate system and a Lagrangian grid (marker points) as shown in Figure 3.5. We solve all the governing equations on the Eulerian grid. The Lagrangian grid constitutes the marker points being on the interface used to track its movement. At each time step, information must be passed between the moving Lagrangian interface and the stationary Eulerian grid. Since the Lagrangian interface points, $\mathbf{x}_p$, do not necessarily coincide with the Eulerian grid points, $\mathbf{x}_{ij}$, this information transfer is done using Peskin's immersed boundary method (Peskin, 1977). With this technique, the infinitely thin interface is approximated by a smooth distribution function that is used to distribute sources at the interface over several grid points near the interface. In a similar manner, this function is used to interpolate field variables from the stationary grid to the interface. In this way, the front is given a finite thickness on the order of the mesh size to provide stability and smoothness. There is also no numerical diffusion since the thickness of the front remains constant for all time.

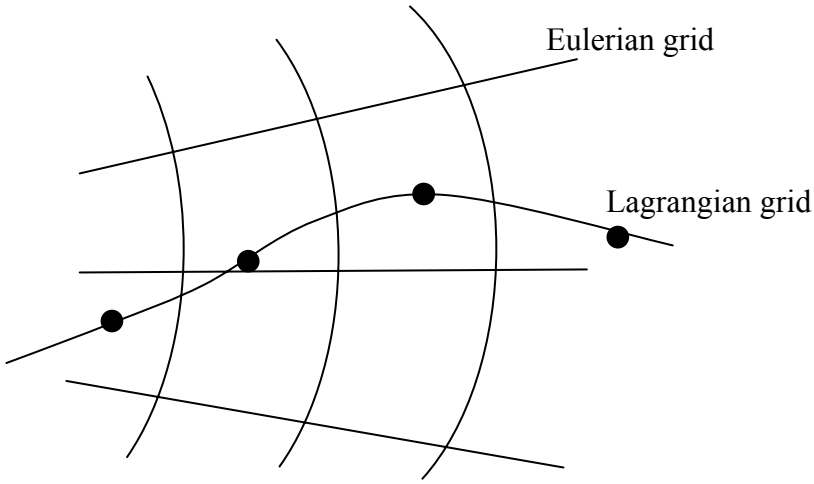

Figure 3.5: Two grids are used in our model: Eulerican grid in cylindrical coordinate system and Lagrangian grid (marker points) to track the interface.

The surface tension term integrals which appear in the governing equations can be written as

$$\Phi = \int_{\Gamma(t)} \phi \delta(\mathbf{x} - \mathbf{x}_f) ds \,. \tag{3.38}$$

The discrete interface sources, ϕ_p, can be distributed to the grid and the discrete field variables. R_{ij} can be interpolated to the interface by the discrete summations:

$$\Phi_{ij} = \sum_p \phi_p D_{ij}(\mathbf{x}_p) \Delta s \,. \tag{3.39}$$

$$R_p = \sum_{ij} h_r h_\theta R_{ij} D_{ij}(\mathbf{x}_p) \,. \tag{3.40}$$

Where Δs is the element length in the 2D case or element area in 3D. Equation (3.39) is the discretized form of (3.38). For $\mathbf{x}_p$ we use the distribution function suggested by Peskin

and McQueen (1994),

$$D_{ij}(\mathbf{x}_p) = \frac{\delta(r_p / h_r - i)\delta(\theta_p / h_\theta - j)}{h_r h_\theta}. \tag{3.41}$$

Where

$$\delta(r) = \begin{cases} \delta_1(r), & |r| \le 1 \\ 1/2 - \delta_1(2 - |r|) & 1 < |r| < 2 \\ 0 & |r| \ge 2 \end{cases}. \tag{3.42}$$

$$\delta_1(r) = \frac{3 - 2|r| + \sqrt{1 + 4|r| - 4r^2}}{8}. \tag{3.43}$$

The above expensions for D_{ij} can be easily extended to three-dimensions.

3.5.3 Interface Reconstruction by Level Contours

Here, we explain the central idea in the LCRM. Readers are referred to (Shin and Juric 2002, Shin and Abdel-Khalik 2007) for more details. We take advantage of the fact that we really have two separate representations of the interface position: (1) the explicitly tracked interface elements and (2) the indicator function whose 0.5 contour level also represents the interface. Thus, beginning with a given indicator function field we can deposit a collection of interface elements on the 0.5 contour or, conversely, beginning with the interface elements we can solve the Poisson equation 3.37 for the indicator function.

Let us suppose that at the end of a time step we have used the tracked interface elements in the solution of Eq. 3.37 to obtain the indicator function, *I*, at each grid point (Figure 3.6). We now completely discard the interface elements and construct new ones.

The procedure to do this is actually quite simple. We first draw a contour level across each grid cell at the value I=0.5 using linear interpolation. The two end points of this contour line form the endpoints of one new interface element. Because we use linear interpolation, neighboring elements from neighboring cells will always have the same endpoint locations. Since interface points that coexist at the same spatial location will move with the same velocity, the elements will never separate. Thus although adjacent elements are not logically connected, their endpoints are automatically physically linked. In this way, all adjacent interface elements are implicitly connected and the need for explicit bookkeeping of neighbor element connectivity is obviated.

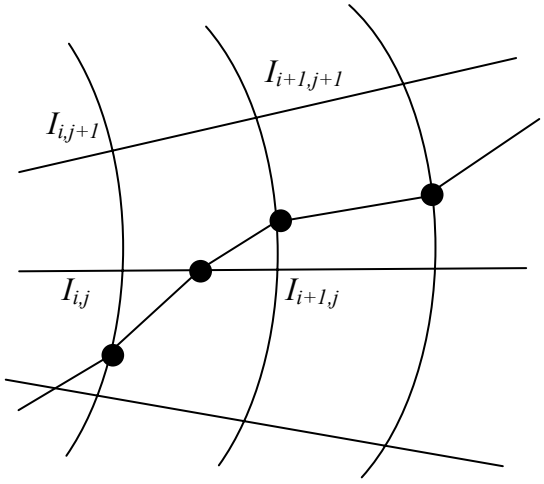

Figure 3.6: Level contour reconstruction in 2D calculation

For now the interface elements are arbitrarily oriented. A simple procedure is used to orient the elements so that all the element normals point toward the inside of the volume enclosed by the surface. As shown in Figure 3.7 , the elements are oriented cell

by cell such that maximum cell indicator function value lies to the right of the element tangent drawn from point 1 to point 2.

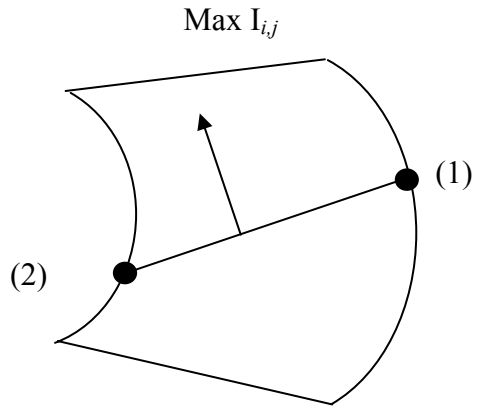

Figure 3.7: Element orientation. Elements are oriented so that maximum cell indicator function value lies to the right of the element drawn from point 1 to point 2. In this way all element normals point consistently to the inside o the enclosed volume.

We now have newly constructed and properly oriented interface elements that lie on the 0.5 indicator function contour level and whose endpoints are physically connected. The reconstruction step has replaced the need to add or delete elements individually. In this way the method handles topology change automatically and naturally in a way much like the level set method does using the distance function. During the course of a simulation, reconstruction is not performed at every time step. The frequency of reconstruction can be prescribed. In the simulations performed here we have found that reconstruction at every 10 time steps is sufficient. However, this frequency will most likely vary depending on the particular interface feature sizes and time scales of the

problem. Although we have not done so here it would be possible to dynamically adjust the reconstruction frequency during the calculation. In between reconstruction steps, the usual point tracking by Lagrangian advection is performed by a simple integration which will be introduced in section 3.5.5.

3.5.4 Interfacial Mass Flux

Evaporation and/or condensation is detemined by performing an energy balance at the interface. The interfacial mass flux is given by:

$$\dot{m}_f h_{fg} = (\mathbf{q}_2 - \mathbf{q}_1)\cdot\mathbf{n} = -k_G \left.\frac{\partial T}{\partial n}\right|_G + k_L \left.\frac{\partial T}{\partial n}\right|_L . \tag{3.44}$$

Where $\mathbf{q}_1$ and $\mathbf{q}_2$ represent the heat flux vectors on the liquid and vapor sides of the interface and $\mathbf{n}$ is the outwardly directed unit normal.

3.5.5 Advecting Surface Points

With phase change, the marker point motion is governed by the velocity and interfacial mass flux:

$$\frac{dr_f}{dt} = u_f + \frac{\dot{m}_f}{\rho_f}\mathbf{n}_r . \tag{3.45}$$

$$\frac{d\theta_f}{dt} = \frac{v_f}{r_f} + \frac{\dot{m}_f}{r_f \rho_f}\mathbf{n}_\theta . \tag{3.46}$$

$$\frac{dz_f}{dt} = w_f + \frac{\dot{m}_f}{\rho_f}\mathbf{n}_z . \tag{3.47}$$

3.5.6 Local Level Contour Reconstruction for Low Resolution Simulations

In the original LCRM described in 3.5.3, although mass is globally conserved

during the interface reconstruction procedure, local conservation is not guaranteed. Using a constant indicator function value, I_f, as the sought after reconstruction contour during reconstruction can result in a mass redistribution. Indeed, it is possible that mass can be unphysically transported from regions of high curvature to regions of low curvature. In the worst case, mass could even be transported across the domain between two completely separate interfaces. Thus when seeking the constant reconstruction contour, I_f, the higher curvature surface would sacrifice some of its volume to the lower curvature surface. Although this effect is normally small (Shin and Juric, 2002), it can be noticed when the size of fine scale interface structures are poorly resolved by the grid. Our motivation is to improve this problem even at low resolution and especially for 3D calculations where low resolutions must often be resorted to.

To mitigate this problem, we modified the method to automatically use different choices of the reconstruction contour values throughout the domain. As can be seen in Figs. 3.8 (a) and (b), we can interpolate (using a Peskin distribution, for example) the grid indicator function values to a surface element point. The idea then is to use this local indicator function value at the surface to reconstruct the element at that cell location. There may be more than one surface element in one cell. After having interpolated the indicator function values to the surface for all the elements, observe that each cell is affected by several elements $I_{p,e}$ with areas, Δs_e . Thus the optimum contour value to use for reconstruction, I_{opt} , at that location is calculated by distributing this value back onto the Eulerian grid

$$I_{opt}(i,j,k) = \frac{\sum_e I_{p,e}\Delta s_e}{\sum_e \Delta s_e}. \tag{3.48}$$

These are the local values we use to reconstruct the surface in that cell. Finally, we match the total volume before and after reconstruction. With this local procedure in the LCRM, there is virtually no mass redistribution between different surfaces even at low resolution.

To get even higher order accuracy, we use higher order level contour reconstruction method as will be presented in section 3.6.

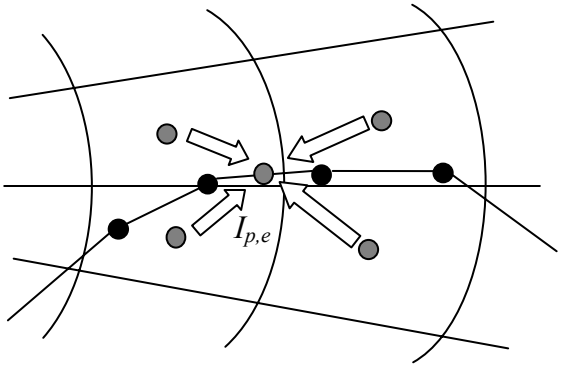

(a)

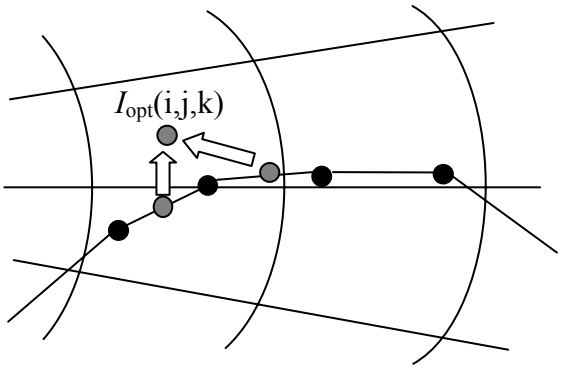

(b)

Figure 3.8: Improved level contour reconstruction method using localized I_{opt} value.

3.6 Higher Order Level Contour Reconstruction Method

In the Level Contour Reconstruction Method, the interface is composed of non-stationary, not logically but implicitly connected computational points to form a two-dimensional surface or one-dimensional line for 3D or 2D problems, respectively. The interface elements are periodically discarded and then reconstructed on a certain level contour of the characteristic indicator function. However, the level contour of the indicator function which satisfies the exact location of the original interfacial points before reconstruction is not, in general, a constant value. At a specific time step and given a complete set of tracked interface elements, we can obtain the indicator function value at each element point by interpolating the original grid indicator function values to surface element points. We then redistribute these local indicator function values back to the nearest grid locations. Thus we generate a localized contour level field, $I_{local}(i,j,k)$, which will be used to reconstruct the element at that cell location. Finally we draw a contour line/surface of zero value with linear evaluation function, $E^L(\mathbf{x})$,

$$E^L(\mathbf{x}) = \sum_g \left[I_{org}(i,j,k) - I_{local}(i,j,k) \right] P(\mathbf{x} - \mathbf{x}_g) \tag{3.49}$$

Here $I_{local}(i,j,k)$ represents the given indicator function field before reconstruction, $\mathbf{x}$ is the evaluation point, $\mathbf{x}_g$ is the grid cell center, and the summation is performed across a small multiple of the mesh spacing in each direction. $P(\mathbf{x} - \mathbf{x}_g)$ is a tensor product of one-dimensional Linear interpolation kernels, L, given by:

$$P(\mathbf{x}-\mathbf{x}_g) = L(r-r_g;\Delta r)L(\theta-\theta_g;\Delta\theta)L(z-z_g;\Delta z) \tag{3.50}$$

with grid spacing Δr, $\Delta\theta$, and Δz. The Linear interpolation kernel is defined by:

$$L(r;h) = \begin{cases} 1-\dfrac{|r|}{h}, & 0 \le \dfrac{|r|}{h} \le 1 \\ 0, & otherwise \end{cases} . \tag{3.51}$$

where h is the grid spacing in each direction. Hereafter, we will refer to this as the linear reconstruction procedure as compared to the high order reconstruction which will be discussed below.

The linear reconstruction always generates a small perturbation near the reconstructed interface since we used a linear interpolation kernel function, which is continuous but not smooth, to locate the zero level of the evaluation function, even though the surface can be reconstructed accurately with small mass redistribution between different curvature regions by using the localized indicator function value. Furthermore, the values of indicator function interpolated from the $I_{local}(i,j,k)$ field at the original interface points do not exactly match the value interpolated from the given original indicator function $I_{org}(i,j,k)$. We interpolated the indicator function value from the original interface points and then redistributed this back to the grid, so that the final local indicator function field is an "averaged" value since each cell can be affected by several elements.

This perturbation eventually dies out since the reconstruction is usually not performed every time step during the course of a simulation. Thus the global sense of the

error can usually be considered to be minimal. But for some problems which undergo abrupt change of interfacial motion from a surface tension dominant equilibrium state to a dynamic flow regime with large deformation, rupture, and coalescence, frequent reconstruction becomes necessary. The reconstruction time step usually depends on the specific problem at hand and the optimal time step can be difficult to obtain. With excessive reconstruction, the small disturbances from reconstruction can drive the interface to unphysical locations and the solution will depend on the reconstruction time step chosen. The problem becomes worse for small length scales without sufficient resolution, which turns out to be a frequent scenario of three-dimensional simulations.

To locate a contour line/surface in the indicator function field, we need two ingredients: a level contour value at a specific location and the evaluation function field to compute field level. A continuous and smooth contour level can be obtained using B-spline interpolation functions. B-spline interpolation allows smoothing of the possibly noisy data (Monaghan, 1985). The indicator function value at an arbitrary location can be found by:

$$I(\mathbf{x}) = \sum_g I_{org}(i,j,k) S(\mathbf{x} - \mathbf{x}_g). \tag{3.52}$$

Here, $S(\mathbf{x} - \mathbf{x}_g)$ is a tensor product of one-dimensional B-splines, given by:

$$S(\mathbf{x} - \mathbf{x}_g) = M(r - r_g; \Delta r) M(\theta - \theta_g; \Delta\theta) M(z - z_g; \Delta z). \tag{3.53}$$

We used both the cubic B-splines $M_3(r;h)$ and quintic B-splines $M_5(r;h)$ suggested by Torres and Brackbill (2000),

$$M_3(r;h)=\begin{cases}\dfrac{2}{3}-\left(\dfrac{|r|}{h}\right)^2+\dfrac{1}{2}\left(\dfrac{|r|}{h}\right)^3, & 0\le\dfrac{|r|}{h}\le 1\\ \dfrac{1}{6}\left(2-\dfrac{|r|}{h}\right)^3, & 1\le\dfrac{|r|}{h}\le 2\\ 0 & ,otherwise\end{cases} \tag{3.54}$$

$$M_5(r;h)=\frac{1}{120}\begin{cases}\left(3-\dfrac{|r|}{h}\right)^5-6\left(2-\dfrac{|r|}{h}\right)^5+15\left(1-\dfrac{|r|}{h}\right)^3, & ,0\le\dfrac{|r|}{h}\le 1\\ \left(3-\dfrac{|r|}{h}\right)^5-6\left(2-\dfrac{|r|}{h}\right)^5, & 1\le\dfrac{|r|}{h}\le 2\\ \left(3-\dfrac{|r|}{h}\right)^5, & 2\le\dfrac{|r|}{h}\le 3\\ 0 & otherwise\end{cases}. \tag{3.55}$$

We can obtain the evaluation function field which gives a zero contour level at interface reconstruction from:

$$E^*(\mathbf{x})=\sum_g\left[I_{org}(i,j,k)-I_{local}(i,j,k)\right]S(\mathbf{x}-\mathbf{x}_g). \tag{3.56}$$

The evaluation field $E^*(x)$ has continuous and smooth properties along the zero contour level. But if we compute the evaluation function value at the original interface point, the resulting value is still not exactly zero due to the manner of calculating $I_{local}(i,j,k)$.

To get a more precise location for the reconstructed interfacial elements, we correct by adding a trial function field Ψ_{ijk}, which will satisfy the zero contour value at

the original interface point. The corrected Eulerical evaluation field function is defined by:

$$E^H(\mathbf{x}) = \sum_g \left[I_{org}(i,j,k) - I_{local}(i,j,k) \right] S(\mathbf{x} - \mathbf{x}_g) - \sum_g \Psi_{ijk} S(\mathbf{x} - \mathbf{x}_g). \qquad (3.57)$$

There are several ways of approximating the trial function. We assumed a function described:

$$\Psi_{ijk} = \sum_{N_p} \delta I_P S(\mathbf{x}_g - \mathbf{x}_p). \qquad (3.58)$$

Here, $\mathbf{x}_p$ is the location of original interface points before reconstruction δI_p is the increment needed at the original interface points, and the integration has been performed throughout the entire given element, respectively. After rearrangement of equation (3.57) and (3.58), the final form of the system of linear equations which satisfies a zero level of evaluation function is:

$$\sum_g \sum_{N_p} \delta I_p S(\mathbf{x}_g - \mathbf{x}_p) S(\mathbf{x} - \mathbf{x}_g) = \sum_g \left[I_{org}(i,j,k) - I_{local}(i,j,k) \right] S(\mathbf{x} - \mathbf{x}_g). \qquad (3.59)$$

The idea here is similar to the Point Set Method of Torres and Brackbill (2000). However, they construct a new indicator function by adding a function interpolated directly from interface points to interface points:

$$I(\mathbf{x}) = \sum_{N_p} \delta I_P S(\mathbf{x} - \mathbf{x}_p) + I_{org}(\mathbf{x}). \qquad (3.60)$$

This was used to find the value of δI_p which would give a constant indicator function value throughout the interfacial points. This proves useful in two-dimensional simulations but requires a tremendous amount of work in three-dimensions. The computational effort needed to find the first part of the right hand side of equation 3.60 is N_p for a single grid location. For the entire computational domain, the number of computations required is $N_p \times N_r \times N_\theta \times N_z$ required. This would most likely be impractical to perform three-dimensional simulations unless additional information for interface point locations is provided

Equation 3.57 is a more convenient form which can be treated efficiently for function evaluation. We distribute the δI_p the increment throughout the domain to construct the Eulerian field trial function and then interpolate this back to the original interfacial points to force the zero contour of I_{org}(i,j,k)-I_{local}(i,j,k). Equation 3.59 can be rewritten in simple form as follows:

$$\Phi\left[\delta I_{p,m}\right] = b(x_{p,m}), m = 1,..., N_p . \tag{3.61}$$

We calculate $\delta I_{p.m}$ using a Newton iteration scheme

$$\delta I_{p,m}^{l+1} = \delta I_{p,m}^{l} - \left[\mathbf{J}\right]^{-1} \Phi(\delta I_{p,m}^{l}), m = 1,..., N_p . \tag{3.62}$$

where l is the iteration index and **J** is the Jacobian matrix of partial derivatives of the error with respect to the $\delta I_{p.m}$. Since these derivatives are difficult to calculate and

the subsequent matrix inversion would be computationally expensive, a simple form of Jacobian is used,

$$\mathbf{J} = a^{-1}\mathbf{I}. \tag{3.63}$$

where $\mathbf{I}$ is the identity matrix and a is a constant which determines the rate of convergence of the iteration. At the optimum value of a, different for different physical parameters, the iteration converges rather quickly to a tolerance of $\varepsilon = 10^{-5}$ in 10 to 100 iterations. Optimum values for a were determined through experiment and range roughly between 1 and 10. The tolerance is calculated by

$$\varepsilon = \max(\left|\delta I_{p,m}^{l+1}\right|), m = 1,..., N_p. \tag{3.64}$$

The higher order Level Contour Reconstruction Method bears great resemblance to the Point Set Method of Torres and Brackbill (2000). They used points rather than the line or triangular elements which we use in our Level Contour Reconstruction Method. Because we utilize higher dimensions in the front description, calculation of geometric quantities such as curvature, normal and tangent associated with the interface becomes much more straightforward to implement.

In general the reconstructed interface contains elements of non-uniform size because the location of reconstruction is confined to the edge of each grid cell. The irregularity of element size does not produce any problem with the high order reconstruction but increases the required memory by generating insignificant size elements without any additional accuracy enhancement. Usually elements of the size of

the spatial grid size are recommended. Thus in terms of memory optimization it is preferable to generate elements of roughly uniform size.

We regularize the interface elements in the following two steps (Figure 3.9): First we draw an approximate contour line neglecting relatively small elements. We draw a new line, which passes through the edge of the cell when the distance from the reconstructing point to the edge of each cell, *dl*, is less than a specified criterion. We call this process "attaching to the grid". Because the first step is simply a rough approximation, we can use either equation 3.49 or 3.56 to locate the reconstructed interface. The next step is to relocate this approximate contour line/point to the exact interfacial location depicted by equation 3.57 by movement in the normal direction.

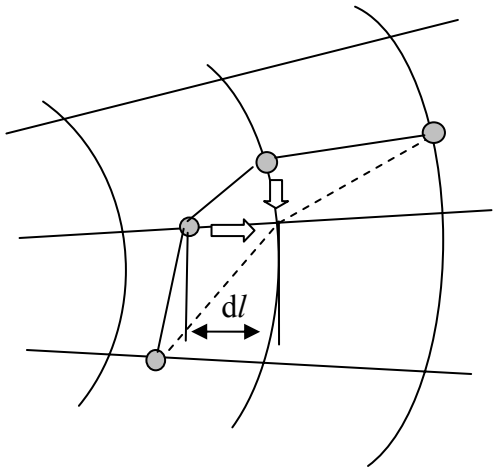

(a)

Figure 3.9: Regularizing the surface points in two steps as shown in (a) and (b)

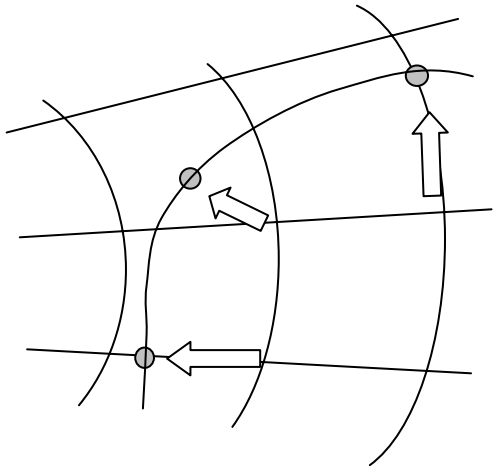

(b)

Figure 3.9: Regularizing the surface points in two steps as shown in (a) and (b)

After these two steps, the size of the reconstructed interface elements may not be exactly the same but they are quite uniform. The range of element sizes is usually 1 or 1.5 times the spatial grid size. By regularizing the interface elements, we can reduce the elements to 70% of that of the previous reconstruction procedure without sacrificing the accuracy. This is quite important in three-dimensional cases where resources are highly restricted.

3.7 Computing the Surface Tension Force

In this section, we will first briefly describe the conventional surface tension calculation method used in front tracking. Next we will give a brief description of a

purely Eulerian approach, the VOF-CSF method. Finally, we introduce a hybrid Lagrangian-Eulerian computation of the surface tension force in front tracking. We will use a hybrid Lagrangian-Eulerian method in our evaporating thin liquid film model.

3.7.1 Conventional Lagrangian Front Tracking Approach for Calculating the Surface Tension Force

In the conventional front tracking approach, the surface tension force **F** is calculated directly on the Lagrangian interface grid. This force is then distributed onto the fixed Eulerian grid using Peskin's immersed boundary method applied to the surface integral

$$\mathbf{F}_L = \int_{\Gamma(t)} \sigma \kappa_f \mathbf{n}_f \delta_f (\mathbf{x} - \mathbf{x}_f) ds, \tag{3.65}$$

where σ is the surface tension coefficient (assumed constant value here) and κ_f is twice the mean interface curvature calculated directly on the Lagrangian grid before the immersed boundary distribution to the Eulerian grid. We use the subscript L on the force in equation (3.62) to distinguish it as having been calculated first directly on the Lagrangian grid before the immersed boundary distribution to the Eulerian grid. The distcrete numerical expression of this distribution onto the fixed grid is in the form of a sum over interface elements e:

$$\mathrm{F}_{L,i,j,k} = \sum_e \mathrm{f}_e D_{i,j,k}(\mathrm{x}_e) \Delta s_e . \tag{3.66}$$

Where Δs_e is the element area and $D_{i,j,k}$ is a discrete approximation to the Dirac function. The tension force on each surface element (typically a plane triangle in 3D) is given by:

$$\mathbf{f_e} = \int_{s_e} \sigma \kappa_e \mathbf{n}_e ds_e = \oint_{l_e} \sigma \mathbf{t}_e \times \mathbf{n}_e dl_e, \tag{3.67}$$

Here $\mathbf{t}_e$ is the vector tangent to the edge, l_e, of the element and $\mathbf{n}_e$ the normal to the element . The latter integral in the equation above, derived using a variation of Stoke's theorem, is a physically appealing description of the actual force on a surface imparted by surface tension. A discrete approximation of this integral is applied to each triangular surface element. The cross product of the normal and tangent vectors, the binormal, gives the direction of "pull" on the edge of each element and the net force is obtained, after multiplying by σ , by integrating around the edges of the element, Eq. (3.67), and summing the contributions of all elements, Eq. (3.66). The advantage of this form is that it exactly preserves the conservation property that the sum of the surface tension forces around a closed surface identically equals zero. Moreover, this calculation can be performed entirely on the element, independent of its neighbors.

3.7.2 Eulerian VOF-CSF Appproach for Calculating the Surface Tension Force

An alternative to calculating the force,**F**, directly on the Lagrangian surface grid is to represent it purely in Eulerian form (as in the level set or VOF-CSF approach, for example) in terms of the indicator(or color) function, C, as

$$\mathbf{F}_E = \sigma \kappa \mathbf{n} \delta . \tag{3.68}$$

where we use the subscript E on the force to denote all the quantities in Eq. (3.68) as being computed solely on the Eulerian grid. Here

$$\mathbf{n}\delta = \nabla_h C \,. \tag{3.69}$$

And the Eulerian expression for twice the mean interface curvature is

$$\kappa = -\nabla_h \cdot \mathbf{n} \,. \tag{3.70}$$

In VOF the color function is advected by Eulerian transport:

$$\frac{\partial C}{\partial t} + \mathbf{u} \cdot \nabla_h C = 0 \,. \tag{3.71}$$

3.7.3 Hybrid Formulation for Calculating the Surface Tension Forces in Front Tracking

The approach to calculate **F** is a hybrid of the Lagrangian representation, $\mathbf{F}_{\mathrm{L}}$ Eq. (3.65) and the Eulerian representation, $\mathbf{F}_{\mathrm{E},}$ in Eq. (3.68) explained as follows. We can write $\mathbf{F}_{\mathrm{L}}$ as

$$\mathbf{F}_L = \sigma \kappa_L \mathbf{G} \,. \tag{3.72}$$

where $\mathbf{G} = \int_{\Gamma(t)} \mathbf{n}_f \delta_f (\mathbf{x} - \mathbf{x}_f) ds$, for example, at a cell face

$$\mathbf{G}_{i+1/2,j,k} = \sum_e \mathbf{n}_e D_{i+1/2,j,k}(\mathbf{x}_e) \Delta s_e \,. \tag{3.73}$$

And κ_L is the sought after expression for the curvature defined on the Eulerian grid. Taking the scalar product of both the left and right sides of Eq. (3.72) with **G**

$$\mathbf{F}_L \cdot \mathbf{G} = \sigma \kappa_L \mathbf{G} \cdot \mathbf{G} . \tag{3.74}$$

gives us an expression for the curvature on the Eulerian grid in terms of quantities calculated on the Lagrangian grid :

$$\kappa_L = \frac{\mathbf{F}_L \cdot \mathbf{G}}{\mathbf{G} \cdot \mathbf{G}} . \tag{3.75}$$

Finally, we express the surface tension force in a manner analogous to VOF-CSF form in Eq. (3.68)

$$\mathbf{F} = \sigma \kappa_L \nabla_h I . \tag{3.76}$$

where I is found from the solution to the Poisson equation. Note that the numerical computation of the curvature is not intimately tied to the indicator function or its gradients as in VOF-CSF, but rather it is more closely related to the actual physical curvature of the Lagrangian surface. We will use a hybrid Lagrangian-Eulerian method in our evaporating thin liquid film model.

For cylindrical coordinates, Eq. 3.70 is given by

$$\kappa = \nabla \cdot \left(\frac{\nabla \phi}{|\nabla \phi|} \right)$$

$$= \frac{1}{r}\frac{\partial}{\partial r}\left(r \frac{\frac{\partial \phi}{\partial r}}{\sqrt{\left(\frac{\partial \phi}{\partial r}\right)^2 + \left(\frac{1}{r}\frac{\partial \phi}{\partial \theta}\right)^2 + \left(\frac{\partial \phi}{\partial z}\right)^2}} \right) \tag{3.77}$$

$$+ \frac{1}{r}\frac{\partial}{\partial \theta}\left(\frac{\frac{\partial \phi}{\partial \theta}}{r\sqrt{\left(\frac{\partial \phi}{\partial r}\right)^2 + \left(\frac{1}{r}\frac{\partial \phi}{\partial \theta}\right)^2 + \left(\frac{\partial \phi}{\partial z}\right)^2}} \right)$$

$$+ \frac{\partial}{\partial z}\left(\frac{\frac{\partial \phi}{\partial z}}{\sqrt{\left(\frac{\partial \phi}{\partial r}\right)^2 + \left(\frac{1}{r}\frac{\partial \phi}{\partial \theta}\right)^2 + \left(\frac{\partial \phi}{\partial z}\right)^2}} \right)$$

3.8 Sharp Interface Temperature Method for the Energy Equation

In the original Level Contour Reconstruction Method, the release and absorption of the latent heat of evaporation is modeled using a discrete delta source term in the energy equation. Due to memory limitations, even with current computational resources, one is often forced to use relatively crude grid resolutions for three-dimensional problems. Using a delta function source term is likely to lead to unacceptable numerical inaccuracy in cases where the interface is too close to the wall. Furthermore, it is quite difficult to maintain the interface temperature at the saturation temperature with the normal probe technique (Udaykumar, 1992). Thus, treating the interface boundary as a sharp interface is preferable especially for the energy equation since the calculation of the correct interfacial mass flux is highly dependent on obtaining an accurate temperature field calculation in the vicinity of the interface. The sharp interface temperature method is

developed by Shin and Abdel-Khalik (2007).This idea was originally applied by Durbin, 2005, to the alloy solidification problem.

Consider the liquid phase with thermal conductivity k_L. For simplicity, assume that the conductivity is constant over the entire computation domain in each phase. Here, for clarity, the arguments are presented in one dimensional form. The explicit finite-difference equation for the temperature at node i is:

$$T_i^{n+1} = T_i^n + \frac{k_L \Delta t}{h^2}\left(T_{i-1}^n + T_{i+1}^n - 2T_i^n\right). \tag{3.78}$$

where h denotes the spatial resolution and Δt is the time step. Suppose that node i-1 is located in the vapor phase while node i lies in the liquid phase. Instead of using the actual temperature at node i-1, a "ghost" value is calculated using the known temperature and location of the interface. A schematic diagram of this process is shown in Figure 3.10. The temperature at one grid spacing away from the interface, $T(x_f + \Delta x)$, is interpolated using the nearest grid points (T_i and T_{i+1}). When the distance between the grid node and the interface becomes too small, the grid node nearest to the interface is not used in the above extrapolation in order to avoid numerical instabilities. The interpolated temperature (Point D in Figure 3.10) and the interface condition (Point C in Figure 3.10) are then used to extrapolate the temperature at the ghost node i-1.

The temperature at node i then become:

$$T_i^{n+1} = T_i^n + \frac{k_L \Delta t}{h^2}\left(T_{i+1}^n + T_{ghost}^n - 2T_i^n\right). \tag{3.79}$$

where T_{ghost} is the "ghost" node temperature (point X in Figure 3.10) at the i-1 location. The advantage of this method, as compared to the immersed-boundary front-tracking method, is that the gradients near the interface are expressed more accurately and the temperature at the interface can be forced to be exactly equal to the value we specify, usually the saturation temperature. The gradient of the temperature in each phase can then be extracted easily and accurately. This information will subsequently be used to calculate the interfacial mass flux.

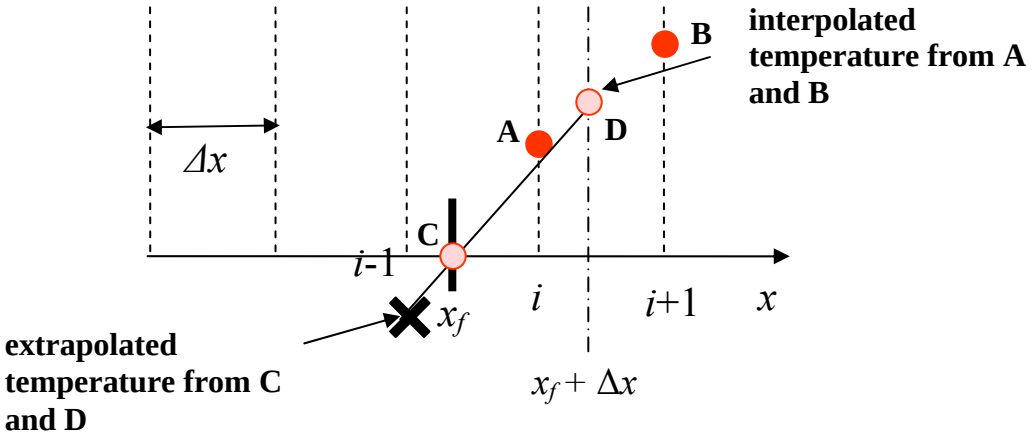

Figure 3.10: Schematic diagram for the interpolation scheme used in the sharp interface temperature method

The same procedure will apply to the computation of the vapor phase node neighboring the interface. Thus, we see that the sharp interface temperature method solves the energy equation separately in each of the two phases using the ghost fluid method for complex geometry. The only difference, as we pointed out earlier, is that the phase boundary is moving rather than stationary which imposes no additional cost in the Level Contour Reconstruction Method since the interface location is explicitly tracked. The accuracy of the sharp interface temperature method was validated by Shin and

Abdel-Khalik (2007) by comparing the results against the exact analytical solution for the Stefan problem.

3.9 Boundary Conditions

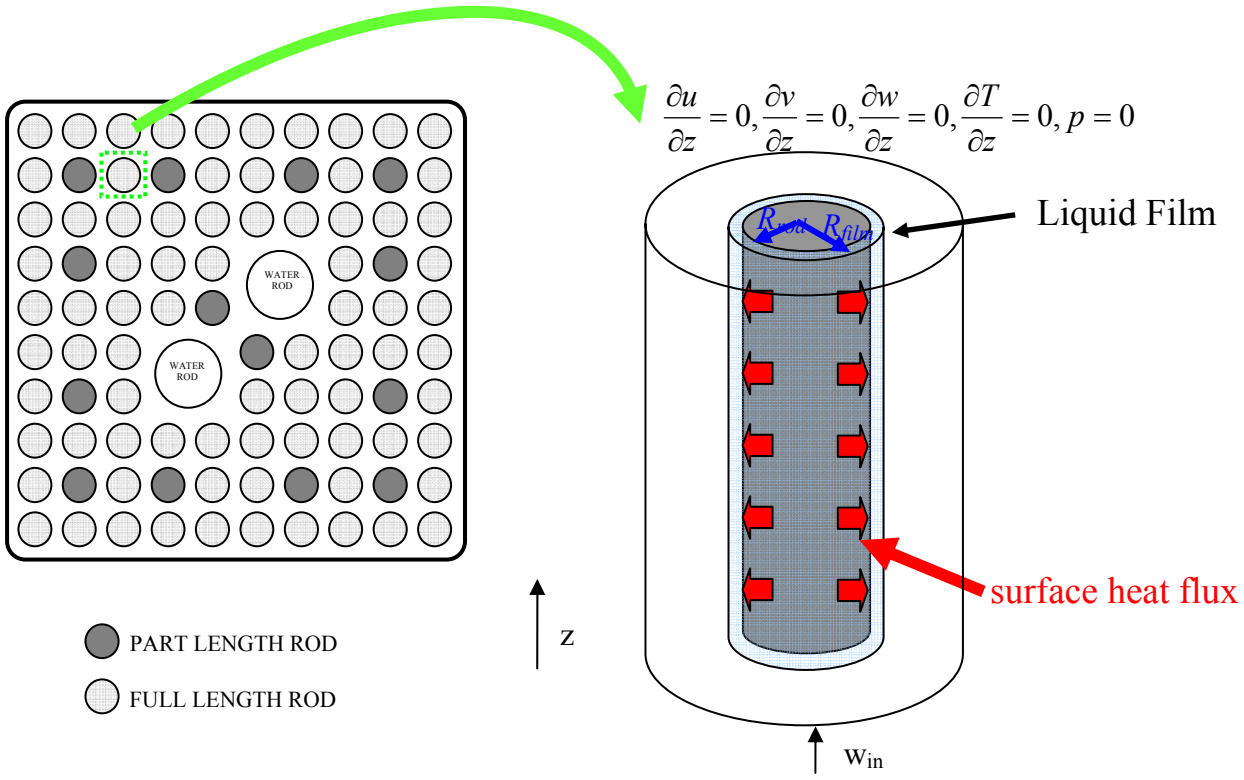

Figure 3.11: Simulation domain and boundary conditions in the simulation

Figure 3.11 shows the computation domain and boundary conditions used in this analysis. It represents an axial segment of a fuel rod within a coolant subchannel, which is about 10 cm long. Normally, a liquid film flows vertically upward along the rod with parallel vapor flow in the square subchannel. However, we simulate it as a cylindrical subchannel consistent with the cylindrical coordinate system used here.

Pressure differences between the channel of interest and neighboring subchannels within the same bundle may result in cross flow of vapor through the subchannel boundaries. Convective boundary conditions are used for both inlet and outlet. No-slip boundary conditions are applied on the inner wall. To simulate axial vapor flow, the outside cylindrical wall is assumed to be moving in the z direction with a specified velocity of w_{in}. Neumann conditions for the pressure are applied on the inner and outer wall. The liquid film is assumed to have a uniform initial thickness around the rod at the bottom of the computation domain. The value of the inlet film thickness has been fixed throughout the simulation thereby approximating a constant inlet mass flow rate of the liquid, i.e. a specified void fraction at the inlet to the computation domain.

Because of turbulence, at the first grid near the inner wall, wall functions are used to set the turbulence kinetic energy, dissipation rate, and eddy viscosity. We also need to set temperature wall function; the details are presented in section 3.10. Readers are referred to (Ferziger and Peric, 2002) for more boundary condition information on the turbulent kinetic energy and dissipation rate.

3.10 Wall Function

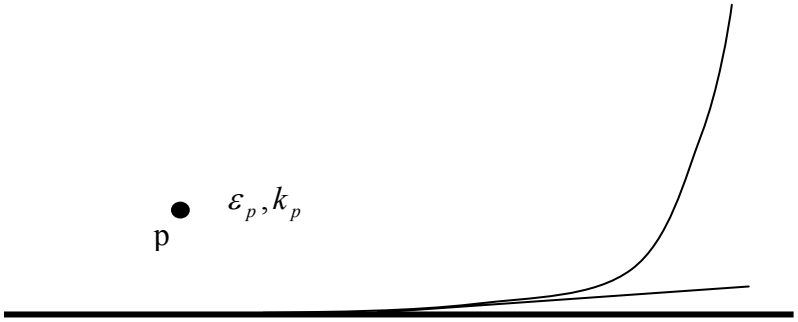

Figure 3.12: Schematic represnetation for turbulent velocity profile and wall function

The velocity gradient of tubulent flow near the wall is very high (Figure 3.12). Hence to resolve the correct velocity gradient near the wall, the first mesh point p from the wall must be very close to the wall, say $y^+ <1$. To address this issue, a nonuniform mesh is often used to place the first grid at $y^+ <1$.

$$y^+ \equiv \frac{u_\tau y}{\nu_L}. \tag{3.80}$$

However, because of the added complexity, a nonuniform mesh has not been used in this study. For a uniform mesh, we assume that the first grid point nearest to the wall is in the log layer ($30< y^+ <500$). From the law of the wall (Chapter 1) in the log layer, assuming the production of turbulence kinectic energy equals to the dissipation rate, we have the wall fuction:

$$\varepsilon_p = \frac{u_\tau^3}{\kappa y}. \tag{3.81}$$

$$k_p = \frac{u_\tau^2}{\sqrt{C_\mu}}. \tag{3.82}$$

where u_τ is found from the law of the wall by Newton's method. To derive the wall function equations 3.81 and 3.82, we start with the RANS boundary layer equation in two dimensions(Wilcox, 2006):

$$U\frac{\partial U}{\partial x} + V\frac{\partial U}{\partial y} = -\frac{1}{\rho}\frac{dP}{dx} + \frac{\partial}{\partial y}\left[(\nu_L + \nu_T)\frac{\partial U}{\partial y}\right]. \tag{3.83}$$

In the log layer, from the perturbation analysis we can neglect convection, pressure gradient and molecular viscosity because these terms are small compared to the eddy viscosity term (Wilcox, 2006) . Then Eq. 3.83 becomes,

$$0 = \frac{\partial}{\partial y}\left[\nu_T \frac{\partial U}{\partial y}\right]. \tag{3.84}$$

Eq. 3.84 implies that the Reynolds shear stress is a constant.

$$\rho\left[\nu_T \frac{\partial U}{\partial y}\right] = \tau_w = \rho u_\tau^2. \tag{3.85}$$

where τ_w is the shear stress at the wall, and u_τ is the friction velocity. Thus,

$$\left[\nu_T \frac{\partial U}{\partial y}\right] = u_\tau^2 . \tag{3.86}$$

In log layer, the law of the wall is,

$$U = \frac{u_\tau}{\kappa} \ln \frac{u_\tau y}{\nu} + C . \tag{3.87}$$

Here, κ is Karman's constant ≈ 0.41.Taking partial derivative of Eq.3.87 respect to y, we have

$$\frac{\partial U}{\partial y} = \frac{u_\tau}{\kappa y} . \tag{3.88}$$

On the other hand, in the k, ε equation, neglecting convection and molecular viscosity (Wilcox, 2006), we have

$$0 = \mathrm{Pk} - \varepsilon + \frac{\partial}{\partial y}\left[\frac{\nu_T}{\sigma_k}\frac{\partial k}{\partial y}\right]. \tag{3.89}$$

$$0 = C_{\varepsilon 1} C_\mu k \left(\frac{\partial U}{\partial y}\right)^2 - C_{\varepsilon 2}\frac{\varepsilon^2}{k} + \frac{\partial}{\partial y}\left[\frac{\nu_T}{\sigma_\varepsilon}\frac{\partial \varepsilon}{\partial y}\right]. \tag{3.90}$$

$$\nu_T = C_\mu \frac{k^2}{\varepsilon} . \tag{3.91}$$

Where Pk is the production of turbulence kinectic energy term.

$$\mathrm{Pk} = \nu_T \left(\frac{\partial U}{\partial y} \right)^2 . \tag{3.92}$$

Assuming production equals dissipation, combining Eqs. 3.86, 3.88 and 3.92, we obtain the wall function for the dissipation rate:

$$\mathrm{Pk} = \varepsilon = \nu_T \left(\frac{\partial U}{\partial y} \right)^2 = \frac{u_\tau^3}{\kappa y} . \tag{3.93}$$

From the Eqs. 3.86, 3.88, and 3.91

$$-\overline{u'v'} = \nu_T \frac{\partial u}{\partial y} = \nu_T \frac{u_\tau}{\kappa y} = C_\mu \frac{k^2}{\varepsilon} \frac{u_\tau}{\kappa y} = u_\tau^2 . \tag{3.94}$$

From Eqs. 3.93 and 3.94,

$$u_\tau^2 = C_\mu \frac{k^2}{\varepsilon} \frac{u_\tau}{\kappa y} = C_\mu \frac{k^2}{\frac{u_\tau^3}{\kappa y}} \frac{u_\tau}{\kappa y} = C_\mu \frac{k^2}{u_\tau^2} . \tag{3.95}$$

Finally we get the wall function for turbulent kinetic energy from Eq. 3.95

$$k = \frac{u_\tau^2}{\sqrt{C_\mu}} . \tag{3.96}$$

u_τ is found from the law of the wall by Newton's method. Define a function f from the law of the wall,

$$f = \frac{U}{u_\tau} - \frac{1}{\kappa}\ln\frac{u_\tau y}{\nu} - C\,. \tag{3.97}$$

where the only unkown is u_τ in the function f

$$f' = -\frac{1}{u_\tau^2} - \frac{1}{\kappa u_\tau}\,. \tag{3.98}$$

From Newton's method:

$$u_\tau^{n+1} = u_\tau^n - \frac{f}{f'}\,. \tag{3.99}$$

It usually takes no more than ten iterations to converge.

For temperature, we use the following wall function to set the temperature T_w on the heating rod surface (Chen and Jaw, 1998) .

$$T^+ = \frac{\mathrm{Pr}_t}{0.41}\ln Ey^+\,. \tag{3.100}$$

where $E = 9.0,$ and Pr_t is the tubulent Prandtl number, set equal to 0.9.

$$T^+ = \frac{T_w - T}{\dfrac{\alpha \cdot q_w}{tk \cdot u_\tau}}\,. \tag{3.101}$$

CHAPTER 4

RESULTS AND DISSCUSION

This chapter presents the simulation results obtained in this investigation. Section 4.1 presents validations of the velocity profile for single-phase flows and the curvature. Section 4.2 illustrates the detailed liquid film structure using the level contour reconstruction method for uniform heating. Section 4.3 presents the prediction of critical heat flux for internally heated annuli, while Section 4.4 includes the application to boiling water reactors.

4.1 Validation of the Velocity Profile for Single-Phase Flow and the Curvature

- Single-phase laminar flow

In order to validate our numerical methods for solving the governing equations in a cylindrical coordinate system, we have simulated the single-phase, fully- developed laminar flow in annuli, as shown in Figure 4.1. Based on the fully-developed assumption, applying the no-slip boundary condition on cylindrical walls, the Navier-Stokes equations can be solved analytically. This analytical solution can be used to measure the error of the numerical solution. The exact solution of the velocity profile in annuli is:

$$w_{exact}(r) = \frac{1}{4\mu}\frac{\partial p}{\partial z}\left[r^2 - r_o^2 + \frac{r_i^2 - r_o^2}{\ln(\frac{r_o}{r_i})}\ln(\frac{r}{r_o}) \right]. \qquad (4.1)$$

.

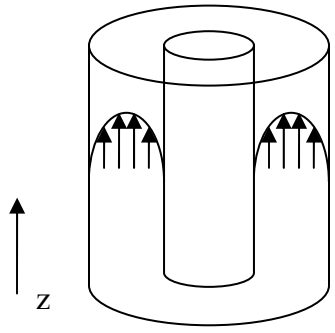

Figure 4.1: Schematic representation of the laminar flow velocity profile in an annulus

An annulus with inner radius 0.005 m, outer radius 0.008 m, and length of 0.003 m, is chosen for the simulation. The working fluid in the simulation is saturated water at 6.9 MPa (1000 psia), fluid density 741.7 kg/m^3, and viscosity 9.17x10^{-5} N-s/m^2. The inlet and outlet velocity in the z direction is set as the analytical solution. In this way, the annulus can be viewed as infinitely long. The Reynolds number is 500. The grid, $\Delta r, \Delta z$, and Δt used in the simulation are presented in Table 4.1.

Table 4.1: Input parameters in the convergence test of laminar flow in annuli

Grid	Δr , Δz (m)	Δt(sec)
$4\times4\times4$	7.5e-4	5.4e-4
$8\times8\times8$	3.75e-4	2.7e-4
$12\times12\times12$	2.5e-4	1.8e-4
$16\times16\times16$	1.875e-4	1.35e-4
$32\times32\times32$	9.375e-5	6.75e-5

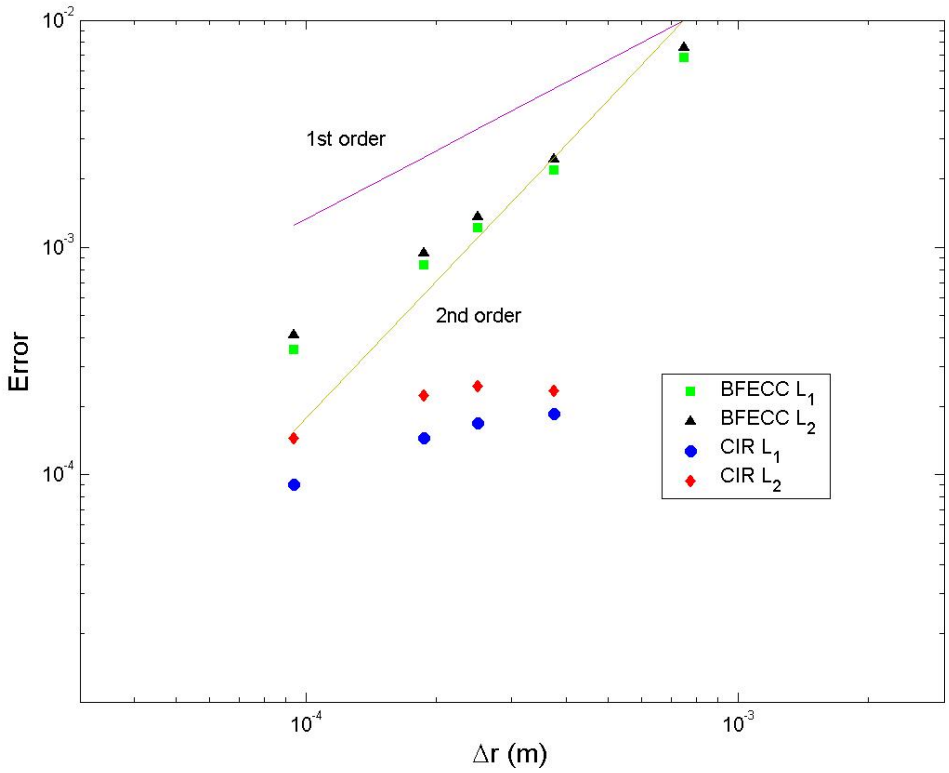

Figure 4.2: Grid convergence test results of BFECC and CIR methods for the laminar flow in annuli. This figure shows that the BFECC method is between first and second order. The CIR method is less than first order. However, the CIR method introduces smaller error than the BFECC method.

Figure 4.2 shows the convergence test results of the BFECC and CIR methods. The error norms used are defined by

$$L_1 = \frac{\sum_{i,j,k} \left| W_{cal}(i,j,k) - W_{exact}(i,j,k) \right| r(i,j,k) \Delta r \Delta\theta \Delta z}{\sum_{i,j,k} r(i,j,k) \Delta r \Delta\theta \Delta z} \,. \qquad (4.2)$$

$$L_2 = \left[\frac{\sum_{i,j,k} \left| W_{cal}(i,j,k) - W_{exact}(i,j,k) \right|^2 r(i,j,k) \Delta r \Delta\theta \Delta z}{\sum_{i,j,k} r(i,j,k) \Delta r \Delta\theta \Delta z} \right]^{1/2} . \quad (4.3)$$

where

W_{cal}=numerical solution

W_{exact}= corresponding analytical solution

i,j,k= discrete index

Figure 4.2 shows that the BFECC method is between first and second order. The CIR method is less than the first order. However, the CIR method introduces smaller errors than the BFECC method. Both of these two methods are employed in this study.

- Curvature Study

We study the accuracy of calculating the curvature from the distance function ϕ by the following equation.

$$\kappa = \nabla \cdot \left(\frac{\nabla \phi}{|\nabla \phi|} \right). \quad (4.4)$$

Eq. 4.4 is discretized directly following the general finite difference method as

$$\kappa = \nabla \cdot \frac{\nabla \phi}{|\nabla \phi|} = \frac{1}{r} \frac{\partial}{\partial r} \left(r \frac{\phi_r}{\left(\phi_r^2 + \frac{\phi_\theta^2}{r^2} \right)^{1/2}} \right) + \frac{1}{r} \frac{\partial}{\partial \theta} \left[\frac{\frac{1}{r}\phi_\theta}{\left(\phi_r^2 + \frac{\phi_\theta^2}{r^2} \right)^{1/2}} \right] \quad (4.5)$$

$$\approx \frac{1}{r_i \Delta r}\left(a_{i+1/2} - a_{i-1/2}\right) + \frac{1}{r_i \Delta \theta}\left(b_{j+1/2} - b_{j-1/2}\right).$$

where

$$a_{i+1/2} = r\frac{\phi_r}{\left(\phi_r^2 + \frac{\phi_\theta^2}{r^2}\right)^{1/2}}\Bigg|_{i+1/2} \qquad b_{j+1/2} = \frac{\frac{1}{r}\phi_\theta}{\left(\phi_r^2 + \frac{\phi_\theta^2}{r^2}\right)^{1/2}}\Bigg|_{j+1/2} \tag{4.6}$$

$$a_{i-1/2} = r\frac{\phi_r}{\left(\phi_r^2 + \frac{\phi_\theta^2}{r^2}\right)^{1/2}}\Bigg|_{i-1/2} \qquad b_{j-1/2} = \frac{\frac{1}{r}\phi_\theta}{\left(\phi_r^2 + \frac{\phi_\theta^2}{r^2}\right)^{1/2}}\Bigg|_{j-1/2}$$

To test the validity of Eqs. 4.5 and 4.6, they are used to calculate the curvature of circles. For a circle with radius r, the exact solution of curvature should be 1/r. The calculation results obtained using a low resolution mesh 4×4 are shown in Fig. 4.3. Figure 4.4 shows the L_1 error norm of the calculation. These two figures show that the numerical solution is nearly identical to the exact solution. The L_1 error norm is approximately 1×10^{-13}, which shows that the curvature calculation for circles is very accurate even when a low resolution mesh is used.

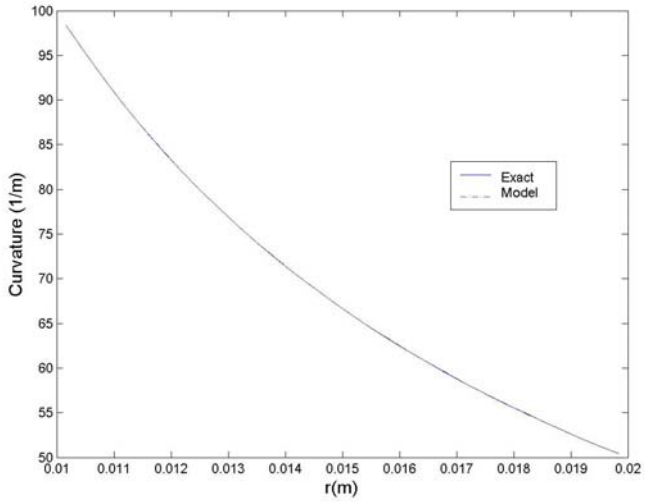

Figure 4.3: Curvature calculation results of Eqs. 4.5 and 4.6 for circles with radii between 0.01 m and 0.02 m

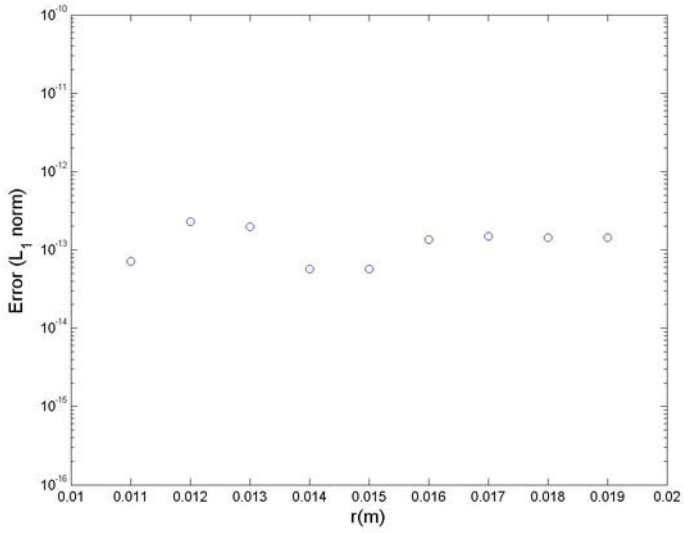

Figure 4.4: Curvature calculation errors of Eqs. 4.5 and 4.6 for circles with radii between 0.01 m and 0.02 m

- Single-phase turbulent flow

Ideally, to verify our numerical scheme for solving the turbulence model in a cylindrical coordinate system, we should compare our results with other simulations in a cylindrical coordinate system for annuli. However, we did not find such data in the public

domain. Instead, the fully-developed velocity profile for turbulent flow in a 2D channel on the x-y domain (Figure 4.5) is provided by Wilcox (2006), whose results are used to test the validity of our numerical methods.

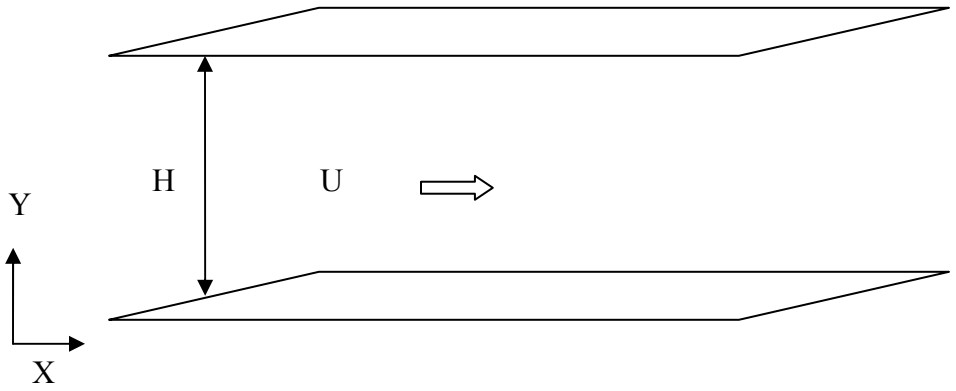

Figure 4.5: A two-dimensional channel is used to verify the numerical method in the Standard $k-\varepsilon$ turbulence model. The height of the channel is 0.1 m and the length 0.1 m.

The numerical scheme is tested in a channel with height of 0.1 m and length of 0.1 m. The fluid density is 1000 kg/m^3 and viscosity 6.38×10^{-4} N-s/m^2. The Reynolds number is 13750. Three different grids are used: 10×10, 20×20, and 50×50. The CIR method is used to solve the convection term. Since this channel is symmetric in the y direction, the Conjugate Gradient Method is used to solve the Poisson equation for pressure. In this test, we run the code until a steady state is reached with Wilcox's calculation being set as the inlet velocity profile of the channel. The wall function is applied to the first grid near the wall. The velocity profile at the mid-plane in the x direction is used to compare with Wilcox's results.

As shown in Figure 4.6, our calculation compares fairly well with Wilcox's results (2006). For the fine mesh grid, the velocity profile calculated by our numerical

model is nearly identical to that found by Wilcox (2006). With the successful completion of these validation tests, the numerical method is ready for the simulation of the evaporating thin liquid film on a cylindrical rod.

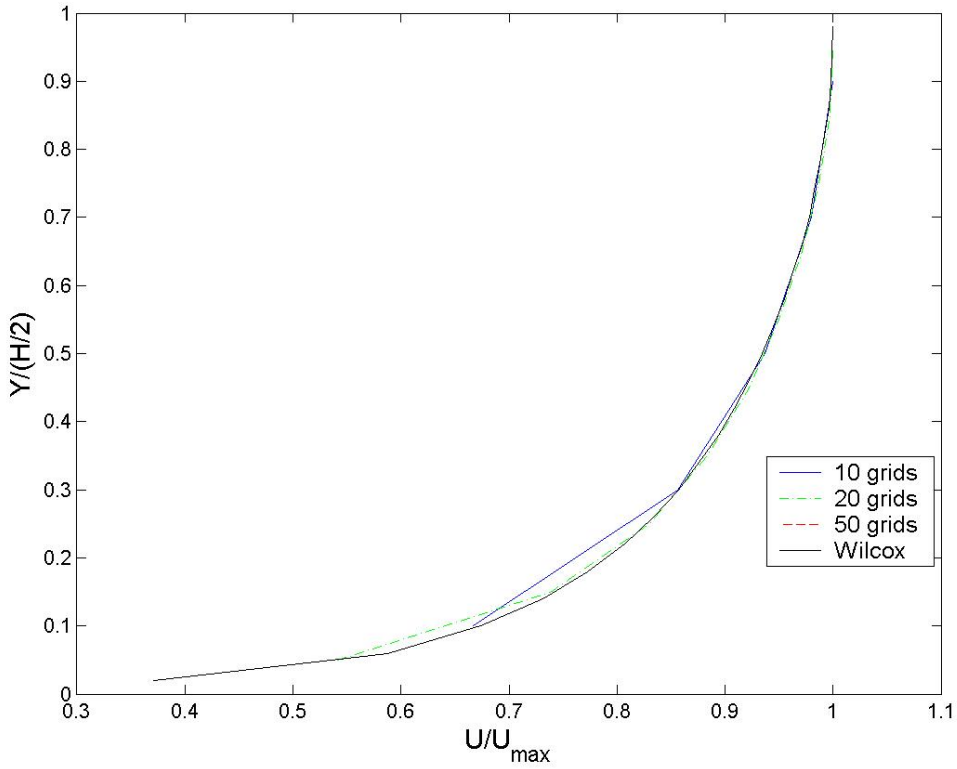

Figure 4.6: The numerical solution of the fully-developed velocity profile for turbulent flow (Re13750) in a two dimensional x-y channel

4.2 Uniformly-Heated Evaporating Thin Liquid Film on a Cylindrical Rod

In this section, the evaporating thin liquid film on a cylindrical rod with uniform heating is simulated by the level contour reconstruction method. To test the responses of the liquid film to uniform heating, both laminar and turbulent flows are simulated.

Saturated water and steam at 6.9 MPa (1000 psia) are used as the working fluids; the liquid density, viscosity, conductivity, and specific heat are 741.7 kg/m^3, 9.17×10^{-5}

kg/ms, 0.5613 W/m^{o}C, and 4973 J/kg^{o}C, respectively; the corresponding values for steam are 35.95 kg/m^{3}, 1.89×10^{-5} kg/ms, 0.0573 W/m^{o}C, and 2684 J/kg^{o}C, respectively. The latent heat of vaporization, surface tension coefficient, and saturation temperature are assumed to be constant and equal to 1.512×10^{6} J/kg, 0.01785 N/m, and 558.8 K, respectively.

In order to simulate a heated rod within a subchannel, the symmetry lines surrounding the rod within the subchannel are replaced by a moving concentric cylinder. The inner rod diameter is assumed to be 1.0×10^{-2}m and the outer "wall" diameter is assumed to be 1.693×10^{-2}m. The outer diameter has been selected to produce a channel hydraulic diameter comparable to that for typical BWR bundles. The liquid film is assumed to have a uniform initial thickness around the rod. The initial film thickness is assumed to be 1.0×10^{-3} m. At the inlet of the simulation domain, a program has been created to calculate the fully-developed velocity profile of the two-phase flow, as presented in Figure 4.7. This calculation is done by solving the governing equation of two-phase flow in the r-z domain until a steady-state is achieved with a fixed outer "wall" velocity and a no slip boundary condition at the inner wall. The velocity profile calculated in the r-z domain is then used as the inlet velocity profile of Level Contour Reconstruction Method in the r-θ-z domain.

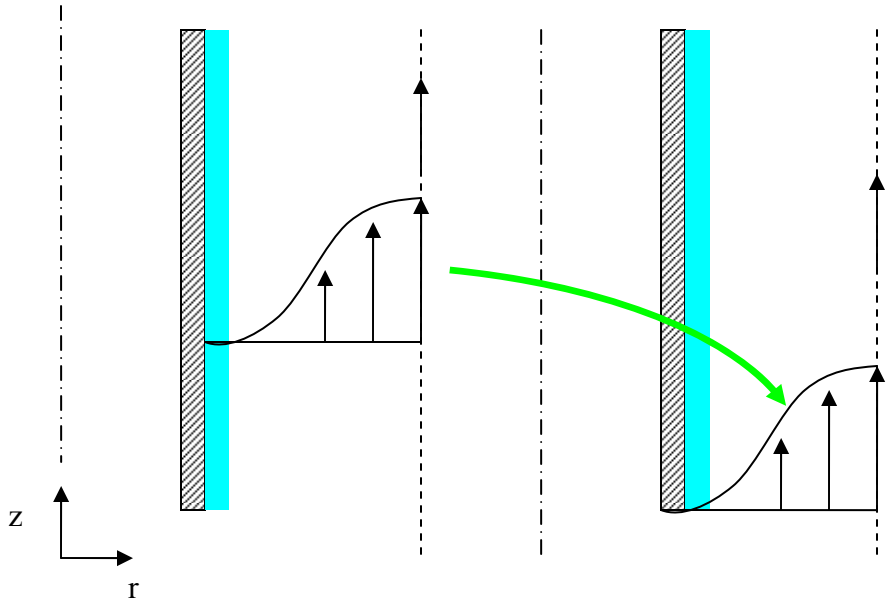

Figure 4.7: A 2D program in the r-z domain calculates the fully-developed velocity profile of the two-phase flow. The velocity profile is then used as the inlet velocity profile of the 3D LCRM model. The outer "wall" moves upward at a constant velocity.

- Laminar Flow

The numerical scheme was first tested by performing the simulation at zero heat flux with no cross flow for laminar flow. This case provides a base reference. Without heating or cross flow, the liquid film should remain uniform throughout the simulation since no disturbance that would cause the interface to move away from its initial equilibrium position occurs. As pointed out in Shin et al. (2005), this type of simulation is extremely difficult because the numerical method should cover both the dynamic and steady equilibrium regions. Our numerical method causes the maximum liquid film thickness to increase by 3% to 1.03×10^{-3} m, as can be seen in Figure 4.8. Because 3% is

very small, this increase should not significantly affect the simulation. The minimum liquid film thickness remains 1.0×10^{-3} m during the entire simulation. With this result, the numerical algorithm can now be used to assess the impact of the forcing functions on film stability and possible dryout formation.

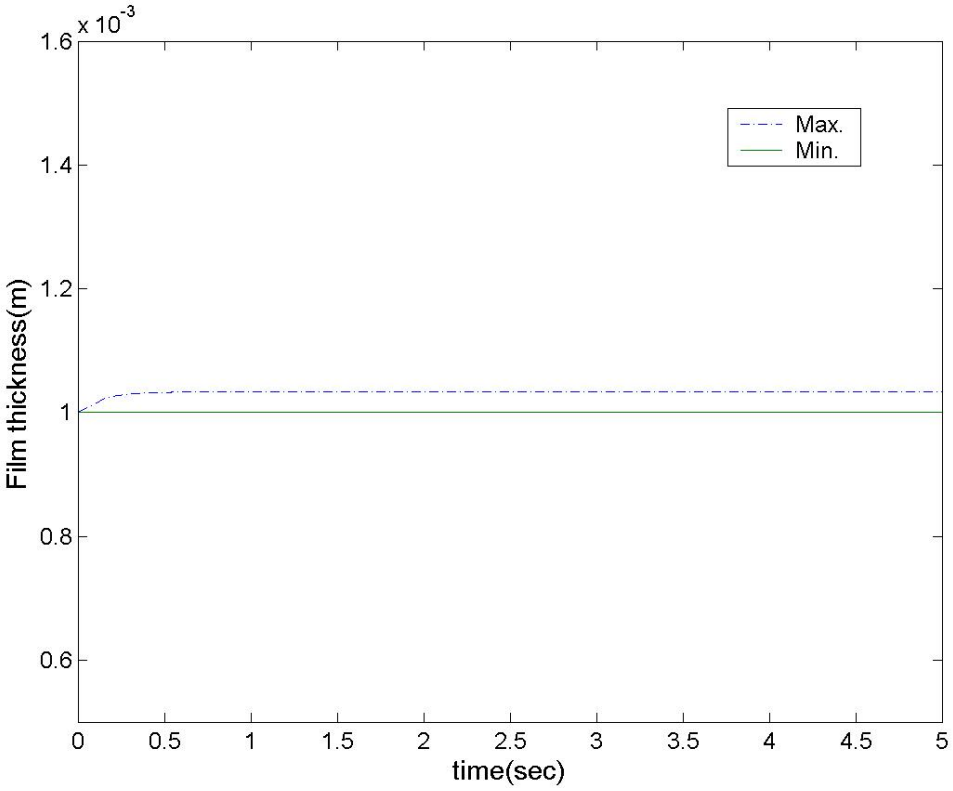

Figure 4.8: Variation of the calculated film thickness with time for the case without heating or cross flow for laminar flow (BFECC method, $\Delta t = 1\times10^{-4}$ s, grid $5\times20\times50$, and the axial "outer" wall velocity is 1.0 m/s)

For nonzero heat flux values, the film thickness is expected to decrease as it proceeds along the rod. As shown in Figure 4.9, the minimum liquid film thickness oscillates slightly in the first 0.4 sec with a wall heat flux, q_w, of 5.0×10^5 W/m^2 for

laminar flow. After 0.4 sec, the minimum liquid film thickness becomes stable. Figure 4.10 shows the detailed interfacial structure along the rod.

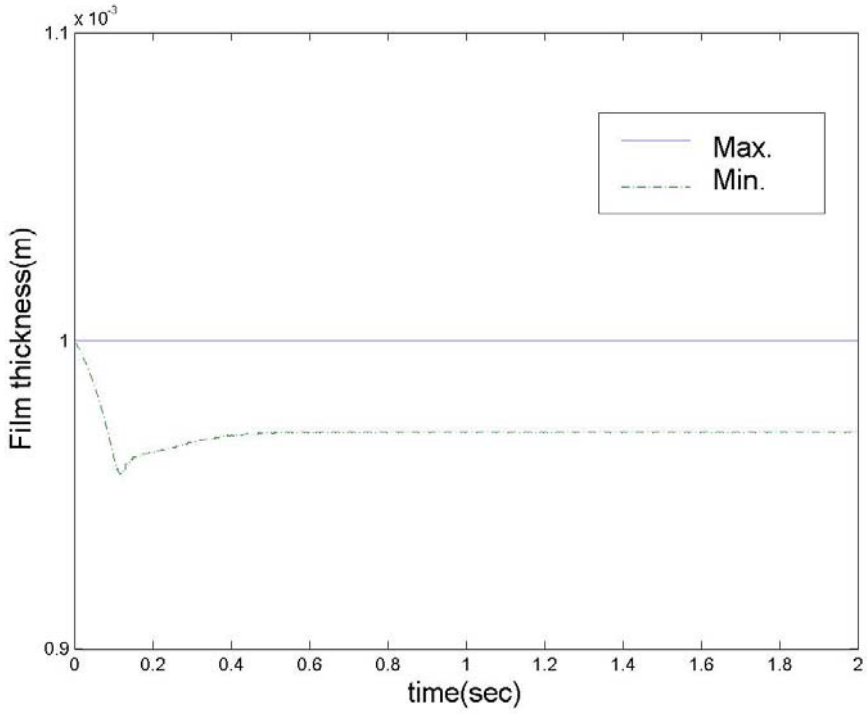

Figure 4.9: Variation of the film thickness with time for uniform heating q_w of 5.0×10^5 W/m^2 for laminar flow (BFECC method, $\Delta t = 1\times10^{-4}$ s, grid $5\times20\times50$, and the axial "outer" wall velocity is 1.0 m/s)

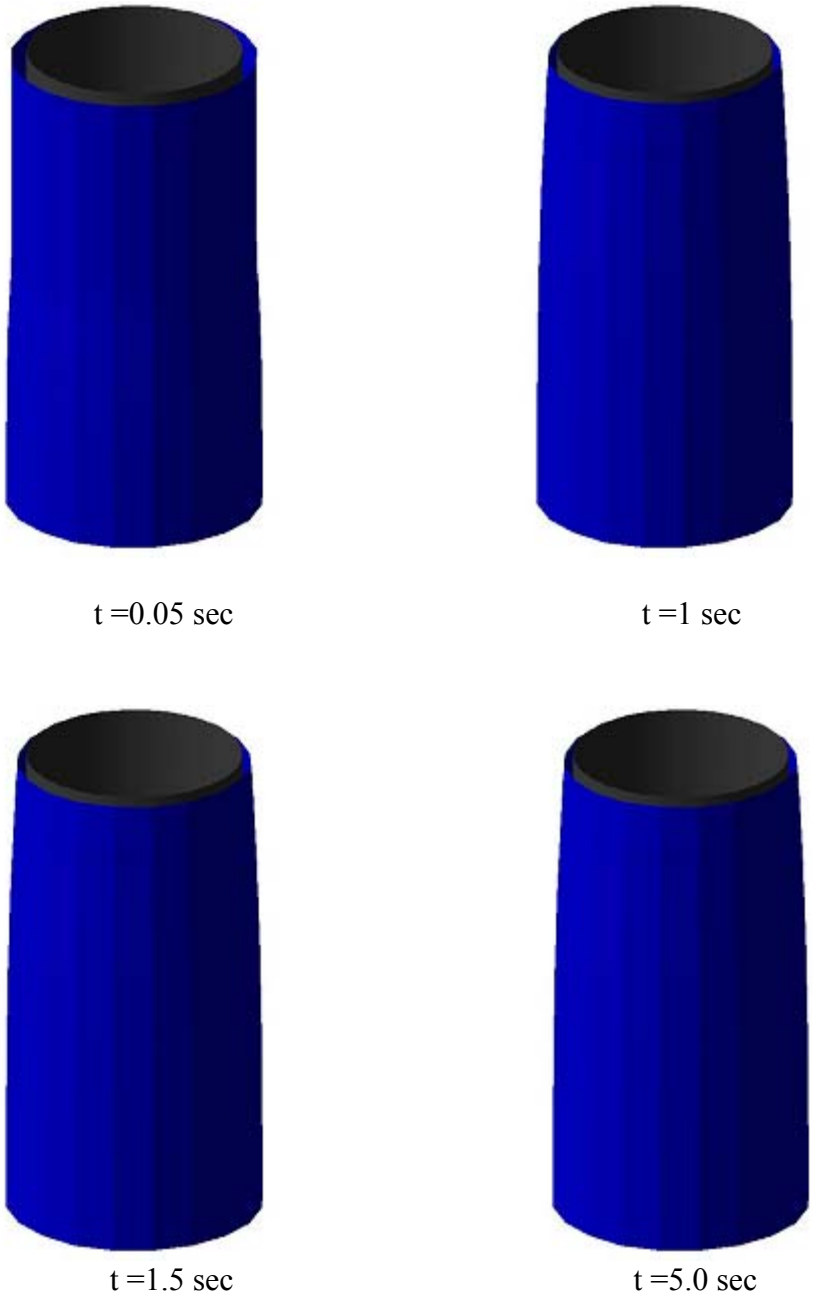

Figure 4.10: Detailed interfacial structure for uniform surface heating time for uniform heating q_w of 5.0×10^5 W/m^2 for laminar flow (Note: This figure is not to scale; the z-dimension has been compressed by a factor of 5, while deviation from the initial radius of the interface of the film has been magnified by a factor of 20 for easier viewing.)

- Turbulent flow

The turbulent effect is simulated by the Standard $k-\varepsilon$ model. Saturated water and steam at 6.9 MPa (1000 psia) is the working fluid. For uniform heat flux at 1.2×10^5 W/m^2, the liquid film oscillates slightly and ultimately approaches a steady minimum and maximum film thickness in Figure 4.11. Figure 4.12 shows the detailed interfacial structure along the rod.

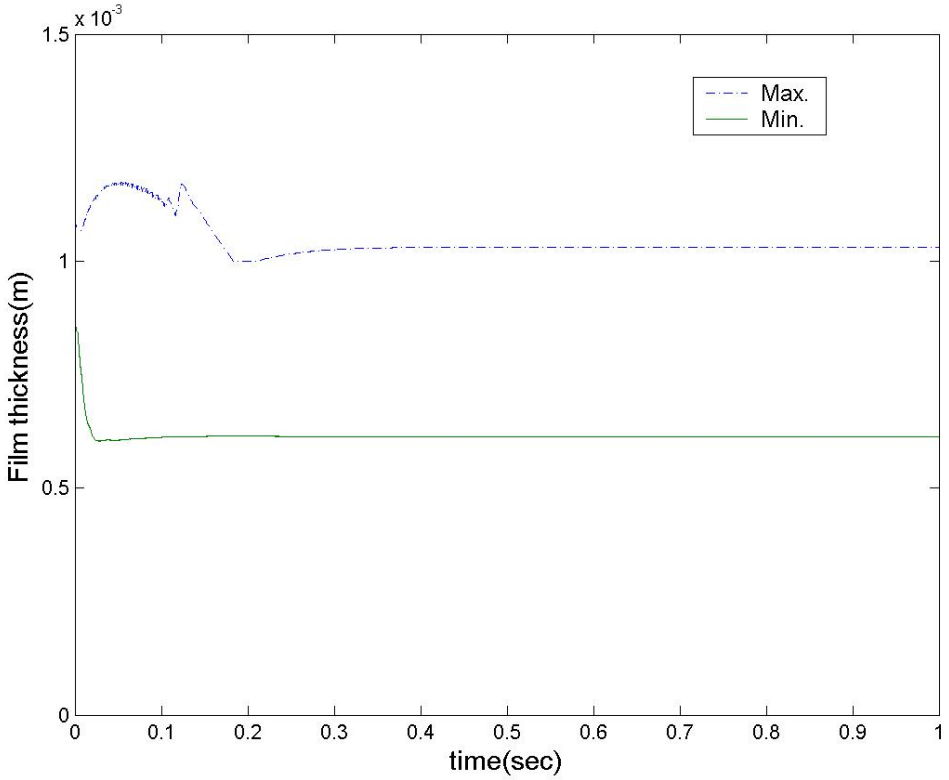

Figure 4.11: Variation of the film thickness with time with uniform heating q_w 1.2×10^5 W/m^2 for turbulent flow (BFECC method, $\Delta t = 1\times10^{-5}$ s, grid $5\times20\times50$, and the axial "outer" wall velocity is 10.0 m/s)

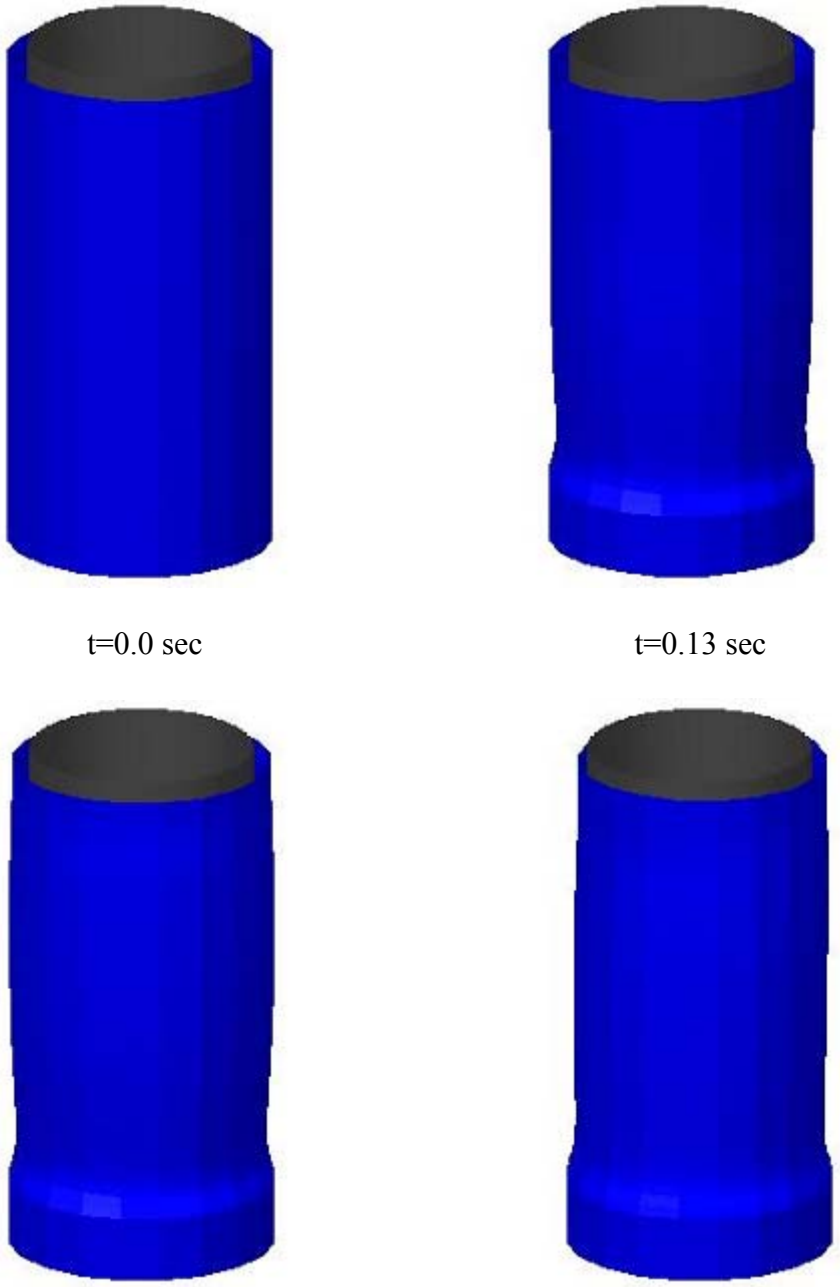

Figure 4.12: Detailed interfacial structure for uniform surface heating q_w of 1.2×10^5 W/m^2 for turbulent flow (Note: This figure is not to scale; the z-dimension has been compressed by a factor of 5 for easier viewing.)

4.3 Prediction of the Critical Heat Flux for Internally-Heated Annuli

In the previous section, we simulated the evaporating thin liquid film on a cylindrical rod for uniform heating by the level contour reconstruction method. In this section our model is applied to the prediction of the critical heat flux for internally-heated annuli, i.e. a heated rod surrounded by an unheated cylindrical shell. For internally-heated annuli, Becker and Hernborg (1964) observed that the liquid film always dried out near the exit of the test section. Based on this observation, to predict the critical heat flux, the LCRM can be applied to the last 10 cm of the test section to simulate the evolution of the liquid film leading to dryout. The program can be run at different heat flux values on the inner rod to determine the heat flux corresponding to dryout (zero film thickness) at the exit, i.e. the critical heat flux (CHF). The simulation results are compared with the experimental data sets obtained by Becker and Hernborg (1964) and Mortimore and Beus (1979).

4.3.1 Becker and Hernborg (1964) Experiment

Becker and Hernborg measured the critical heat flux for internally heated annuli in 1964. In the experiment, the heat flux is kept constant. The mass flow rate is reduced slowly until the liquid film dries out. At dryout, the exit quality and pressure are recorded. The experimental data corresponding to CHF 2.01 and 2.47 (MW/m^2) are shown in Table 4.2.The heating length of the annulus is 0.608 m, the outer tube diameter 0.01742 m, and the inner rod diameter 0.00992 m.

Table 4.2: Exit Pressure and Quality at Dryout (Becker and Hernborg, 1964)

Heat Flux (MW/m^2)	Exit Pressure (bar)	Exit quality	Mass Flux (Kg/m^2s)	Heat Flux (MW/m^2)	Exit Pressure (bar)	Exit quality	Mass Flux (Kg/m^2s)
2.01	15.422	0.162	753.8	2.47	16.472	0.154	978.2
2.01	16.368	0.177	693.3	2.47	18.206	0.158	966.3
2.01	18.239	0.189	654	2.47	20.206	0.170	906
2.01	20.487	0.193	649.4	2.47	20.657	0.172	897.7

The procedure used to predict the critical heat flux using the LCRM is as follows:

1. determine the initial liquid film thickness at the inlet
2. input the material properties
3. calculate the inlet velocity profile based on the calculated initial liquid film thickness and the mass flux
4. run the LCRM model at different heat flux boundary conditions to determine the critical heat flux, i.e. the heat flux corresponding to dryout at the exit

- Initial Liquid Film Thickness Calculation

One important input parameter needed in the LCRM model is the initial liquid film thickness. To determine this parameter, the energy conservation equation is applied to compute the steam quality at the inlet of the simulation domain. From the steam quality, the correlation by Furukawa and Sekoguchi (1986) is employed to calculate the void fraction. The void fraction is then used to determine the liquid film thickness. The detail steps used to calculate the liquid film thickness in the experiment of Becker and Hernborg (1964) are illustrated below.

- Simulation Domain

The simulation domain is in the last 10 cm of the test section. In this simulation domain, the flow type is assumed to be annular flow.

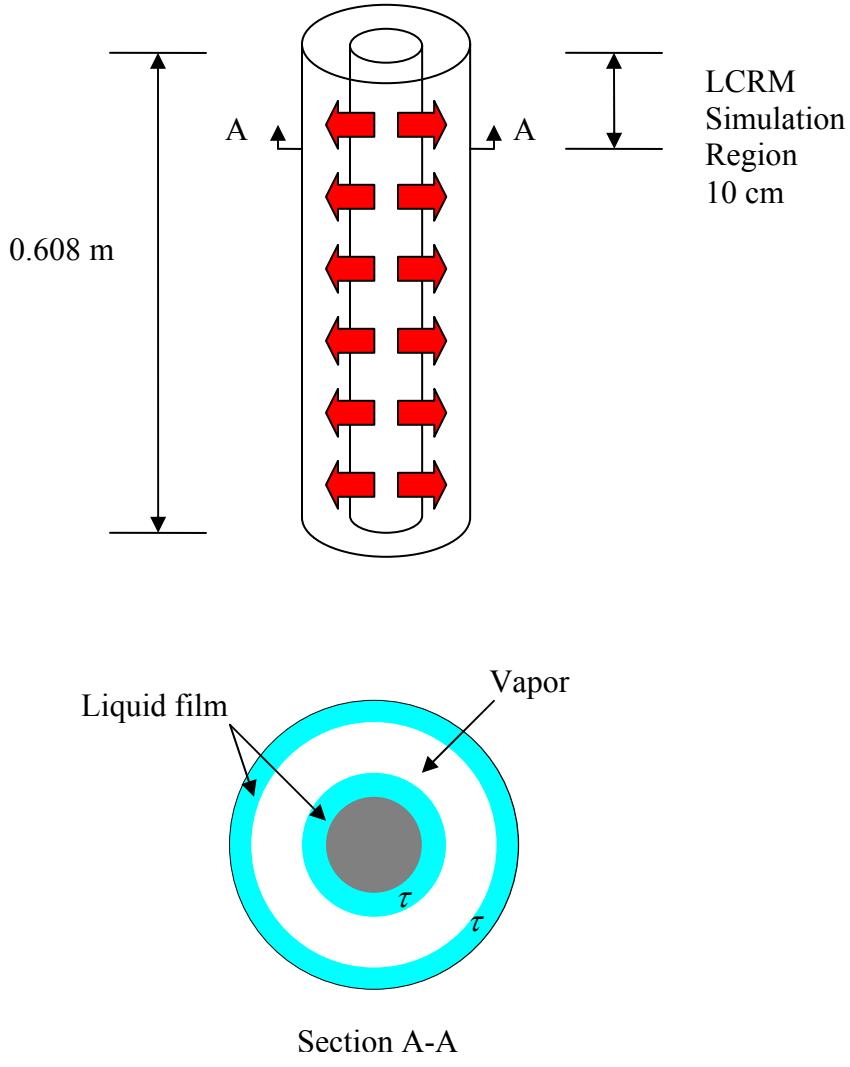

Figure 4.13: LCRM simulation region in the experiment of Becker and Hernborg (1964)

In this annular flow region, it is assumed that a liquid film exists on both the inner rod and the outer tube as shown in Figure 4.13. In the inlet of the simulation domain, section A-A, the two liquid films are assumed to have the same thickness.

- Calculating Quality at Section A-A and Mass Flux

The energy balance equation, along with the experimental data, is used to calculate the enthalpy at section A-A, $h_{\text{A-A}}$. The exit quality X_{exit}, critical heat flux $q_{\text{cr,exp}}$, and inner diameter D_i are used. The latent heat h_{fg} is obtained by looking up the steam table at the exit pressure of the experiment. The inlet subcooling for the 0.608 m long test section is zero. The enthalpy at inlet is

$$h_{in} = h_f \,. \tag{4.7}$$

The mass flux can, therefore, be calculated by the energy balance equation

$$\dot{m}(h_{exit} - h_{in}) = \dot{m} \cdot X_{exit} \cdot h_{fg} = q_{cr,\text{exp}} \cdot \pi \cdot D_i \cdot (0.608m) \,. \tag{4.8}$$

The energy balance equation is applied again, then the quality at section A-A, $X_{A\text{-}A,}$ can be obtained as follows:

$$\dot{m}(h_{A-A} - h_{in}) = \dot{m} \cdot X_{A-A} \cdot h_{fg} = q_{cr,\text{exp}} \cdot \pi \cdot D_i \cdot (0.508m) \,. \tag{4.9}$$

- Calculating Void Fraction α at Section A-A

Once the quality is calculated, the proper correlation is needed to calculate the void fraction. However, a validated correlation of void fraction for water and steam in

annuli was not found in the open literature. Instead, a correlation proposed by Furukawa and Sekoguchi (1986) for air-water two-phase flow in annuli is found. This correlation is used to calculate the void fraction in our model. The Furukawa and Sekoguchi (1986) correlation is

---

pressure:102~159 kPa
water temperature: 33 °C
superficial air velocity, j_g :0.2~20 m/s
superficial water velocity, j_l :0.1~2.0 m/s
diameter ratio D_i / D_o 5/13, 8/13, 10/13

$$\alpha = 0.616\beta\left(\frac{j_g + j_l}{\sqrt{gDeU}}\right)^{0.118} \quad \alpha > 0.75$$

$$\frac{j_g}{\alpha\sqrt{gDeU}} = 1.28\left(\frac{j_g + j_l}{\sqrt{gDeU}}\right) + 0.35 \quad \alpha \le 0.75 \tag{4.10}$$

$$\beta = \frac{j_g}{j_g + j_l}$$

$$DeU = D_o + D_i\psi^{1/\psi}$$

$$\psi = \frac{D_o}{D_o - D_i}$$

$$j_l = G(1-X)v_l$$

$$j_g = GXv_g$$

$$g = 9.8 \text{ m/s}^2$$

After the void fraction is determined from the Furukawa and Sekoguchi (1986) correlation, the slip ratio is calculated by the relation:

$$\alpha = \frac{1}{1 + \frac{1-X}{X}\frac{\upsilon_f}{\upsilon_g}Slip} \ . \tag{4.11}$$

However, the prediction with the slip ratio by the Furukawa and Sekoguchi (1986) correlation tends to underestimate the CHF by 50%, as shown in Figure 4.13. In view of this, we multiply the $(\text{slip ratio})_{\text{F-S(1986) correlation}}$ by an empirical correction factor of 1.3 or 1.4.

$$(\text{slip ratio})_{\text{sim}} = (\text{slip ratio})_{\text{F-S (1986) correlation}} \times (\text{correction factor 1.3 or 1.4}) . \qquad (4.12)$$

The void fraction is calculated again by Eq. 4.11 with $(\text{slip ratio})_{\text{sim}}$.

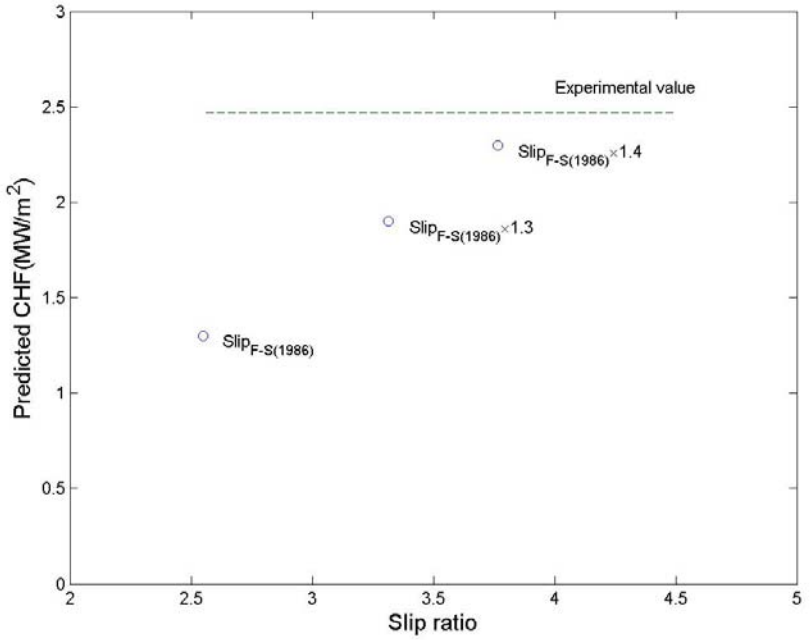

Figure 4.14: Variation of the CHF prediction with the slip ratio. Value calculated based on film thickness from the Furukawa and Sekoguchi (1986) correlation tends to underestimate CHF by 50% (Pressure 18.206 bar, BFECC method, $\Delta t = 1 \times 10^{-6}$ s, and grid $6 \times 24 \times 42$)

- Calculate the Liquid Film Thickness τ

At time=0 sec, we assumed that the inner and the outer liquid film are with the same thickness τ . The liquid film thickness can be calculated from the void fraction based on the area fraction of vapor by Eq. 4.13.

$$\alpha = \frac{\frac{\pi}{4}(D_o - 2\tau)^2 - \frac{\pi}{4}(D_i + 2\tau)^2}{\frac{\pi}{4}(D_o - D_i)^2} \quad . \tag{4.13}$$

The liquid film thickness calculated from Eqs. 4.11, 4.12, and 4.13 increases as the slip ratio increases, as shown in Figure 4.13.

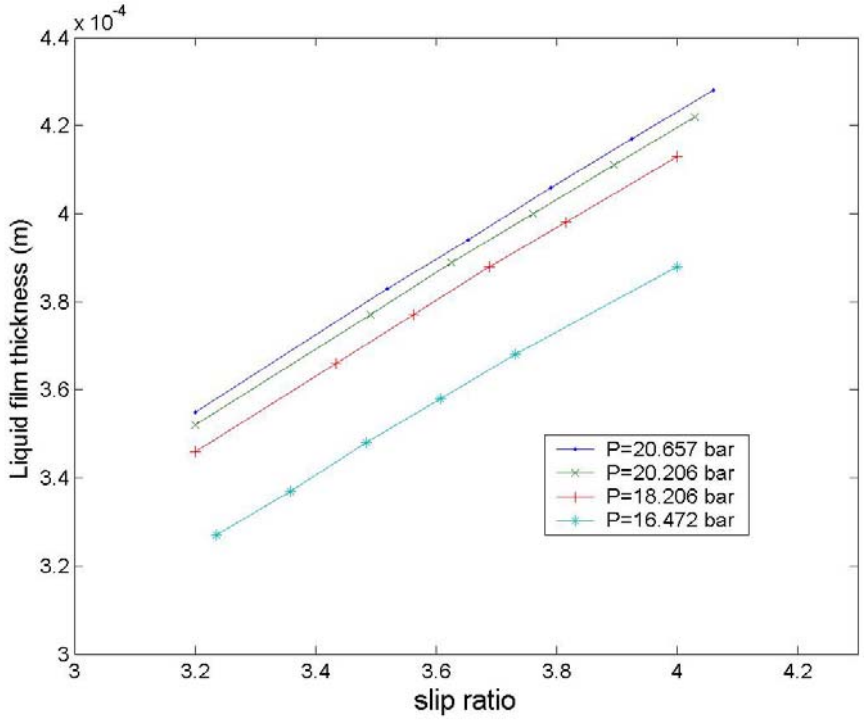

Figure 4.15: The liquid film thickness for different slip ratio calculated using Eqs. 4.11, 4.12, and 4.13 at CHF 2.47 (MW/m^2)

Although there are two liquid films in this annulus, the outer liquid film does not dry out (Becker and Herborg, 1964). In our simulation, we ignore the outer liquid film on

the unheated shroud, assuming that its movement does not affect the critical heat flux prediction for the inner heated rod. Only the inner liquid film is simulated by our level contour reconstruction method. Vapor occupies the rest of the area as seen in Figure 4.16. The outer film plays a role only in the film thickness calculation of Eq. 4.13. The inner liquid film thickness is set as τ from Eq. 4.13. The material properties used in the simulation are presented in Table 4.5.

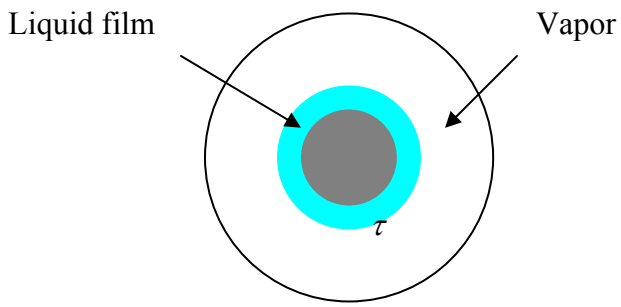

Figure 4.16: Schematic Diagram of the Model Geometry--Only the liquid film on the inner rod is simulated in our model. The outer film is ignored, and it is assumed that vapor is filled by the rest of the space

- Calculate the Inlet Velocity Profile

A program has been created to calculate the fully-developed velocity profile of the two-phase flow within the annulus as presented in Figure 4.17. This fully-developed velocity profile is calculated by simulating a flow with uniform velocity at the inlet flowing through a long annulus in the r-z domain. The flow reaches fully-developed conditions as its velocity profile does not change in the axial direction. This fully-developed velocity profile is employed as the inlet velocity profile of the computational domain for the 3D Level Contour Reconstruction Method.

Table 4.3: Material properties used in the simulation of Becker and Hernborg (1964) experiment

	P=16.472 bar	P=18.206 bar	P=20.206 bar	P=20.657 bar
Liquid density (Kg/m^3)	861.5	855.6	849.2	847.8
Steam density (Kg/m^3)	8.31	9.158	10.14	10.36
Liguid viscosity ($N\text{-}Sm^2$)	1.324e-4	1.291e-4	1.258e-4	1.251e-4
Steam viscosity ($N\text{-}S/m^2$)	1.581e-5	1.598e-5	1.616e-5	1.62e-5
Liquid conductivity (W/m^oC)	0.6491	0.6462	0.6427	0.642
Steam conductivity (W/m^oC)	0.04046	0.0414	0.04243	0.04265
Liquid specific heat (J/kg^oC)	4503	4529	4559	4566
Steam specific heat (J/kg^oC)	2835	2906	2988	3006
Latent heat (J/kg)	1.929e6	1.909e6	1.888e6	1.883e6
Surface tension (N/m)	0.03703	0.03591	0.0347	0.03444
Saturation temperature (^oC)	202.9	207.8	213.1	214.2

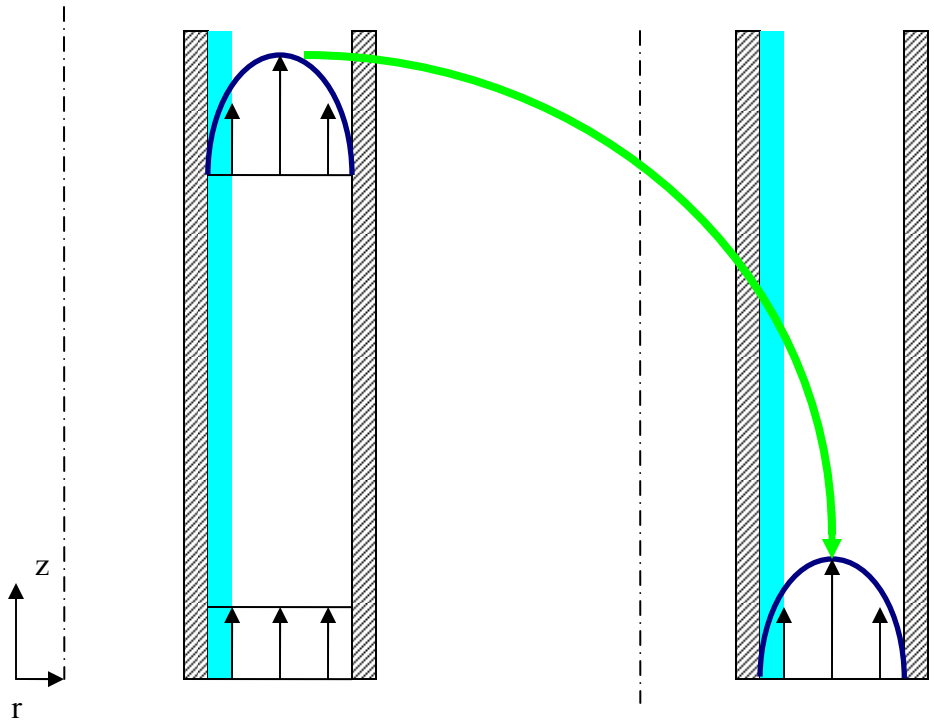

Figure 4.17: A 2D program in the r-z domain calculates the fully-developed velocity profile of the two-phase flow in annuli. The velocity profile is used as the inlet velocity profile of the 3D LCRM model. Both inner and outer walls are stationary.

- Steady-State CHF Prediction Results

Figures 4.18 to 4.21 illustrate the steady-state CHF prediction results versus liquid film thickness at different exit pressures. Referring to Fig. 4.18, for a given initial film thickness, mass flux, and pressure, the film thickness corresponding to a given heat flux is calculated. When a non-zero exit film thickness is calculated, a "no-dryout" result is noted. As the assumed heat flux value increases, dryout is reached at the exit. The CHF is calculated by interpolation between the last-calculated "dryout" and "no dryout" cases. The results in Figures 4.18, 19, 20, and 21 correspond to different pressure with slightly

different mass flux values. All calculations are performed using the BFECC method with mesh $6 \times 24 \times 42$, and $\Delta t = 1.0 \times 10^{-6}$ sec. As expected, these four figures show that the predicted CHF increases as the liquid film thickness increases.

Figure 4.22 shows the effect of slip on the predicted CHF at different pressures. The slip ratio predicted by the Furukawa and Sekoguchi (1986) model was multiplied by an empirical correction factor of either 1.3 or 1.4. In this figure, the simulation results obtained using the BFECC method with the slip ratio correction factor of 1.4 yields the best result. With the correction factor 1.4, the predicted CHF values are 3-23% lower than the experimental value CHF_{exp} of 2.47 MW/m^2. Figure 4.22 also compares the predicted CHF values obtained using either the CIR or the BFECC method with the same slip empirical factor (1.3). The results show that the BFECC method yields better results than the CIR method; the BFECC improves the CHF prediction by 11-20% versus the CIR method. The progressive simulation results leading to the predicted CHF values shown in Figure 4.22 can be found in Figures 4.23 to 4.25. Figure 4.26 shows the CHF prediction results for a lower mass flux corresponding to an experimental CHF_{exp} value of 2.01 (MW/m^2). Here only the predictions obtained using the BFECC method and a slip correction factor of 1.4 are shown. The predicted CHF is 20-40% lower than the experimental CHF.

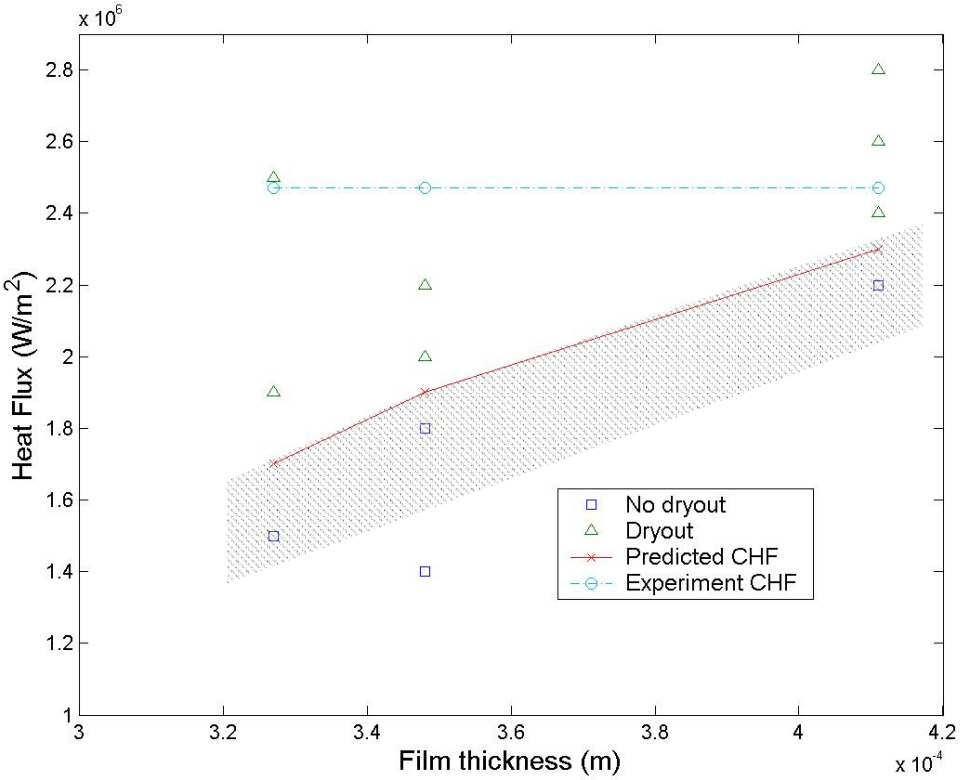

Figure 4.18: Variation of predicted CHF with film thickness at pressure 16.472 (bar) and mass flux 978.2 (Kg/m^2-s) (BFECC method, mesh $6\times24\times42$, and $\Delta t=1.0\times10^{-6}$ sec)

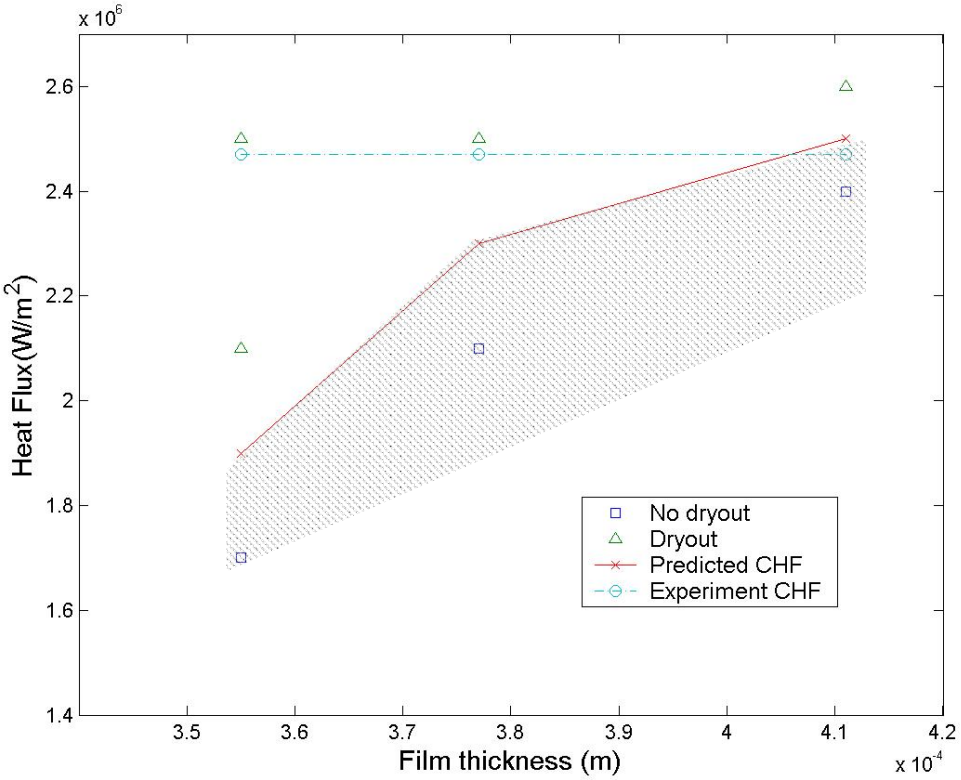

Figure 4.19: Variation of predicted CHF with film thickness at pressure 18.206 (bar) and mass flux 966.3(Kg/m^2-s) (BFECC method, mesh $6\times24\times42$, and $\Delta t=1.0\times10^{-6}$ sec)

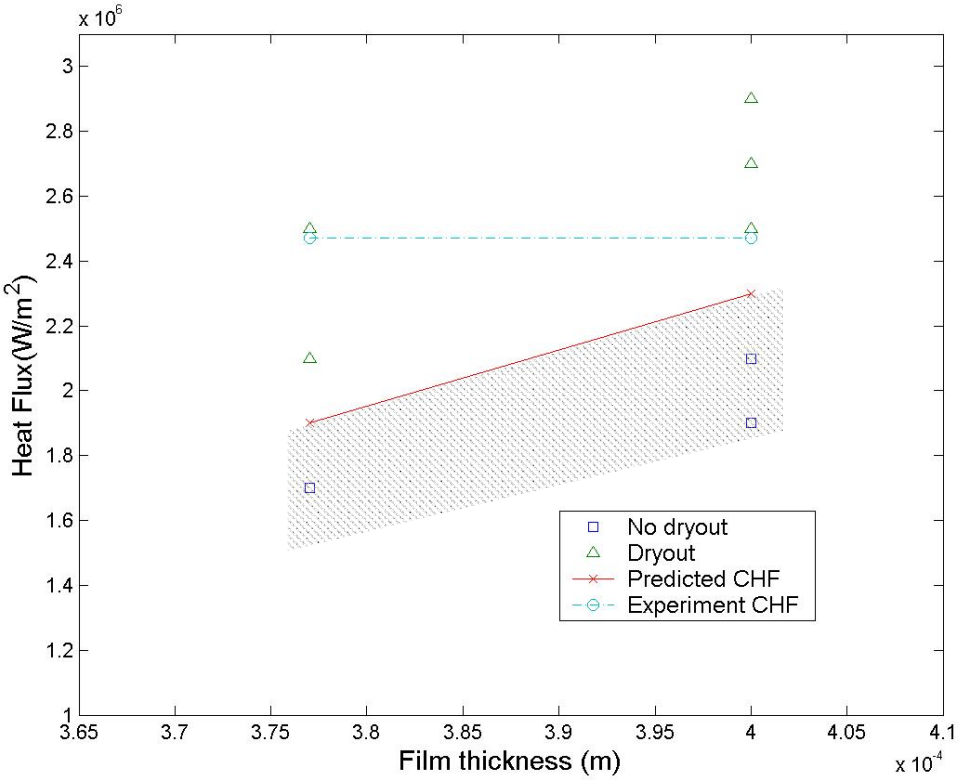

Figure 4.20: Variation of predicted CHF with film thickness at pressure 20.206 bar and mass flux 906 (Kg/m^2-s) (BFECC method, mesh $6\times24\times42$, and $\Delta t=1.0\times10^{-6}$ sec)

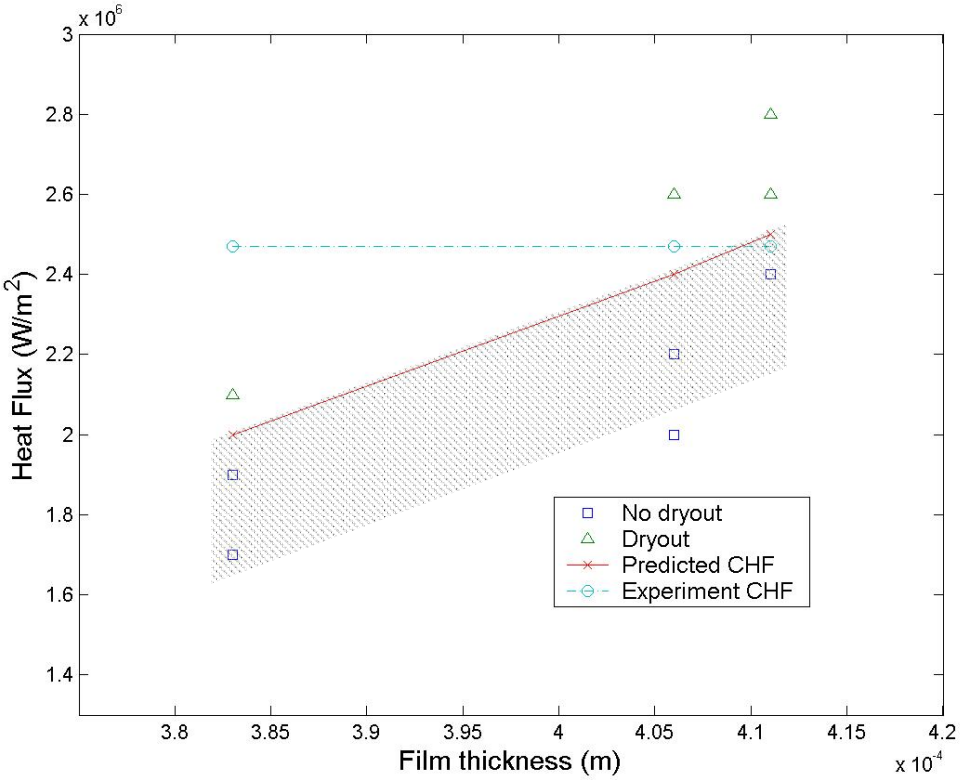

Figure 4.21: Variation of predicted CHF with film thickness at pressure 20.657(bar) and mass flux 897.7 (Kg/m^2-s) (BFECC method, mesh $6\times24\times42$, and $\Delta t=1.0\times10^{-6}$ sec)

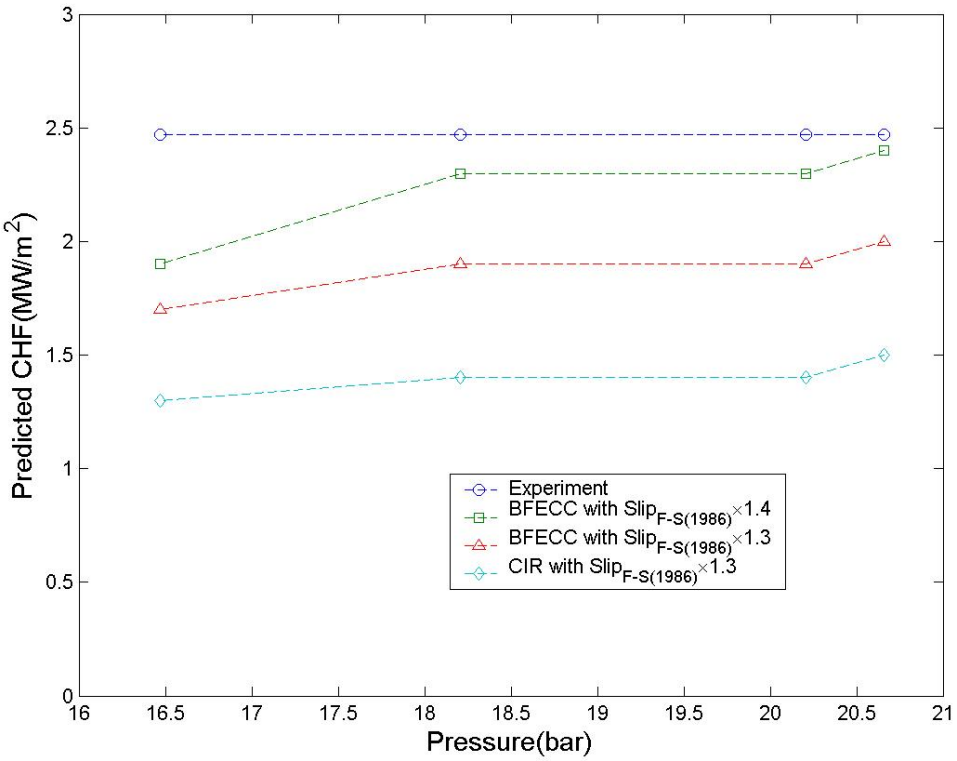

Figure 4.22: Steady-state CHF prediction results at different pressure (mesh $6\times24\times42$ and $\Delta t=1.0\times10^{-6}$ sec)

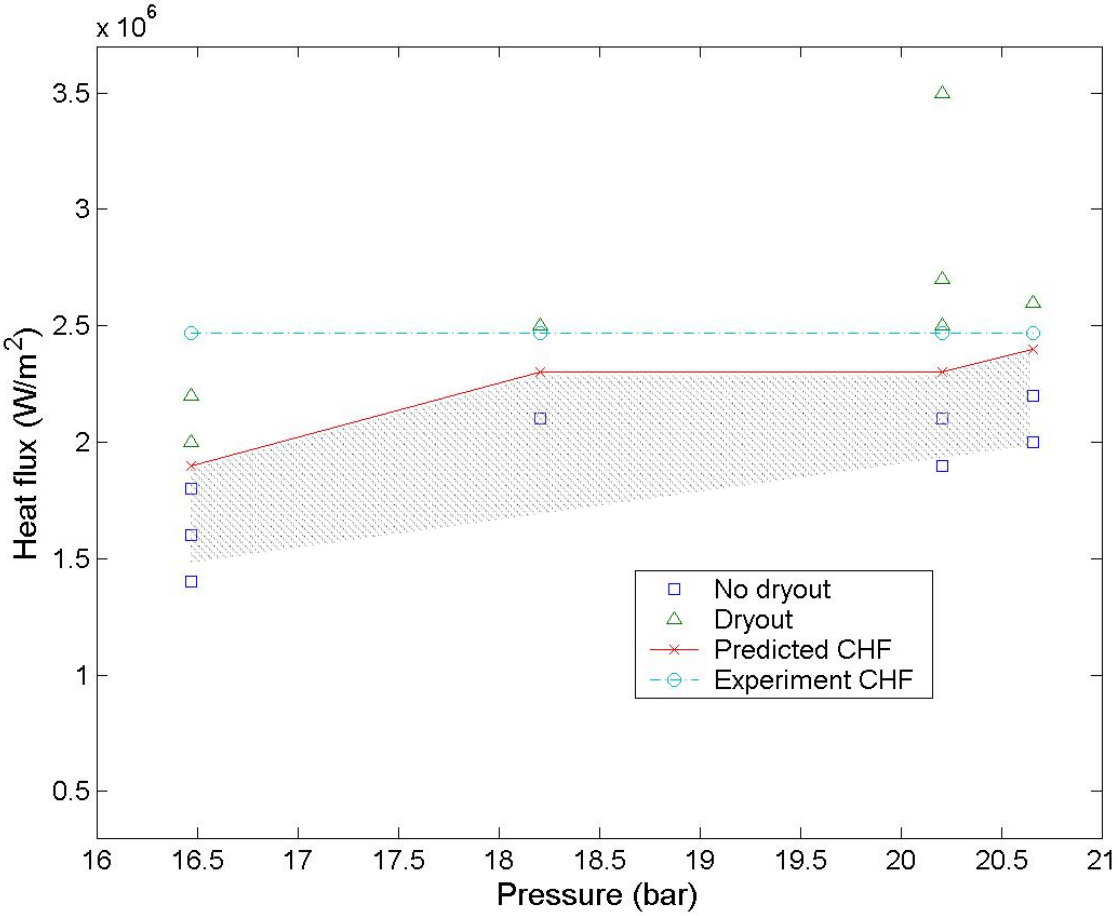

Figure 4.23: Steady-state CHF prediction results (slip ratio=Furukawa and Sekoguchi (1986) correlation$\times$ 1.4, BFECC method, mesh $6\times 24\times 42$, and $\Delta t=1.0\times 10^{-6}$ sec)

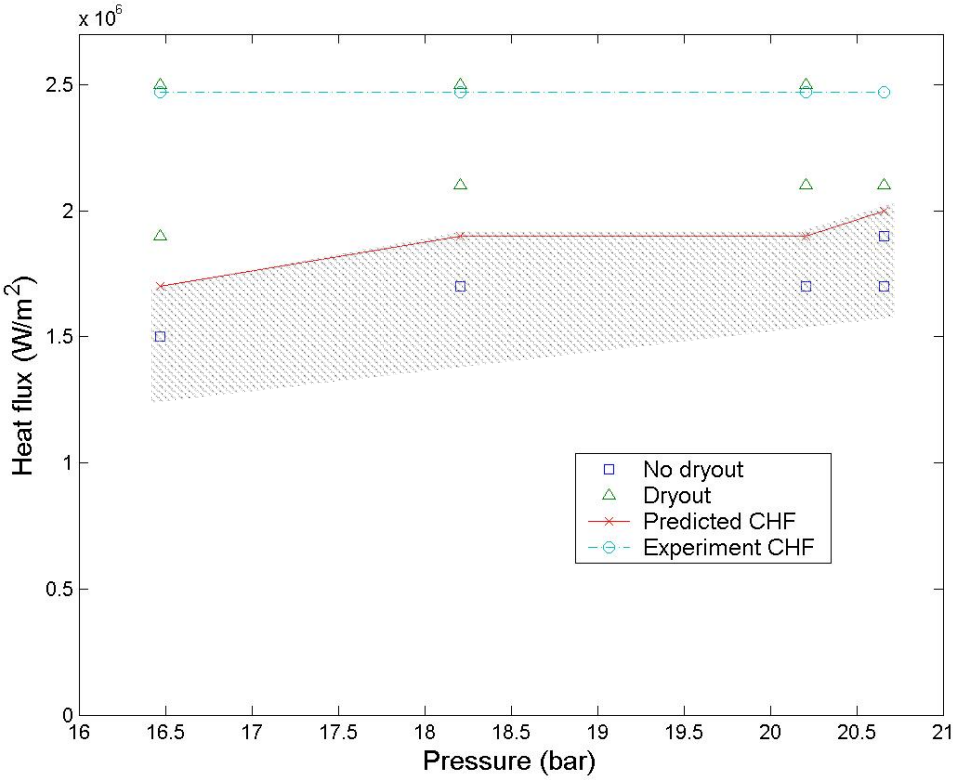

Figure 4.24: Steady-state CHF prediction results (slip ratio=Furukawa and Sekoguchi (1986) correlation$\times$ 1.3, BFECC method, mesh $6\times24\times42$, and $\Delta t=1.0\times10^{-6}$ sec)

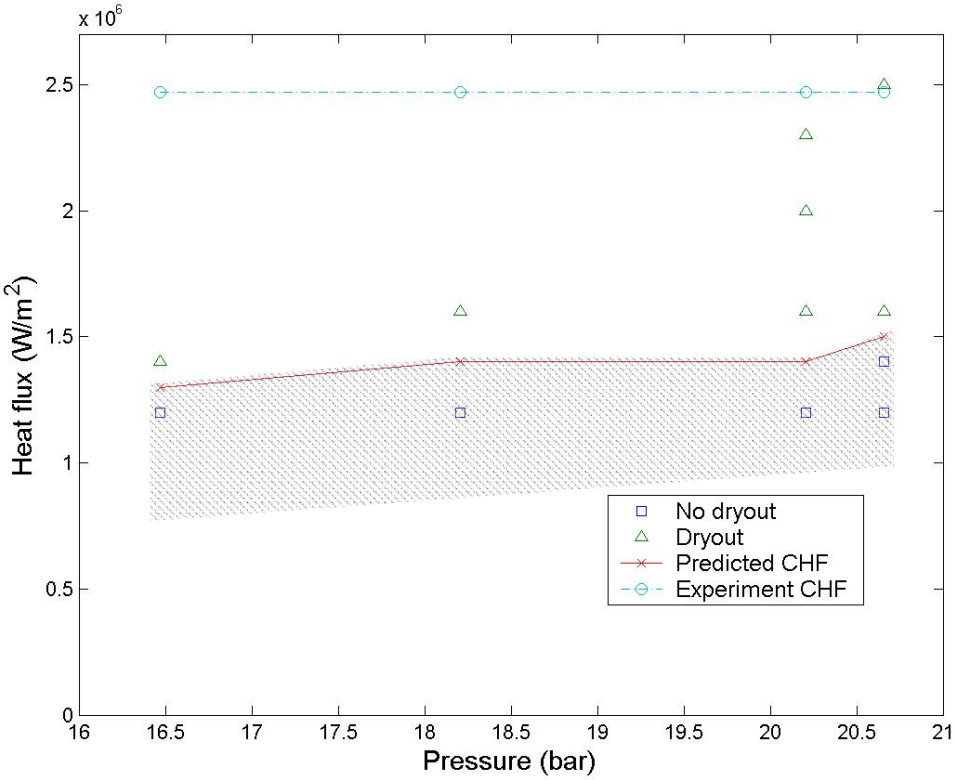

Figure 4.25: Steady-state CHF prediction results (slip ratio=Furukawa and Sekoguchi (1986) correlation× 1.3, CIR method, mesh 6×24×42, and $\Delta t=1.0\times10^{-6}$ sec)

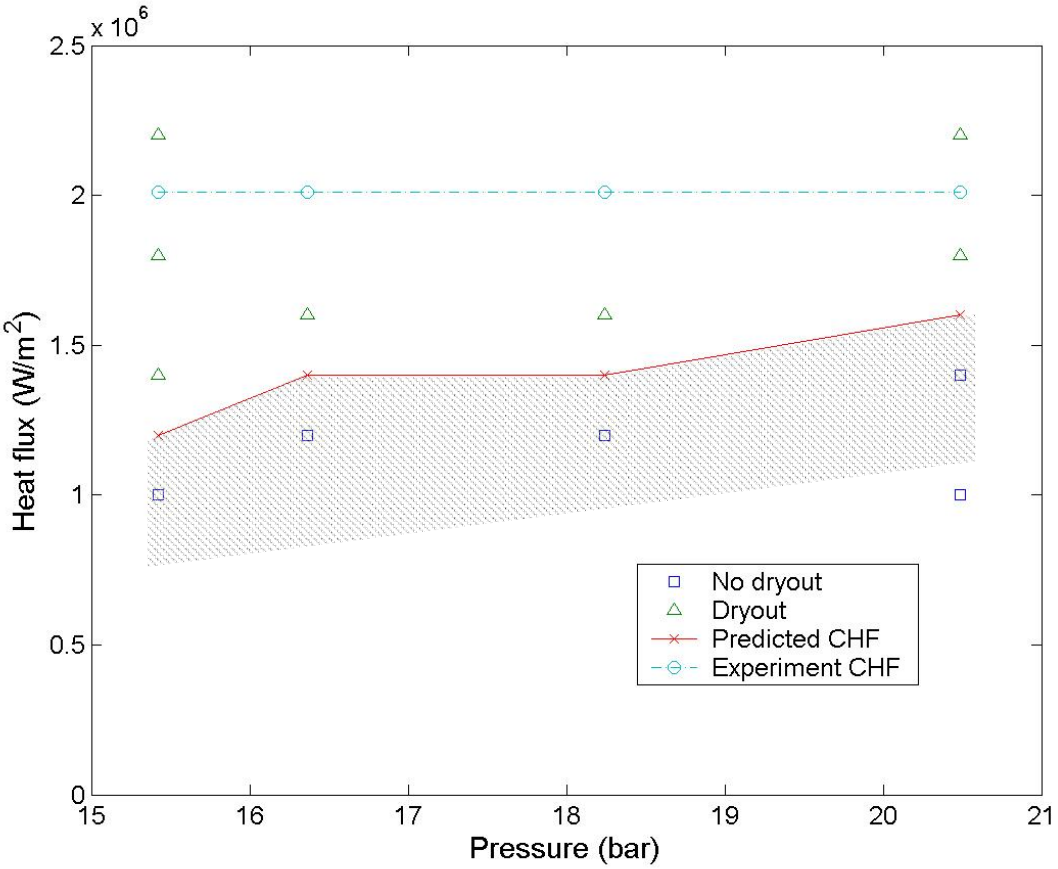

Figure 4.26: Steady-state CHF prediction results (slip ratio=Furukawa and Sekoguchi (1986) correlation$\times$ 1.4, BFECC method, mesh $6\times24\times42$, and $\Delta t=1.0\times10^{-6}$ sec)

- Transient CHF Prediction--Simulation for Different Mass Flux Reduction Rates

In the Becker and Hernborg (1964) experiment, the heat flux is kept constant. The mass flux is gradually reduced until the liquid film dries out. To better simulate the dry out process, we follow the experimental procedure in our numerical simulation to predict the exit quality at dryout for different mass flux reduction rates. One advantage of the Level Contour Reconstruction Method is that it allows us to simulate the liquid film movement at different boundary conditions. For example, one simulation with a mass flux reduction rate 9.36×10^{7} (Kg/m^2-s)/hr is shown in Figure 4.27. We first run the simulation at a high mass flux (1.5 times the experimental dryout mass flux) until it

reaches steady state. It takes 0.02 seconds. The liquid film does not dry out at this high mass flux. After the liquid film reaches steady state conditions at 0.02 second, the mass flux is decreased at a prescribed mass flux reduction rate until the liquid film dries out. In the simulation, the mass flux is reduced by decreasing the velocity at the inlet of the calculation domain while keeping the same inlet film thickness in Eq. 4.13. At dryout, we recorded the mass flux. The exit quality at dryout can then be calculated by the energy balance equation.

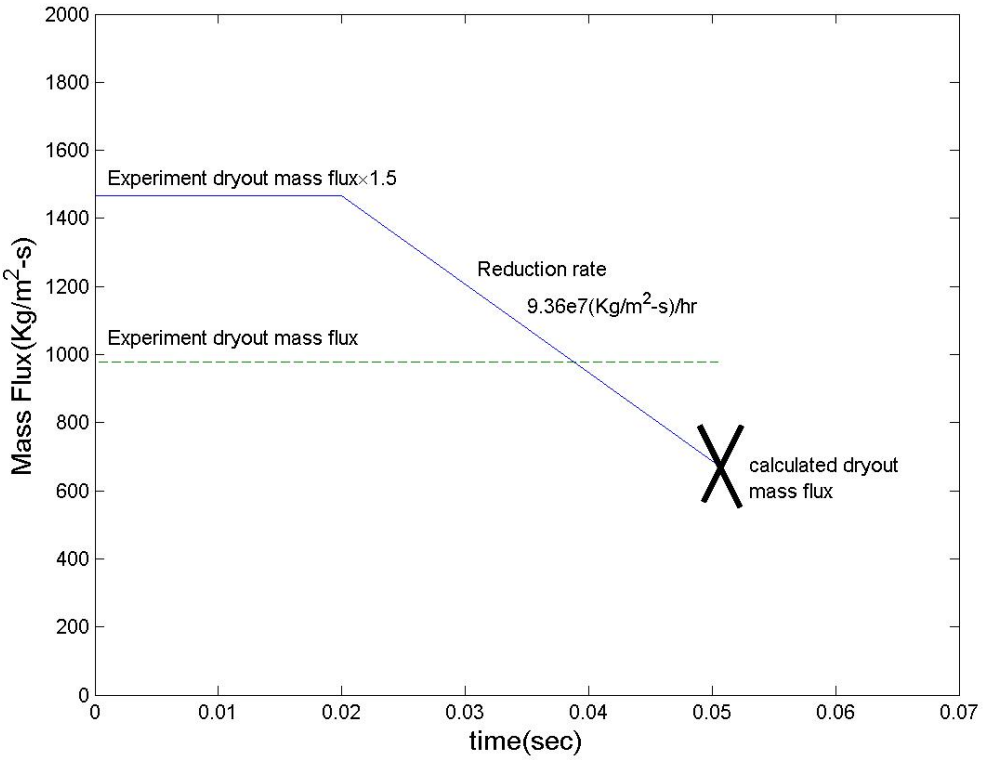

Figure 4.27: Mass flux setting at the mass flux reduction rate 9.36×10^{7} (Kg/m^2-s)/hr.

We then test the sensitivity of the initial mass flux setting in the simulation. Figure 4.28 shows that exit quality at dryout predicted in the simulation for different initial mass flux values at the same mass flux reduction rate. The figure shows that the

prediction results of the exit quality at dryout do not significantly change for different initial mass flux values. The exit quality is not sensitive to the initial mass flux used to establish the starting steady state condition.

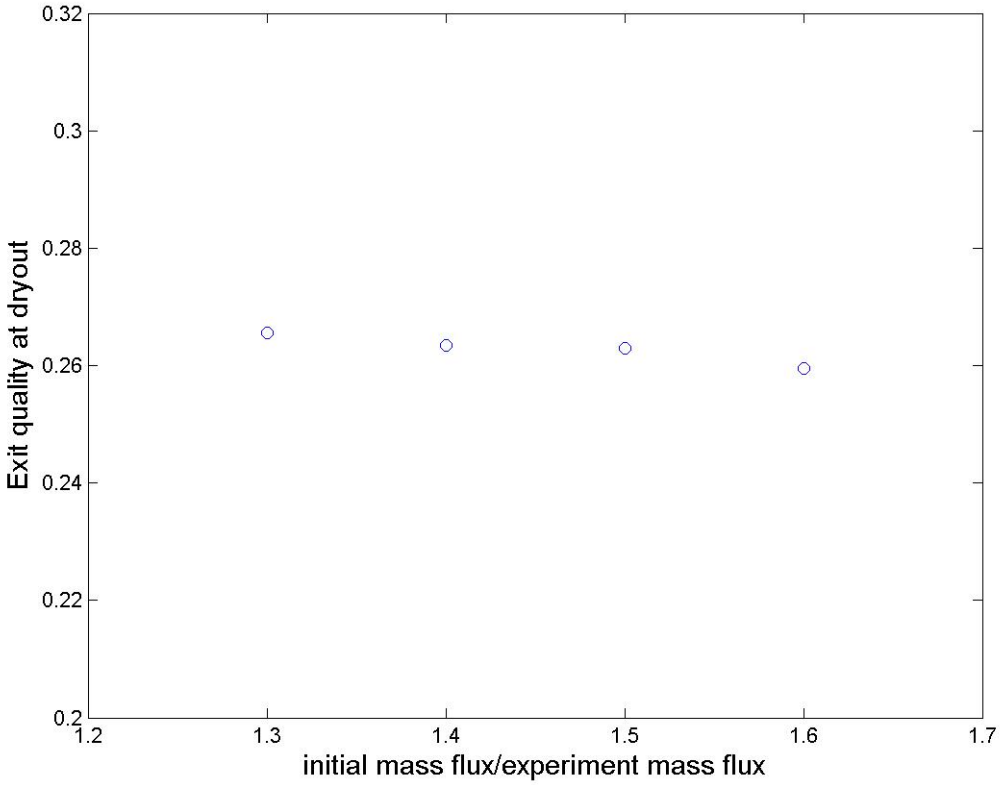

Figure 4.28: Exit quality at dryout for different initial mass flux (CHF 2.47 MW/m^2, mass flux reduction rate 9.36e7 (Kg/m^2-s)/hr, and pressure 18.206 (bar), mesh $6\times24\times42$, and $\Delta t=1.0\times10^{-6}$ sec)

Figure 4.29 shows that the mass flux at dryout obtained in the simulation decreases as the mass flux reduction rate increases. The higher the mass flux reduction rate, the lower the mass flux at dryout is. From the energy balance equation, we can calculate the exit quality at dryout from the dryout mass flux in Figure 4.29. The results are shown in

Figure 4.30. It shows the exit quality at dryout will be higher at high mass flux reduction rates. This result confirms the observation that the use of steady state CHF values in transient analysis is generally conservative. The level of conservation increases as the transient becomes more rapid.

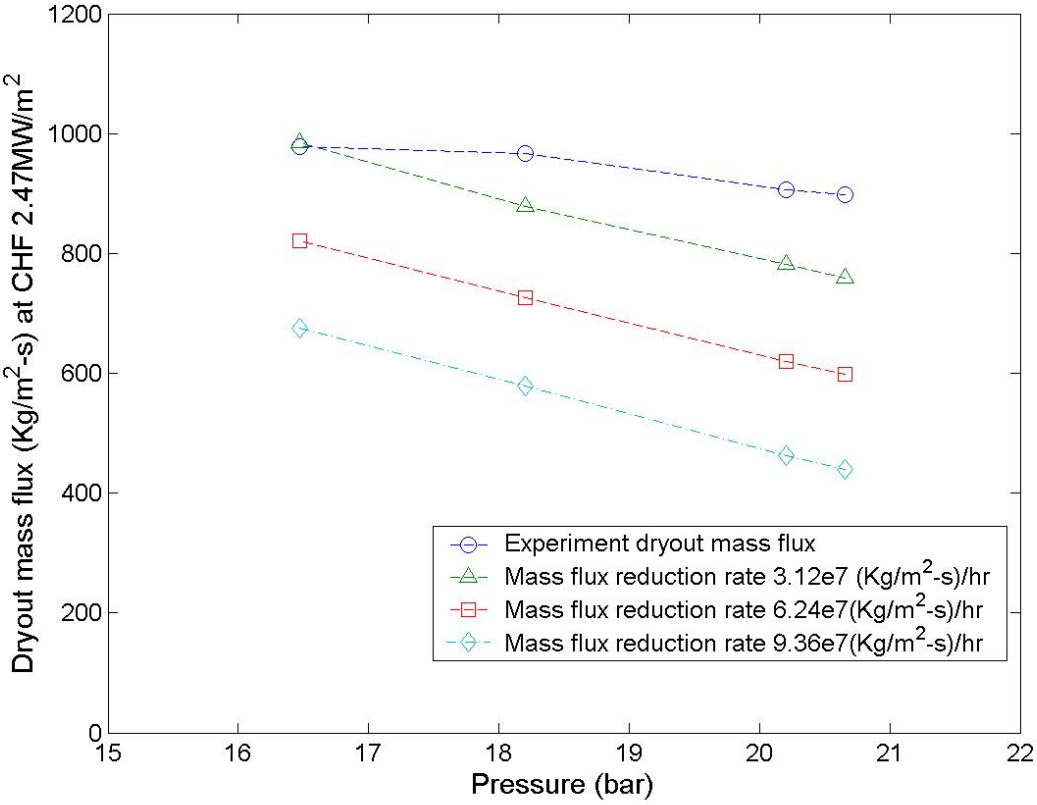

Figure 4.29: Dryout mass flux at CHF 2.47 MW/m^2 for different mass flux reduction rates. (Slip ratio=Furukawa and Sekoguchi (1986) correlation$\times$1.4, initial mass flux=1.5 $\times$experiment mass flux, mesh $6\times24\times42$, and $\Delta t=1.0\times10^{-6}$ sec)

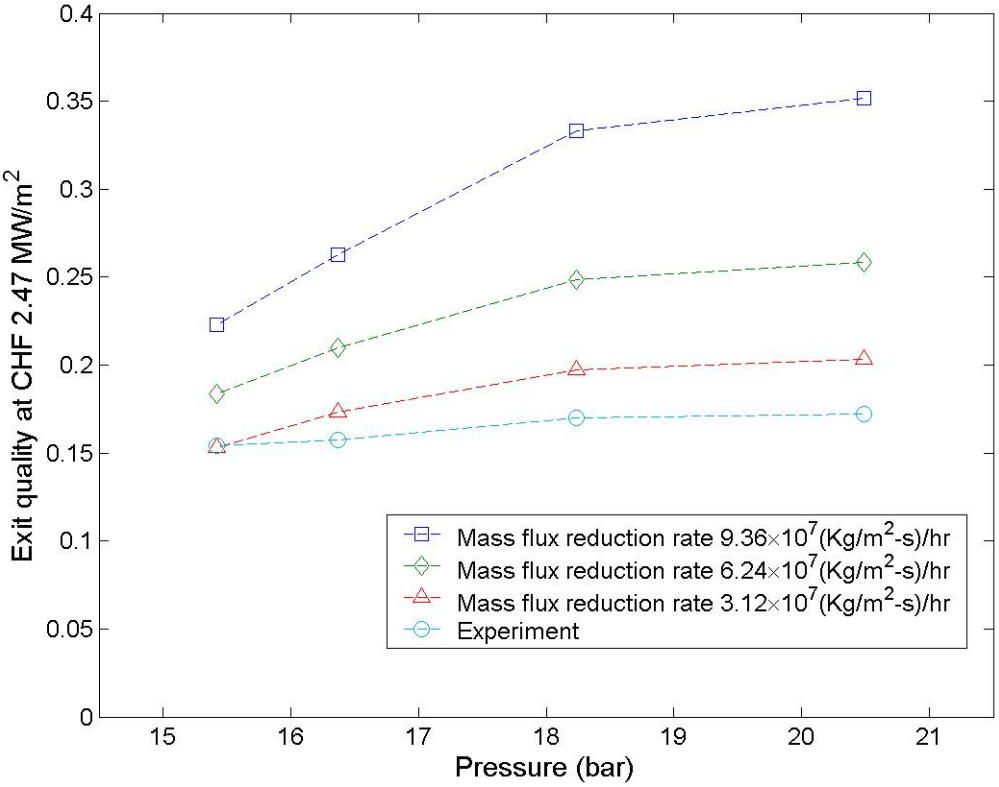

Figure 4.30: Exit quality at dryout at CHF 2.47 MW/m^2 for different mass flux reduction rates. (Slip ratio=Furukawa and Sekoguchi (1986) correlation$\times$1.4, initial mass flux=1.5 $\times$ experiment mass flux, mesh $6\times24\times42$, and $\Delta t=1.0\times10^{-6}$ sec)

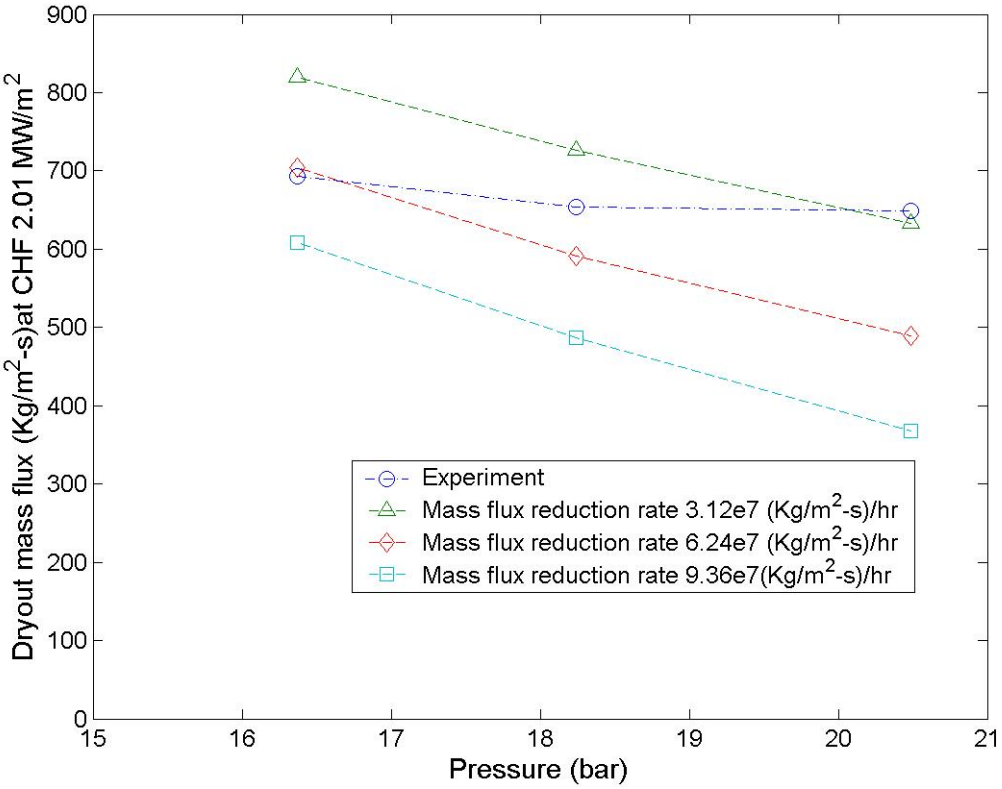

Figure 4.31: Dryout mass flux at CHF 2.01 MW/m^2 for different mass flux reduction rates (slip ratio=Furukawa and Sekoguchi (1986) correlation$\times$1.4, initial mass flux=1.5 $\times$ experiment mass flux, mesh $6\times24\times42$, and $\Delta t=1.0\times10^{-6}$ sec)

Figure 4.31 shows that the dryout mass flux obtained in the simulation decreases as the mass flux reduction rate increases for CHF 2.01 MW/m^2. However, some of the predicted dryout mass flux values are higher than the experiment mass flux. This is because the slip ratio obtained using the Furukawa and Sekoguchi (1986) model with a correction factor 1.4 appears too low for the experiment with CHF 2.01 MW/m^2. In the steady-state simulation, the CHF_{sim} with correction factor 1.4 is 20-40% lower than the CHF_{exp} in Figure 4.26. Even when the mass flux at time zero is increased by 50% above the experimental CHF value, the liquid film dries out quickly as shown in Figure 4.32.

From energy balance equation, the exit quality at dryout can be calculated. The results are shown in Figure 4.33.

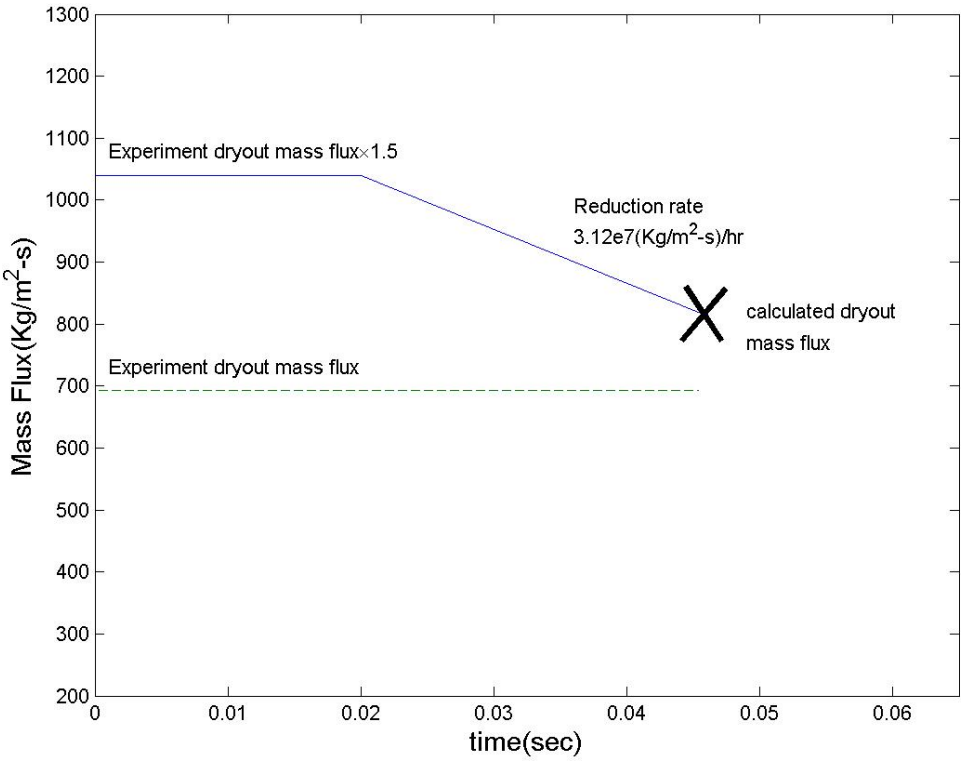

Figure 4.32: Mass flux setting at the mass flux reduction rate 3.12×10^{7} (Kg/m^2-s)/hr (mesh $6\times24\times42$ and $\Delta t=1.0\times10^{-6}$ sec)

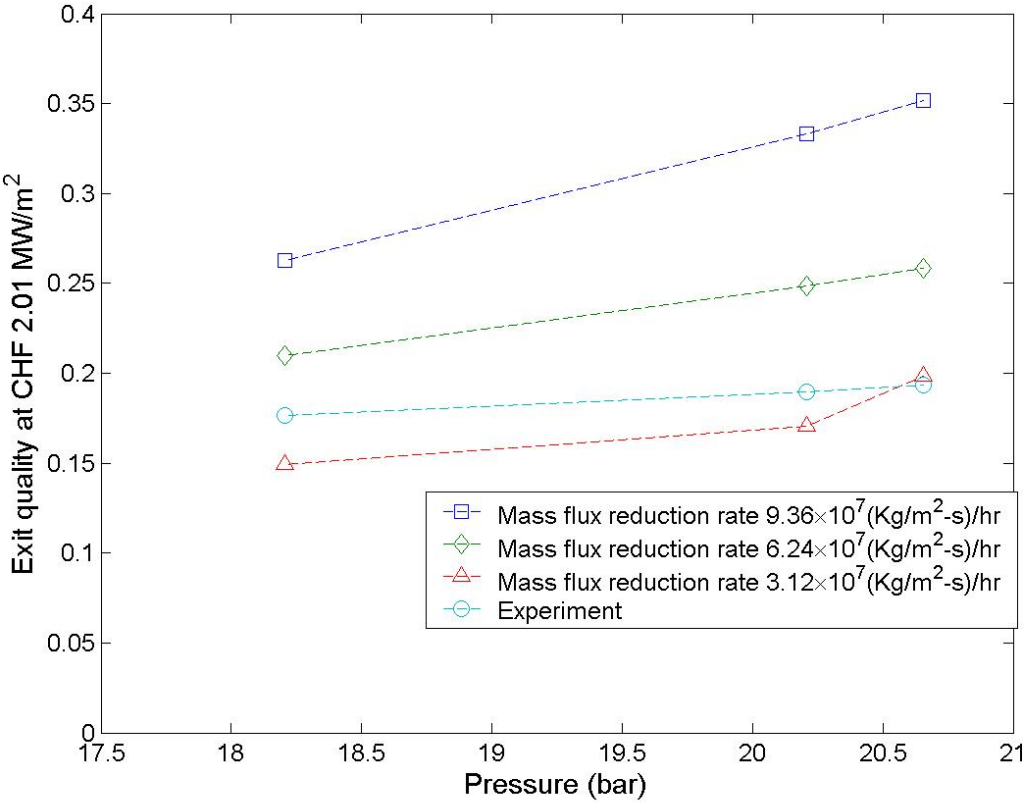

Figure 4.33: Exit quality at CHF 2.01 MW/m^2 for different mass flux reduction rates. (slip ratio=Furukawa and Sekoguchi (1986) correlation$\times$1.4, initial mass flux=1.5 $\times$ experimental value mesh $6\times24\times42$, and $\Delta t=1.0\times10^{-6}$ sec)

4.3.2 Mortimore and Beus (1979) experiment

Mortimore and Beus (1979) measured the critical heat flux at different subcooling conditions for internally heated annuli. In the experiment, the mass flux is kept constant at 352 kg/m^{2}s while slowly increasing the heat flux until the liquid film dries out. The heat flux at dryout is shown in Table 4.4. From the experimental data, we can calculate the initial film thickness using the energy balance equation as we did in the simulation of the Becker and Hernborg (1964) experiment. The heating length of the annulus was 2.13

m. At the test section inlet, the subcooling Δh_i was between 0.1746 MJ/kg and 1.1635 MJ/kg. Pressure was kept at 138 bar. The outer tube diameter was 0.0127 m, while the inner rod diameter was 0.0077 m.

Table 4.4: Critical heat flux data (Mortimore and Beus, 1979)

Inlet subcooling (MJ/Kg)	Critical heat flux (MJ/m^2)
0.1746	0.3849
0.4352	0.5205
0.6840	0.6152
1.1635	0.8518

- Material property

Saturated water and steam at 138 bar (2000 psia) are used as the working fluid; the liquid density, viscosity, conductivity, and specific heat are 624.7 kg/m^3, 7.231×10^{-5} Ns/m^2, 0.4416 W/m^{o}C, and 7715 J/kg^{o}C, respectively; the corresponding values for steam are 85.26 kg/m3, 2.21×10^{-5} Ns/m^2, 0.08156 W/m^{o}C, and 10584 J/kg^{o}C, respectively. The latent heat of vaporization, surface tension coefficient, and saturation temperature are assumed to be constant and equal to 1.079×10^6 J/kg, 0.006547 N/m, and 335.6 ^{o}C.

- Grid convergence study

For the grid convergence test, we predict the CHF for different grid resolutions. As can be seen in Figure 4.16, the predicted CHF value converges as the number of nodes increases. The time step is 1.0×10^{-4} sec. As the number of nodes increases, the predicted

CHF decreases. At the highest resolution (29160 nodes), the predicted CHF is 4.1×10^5 (W/m^2), which is lower than the experimental value of 6.15×10^5 (W/m^2). With the slip ratio calculated from the Furukawa and Sekoguchi (1986) correlation, the prediction tends to underestimate the CHF by 33%. Again, Eq. 4.12 is used to correct the slip ratio.

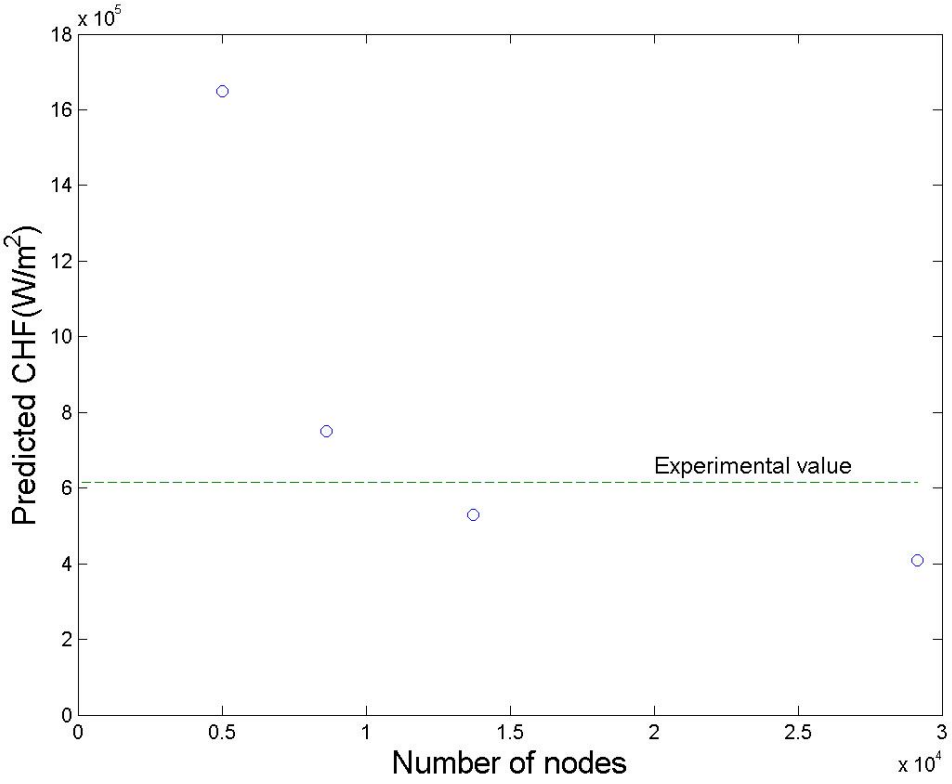

Figure 4.34: Grid convergence study of the simulation for mass flux=352 (kg/m^2-s) in the experiment of Mortimore and Beus (1979) (P=138 (bar), slip ratio=Furukawa and Sekoguchi (1986) correlation, and subcooling Δh_i =0.68 MJ/kg, CIR method, mesh $5\times20\times50$, and $\Delta t=1.0\times10^{-4}$sec)

- Steady State CHF Prediction Results

Steady state CHF values are obtained by performing a series of steady state simulations at different heat flux values for the same film thickness. For low heat flux values dryout does not occur (see square symbols in Fig. 4.35). However, heat fluxes

above a specific value, dryout occurs at the exit (see triangular symbols in Fig. 4.35). The CHF value is obtained by interpolating between the last calculated value with and without dryout. Figures 4.35 to 4.38 illustrate that the predicted steady-state CHF increases as the liquid film thickness increases for different inlet subcooling. Figure 4.39 shows that predicted CHF is very close to the CHF_{exp} when a slip ratio correction factor of 1.3 is used. The simulation error is between -20% and 5%.

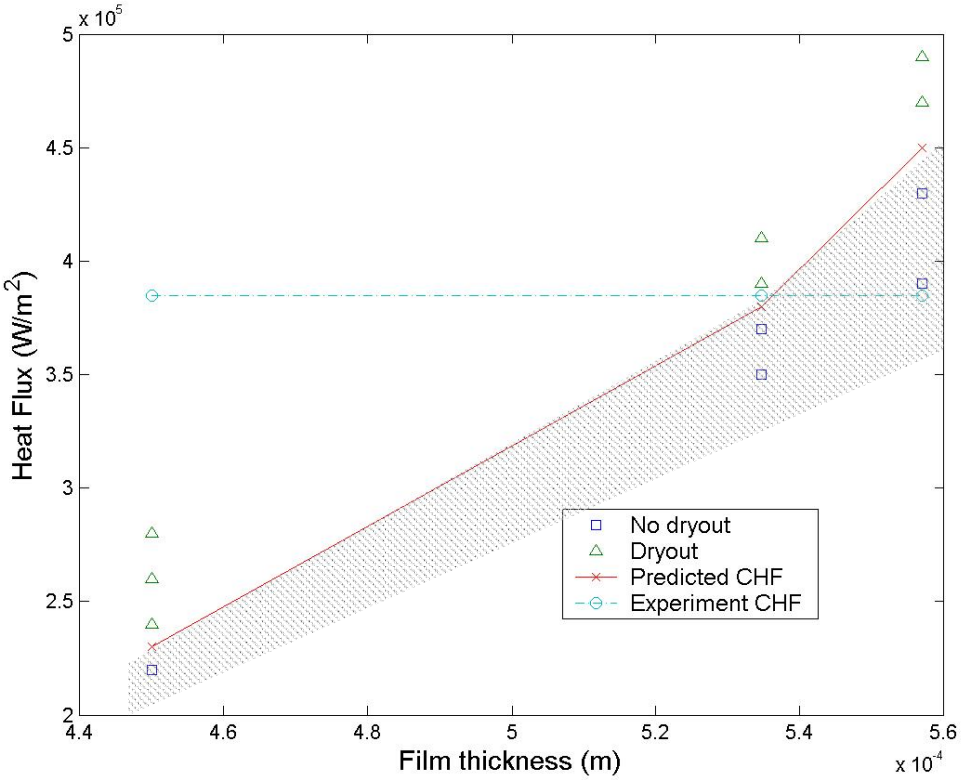

Figure 4.35: Variation of CHF with film thickness at inlet subcooling 0.1746 (MJ/Kg) (P=138 bar, mass flux=352 kg/m^2-s, CIR method, $\Delta t=1.0\times10^{-4}$sec, and mesh $9\times36\times90$)

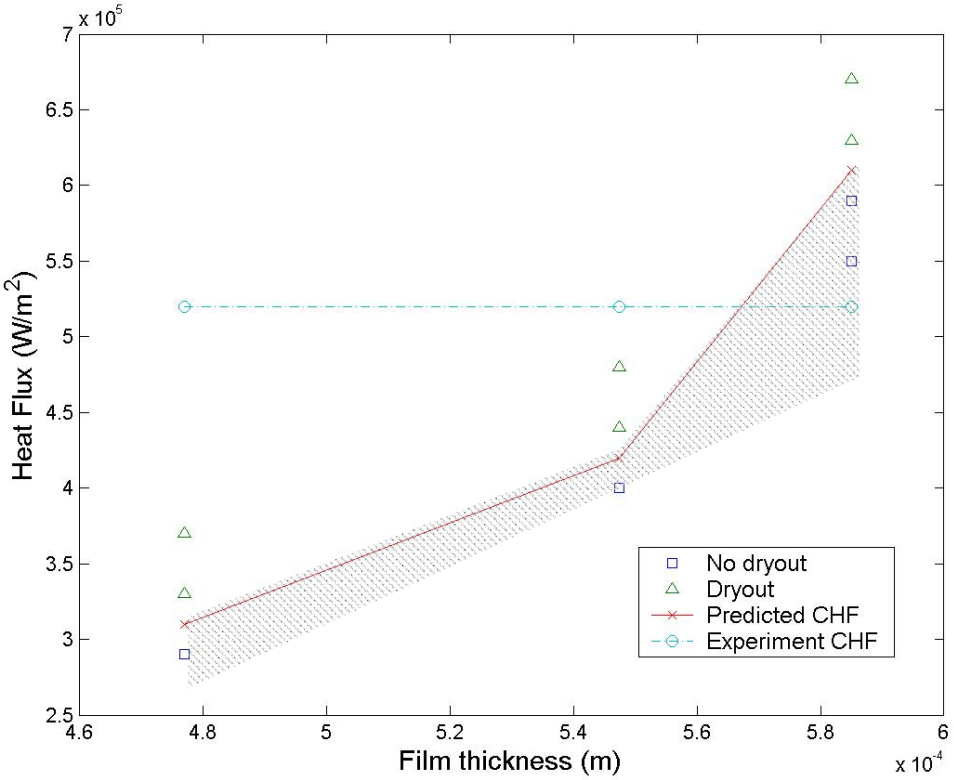

Figure 4.36: Variation of CHF with film thickness at inlet subcooling 0.435 (MJ/Kg) (P=138 bar, mass flux=352 kg/m^2-s, CIR method, $\Delta t=1.0\times10^{-4}$sec, and mesh $9\times36\times90$)

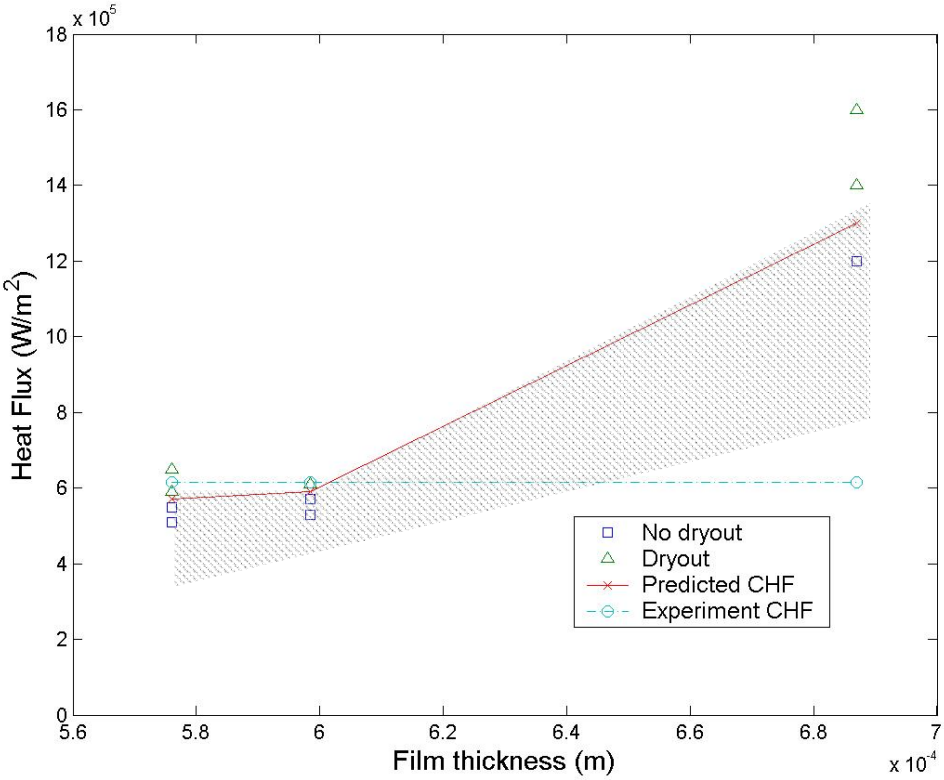

Figure 4.37: Variation of CHF with film thickness at inlet subcooling 0.684 (MJ/Kg) (P=138 bar, mass flux=352 kg/m^2-s, CIR method, $\Delta t=1.0\times10^{-4}$sec, and mesh $9\times36\times90$)

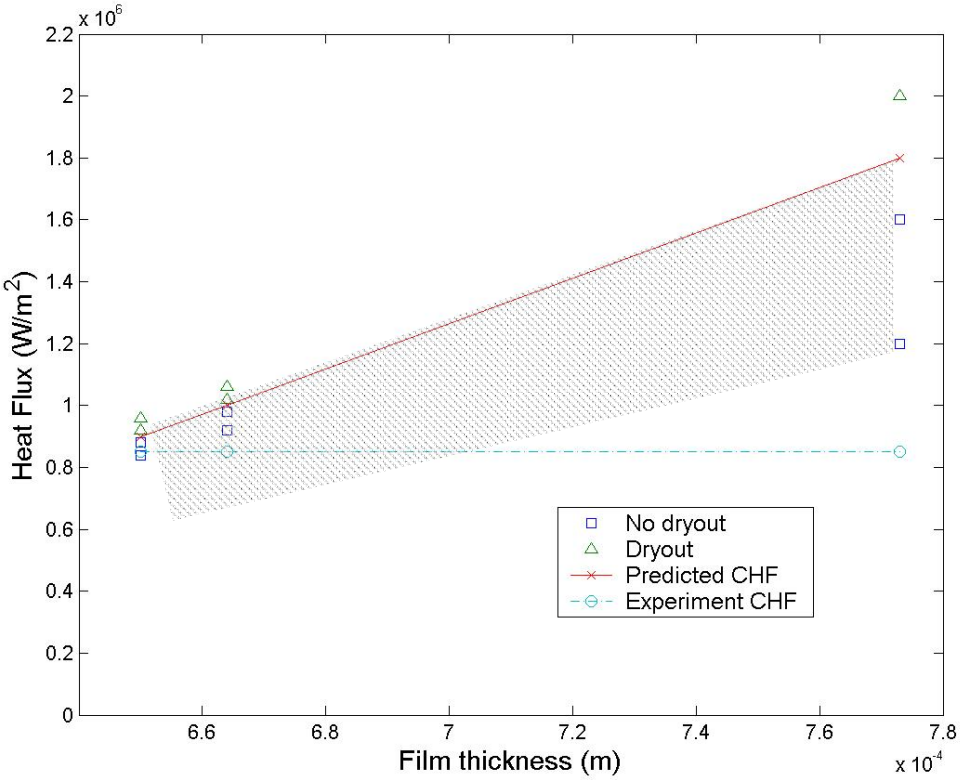

Figure 4.38: Variation of CHF with film thickness at inlet subcooling 1.164 (MJ/Kg) (P=138 bar, mass flux=352 kg/m^2-s, CIR method, $\Delta t=1.0\times10^{-4}$sec, and mesh $9\times36\times90$)

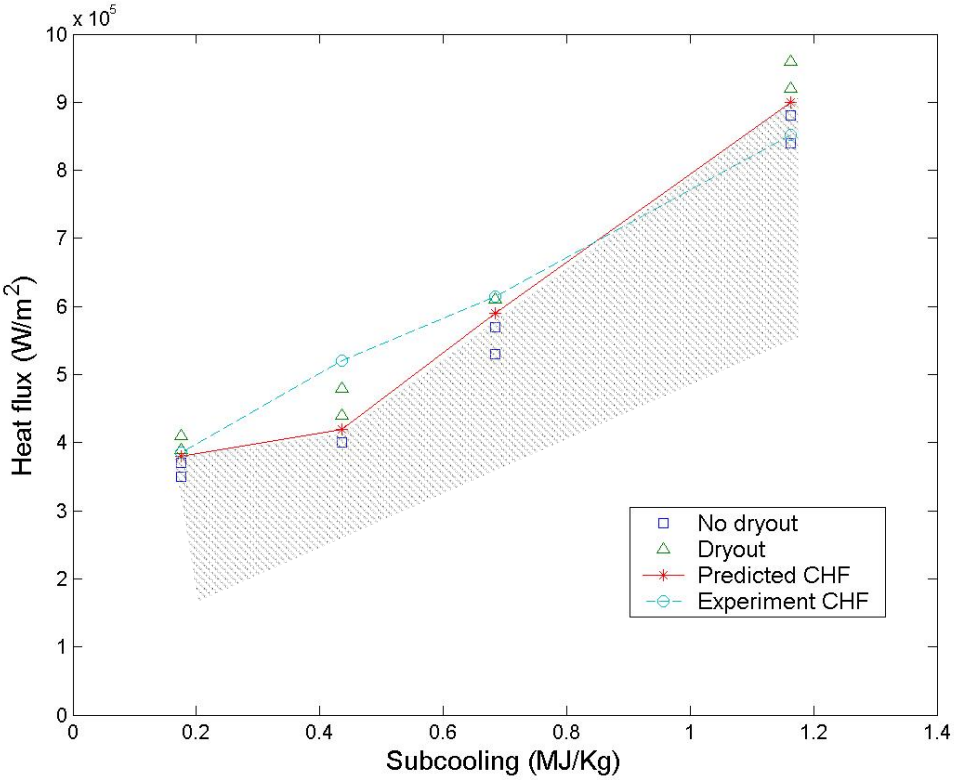

Figure 4.39: Predicted CHF results (P=138 bar, slip ratio=Furukawa and Sekoguchi (1986) correlation$\times$1.3, mass flux=352 kg/m^2-s, CIR method, Δt=1.0$\times$10^{-4}sec, and mesh 9$\times$36$\times$90)

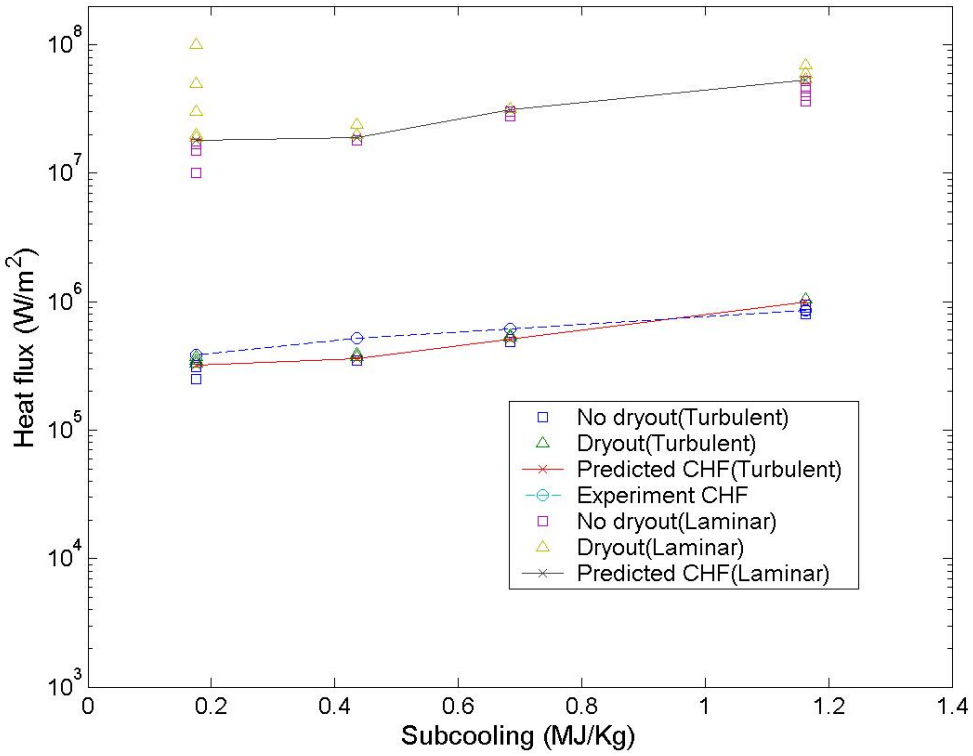

Figure 4.40: Predicted CHF results for laminar and turbulent flows (P=138 bar, slip ratio=Furukawa and Sekoguchi (1986) correlation $\times$ 1.3, mass flux=352 kg/m^2-s, CIR method, Δt=1.0$\times$10^{-4}sec, and mesh 9$\times$36$\times$90)

- CHF Prediction Assuming Laminar Flow

In this section, comparison is made between the predicted CHF values for laminar and turbulent flows with the same liquid thickness and material properties. Both predictions are compared against the experimental data. The Standard $k-\varepsilon$ turbulence model is turned off for the laminar CHF simulations. The simulation results are shown in Figure 4.40. Without including the turbulent model, the CHF prediction is significantly higher than the turbulent model predictions and the experimental data. For the same boundary conditions, the difference between the laminar and turbulent CHF predictions is more than an order of magnitude. Clearly including the turbulence in the dryout model is

critical because the laminar model overestimates the critical heat flux by more than 1000%.

In turbulent flow, there are numerous eddies in the flow ranging in size from "large" eddies to "small" eddies. In addition to the eddies, large scale motion exists in turbulent flow. The complex movement present in turbulent flow greatly enhances the transport of mass, momentum and energy. The heat transfer and evaporation rates in turbulent flow are much higher than the corresponding rates in laminar flow. Thus, the critical heat flux for turbulent flow is much lower than the critical heat flux for laminar flow.

- Transient CHF Prediction for Different Heat-Up Rates

In this section, we focus on CHF prediction for different heat-up rates. Again, the aim is to compare transient CHF predictions against the steady state values. The mechanistic model developed in this investigation allows one to quantify the effects of transient conditions on CHF. In nearly all transient analyses performed for reactor core design, steady state dryout correlations are used to establish safety limits. This approach is used even in BWR stability transients where both reactor power and core flow undergo rapid oscillatory behavior. This practice is usually justified by the assertion that the use of such steady state correlations should yield conservative results. Experimental data supporting such an assertion are not available. Therefore, the model developed in this investigation will be used to examine the validity of such an assertion.

To predict the critical heat flux for transient conditions, experimental data at subcooling 0.68 MJ/kg is used. The corresponding experimental critical heat flux is $6.15 \times 10^5 (W/m^2)$, while the mass flux is 352 (Kg/m^2-s). Assuming a slip ratio of 1.15, an

initial liquid film thickness of 0.000274 m is calculated. In the first two seconds of the simulation, the heat flux is set as half of the experimental critical heat flux. After the liquid film reaches steady state, the heat flux is increased at a prescribed heat-up rate until dryout occurs. The liquid film does not dryout at the initial heat flux.

Figure 4.41 illustrates the heat flux setting at a heat-up rate $6.152\times 10^5(W/m^2)$ sec^{-1}. After the liquid film reaches steady state at two seconds, the heat flux is increased at a heat-up rate of $6.152\times 10^5(W/m^2)$ sec^{-1} until the liquid film dries out. Results similar to that in Figure 4.41 haven been obtained for different heat-up rates following the initial steady state at 50% of the experimental CHF value. The results are shown in Fig. 4.42, which shows the CHF increases as the heat-up rate increases. The predicted critical heat flux values at all heat-up rates are higher than the experimental steady state critical heat flux. The fact that Fig. 4.42 show the predicted values to be higher than the experimental values is related to the uncertainty in the slip ratio, i.e. the initial film thickness. The important point, however, is that the predicted CHF generally increases as the heat-up rate increases. In other words, for faster transients, dryout will occur at a higher heat flux confirming the validity of the assertion that the used of steady state CHF correlation in transient analysis is conservative. Figure 4.43 shows a plot of the dryout time following initiation of the heat-up ramp for the calculation shown in Fig. 4.42. Clearly, the results show that the dryout time decreases as the heat-up rate increases.

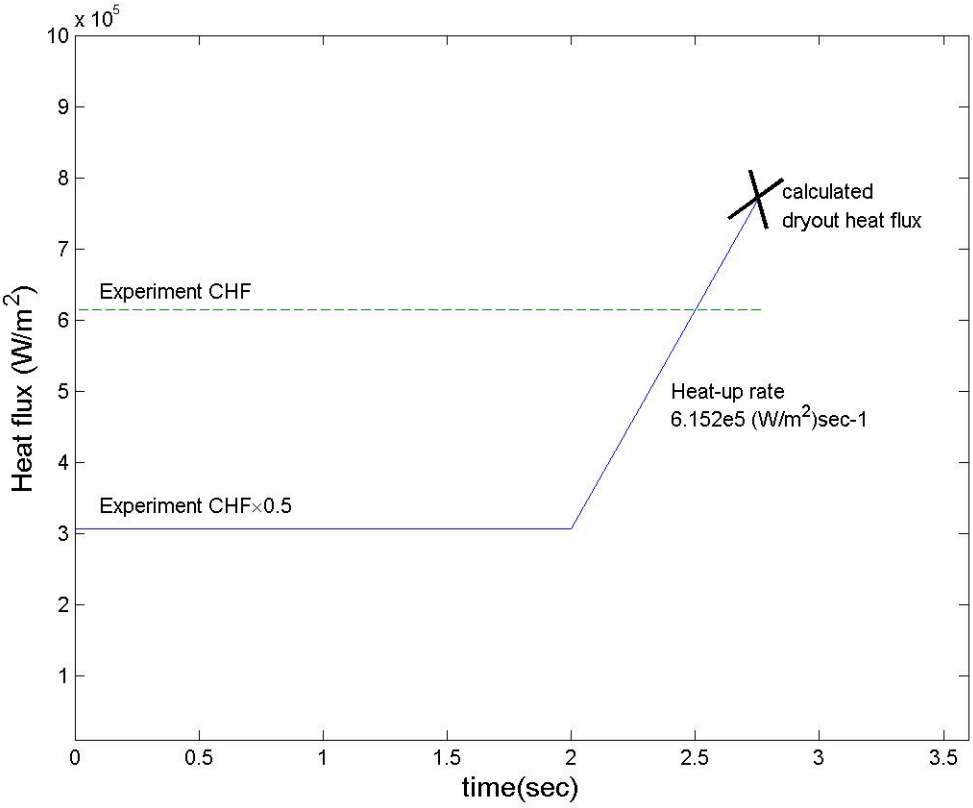

Figure 4.41: Heat flux setting of heat-up rate $6.152\times 10^5(W/m^2)$ sec^{-1}

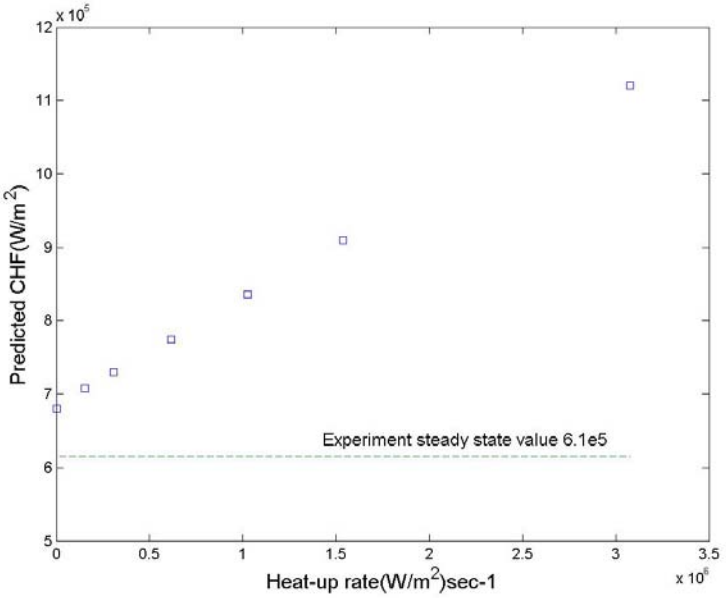

Figure 4.42: CHF prediction results at different heat-up rates (slip ratio 1.15, P=138 bar, mass flux=352 kg/m^2-s, subcooling 0.68 MJ/Kg, CIR method, mesh $5\times20\times50$, and $\Delta t=1.0\times10^{-4}$sec)

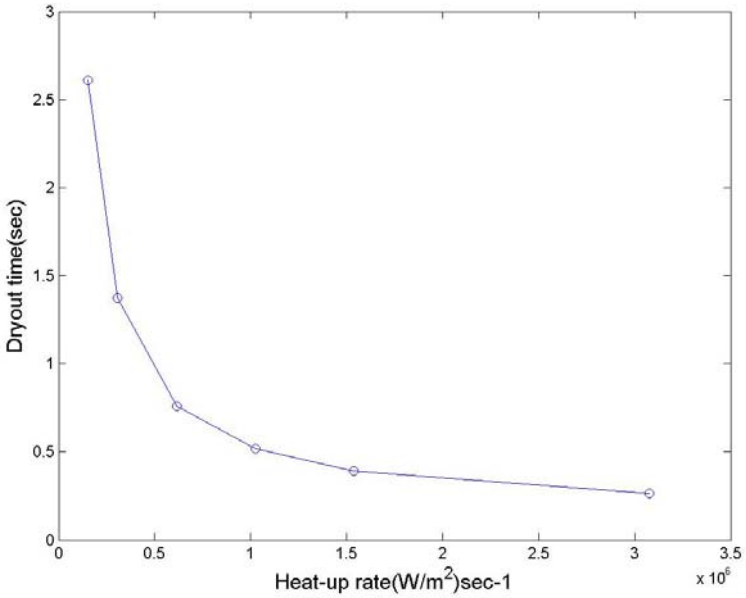

Figure 4.43: Dryout time calculation results at different heat-up rates (slip ratio 1.15, P=138 bar, mass flux=352 kg/m^2-s, subcooling 0.68 MJ/Kg, CIR method, mesh $5\times20\times50$, and $\Delta t=1.0\times10^{-4}$sec)

- Transient CHF Prediction for Different Mass Flux Reduction Rates

In this section, simulations of transient dryout at a fixed heat flux with different mass flux reductions are presented. The critical heat flux at different mass flux reduction rates is also simulated. The setting of the mass flux is similar to the one in Figure 4.27. Assuming a slip ratio of 1.15, the initial liquid film thickness is 0.000274 m. The heat flux is set as the experimental critical heat flux $6.15\times 10^5(\mathrm{W/m^2})$, while the initial mass flux is set as twice the experimental mass flux value. After the liquid film reaches steady state at 2 seconds, the mass flux is reduced at a prescribed rate until the liquid film dries out.

Figure 4.44 shows the predicted CHF values for different mass flux reduction rates. The results show that the dryout mass flux decreases as the mass flux reduction rate increases. In all cases, however, the predicted CHF mass flux values are lower than the corresponding experimental value. Again, this difference is probably related to uncertainty in the slip ratio used to estimate the initial film thickness. However, as discuss in the previous section, the important observation is to note that for a given heat flux, the dryout mass flux decreases as the transient becomes faster. The dryout times corresponding to the results in Fig. 4.44 are shown in Fig. 4.45; the dryout time decreases as the mass flux reduction rate increases. As shown in these two figures, our simulations confirm the assertion that the use of steady state correlations to predict dryout during transient conditions should yield conservative results.

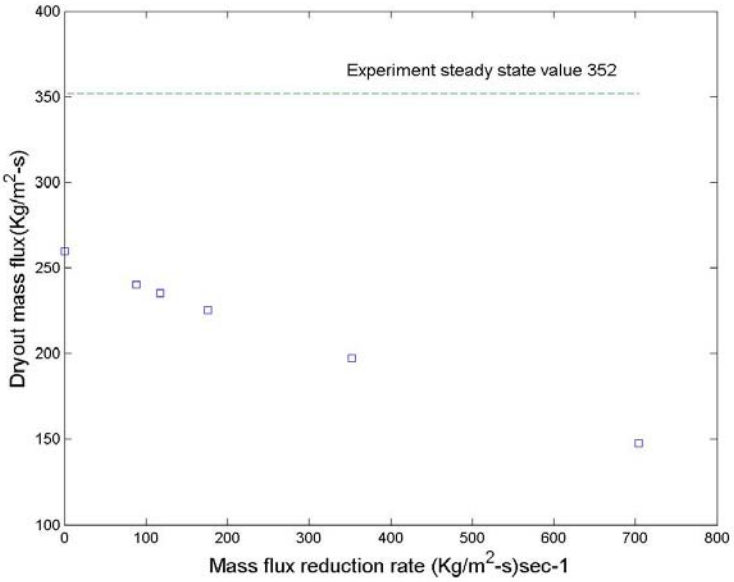

Figure 4.44: Dryout mass flux prediction results at different mass flux reduction rates (slip ratio 1.15, P=138 bar, subcooling 0.68 MJ/Kg, heat flux 6.15×10^{5}W/m^2, CIR method, mesh $5\times20\times50$, and $\Delta t=1.0\times10^{-4}$sec)

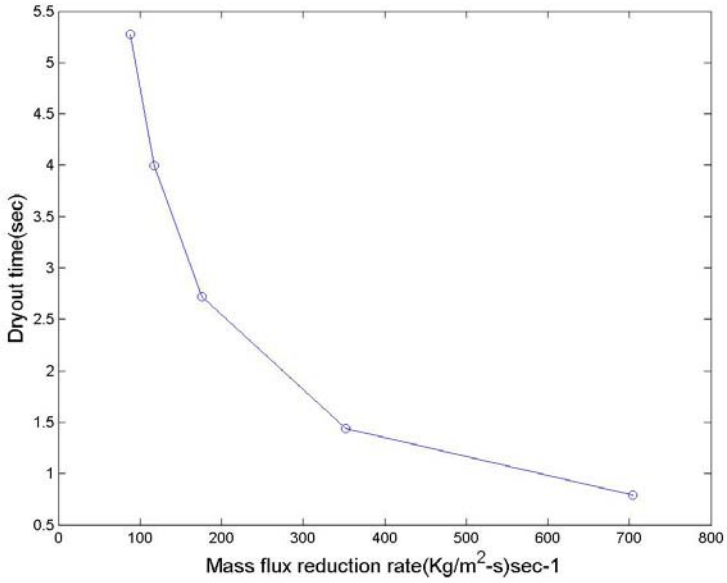

Figure 4.45: Dryout time calculation results at different mass flux reduction rates(slip ratio 1.15, P=138 bar, subcooling 0.68 MJ/Kg, heat flux 6.15×10^{5}W/m^2, CIR method, mesh $5\times20\times50$, and $\Delta t=1.0\times10^{-4}$sec)

4.4 Application to BWRs

In this section, we focus on modeling the behavior of an evaporating thin liquid film on a heated cylindrical rod with spatially non-uniform heating and/or cross flow. As indicated earlier, our interest in this problem derives from earlier work on modeling annular two-phase flow in boiling water reactors (BWRs). It has been hypothesized that some recent fuel failures following control rod maneuvers may have been caused by liquid film instability in regions of localized cross flow and high heat flux gradients. Specifically, the liquid water film flowing upwards along a full-length fuel rod in the upper regions of the core may experience significant azimuthal and axial heat flux gradients and cross flow caused by variations in the thermal-hydraulic conditions in the surrounding subchannels caused by proximity to an inserted control blade tip and/or sudden change in geometry at the top of neighboring part-length rods. The heat flux gradients and cross flows may cause the liquid water film on the fuel rod surface to rupture by hydrodynamic instability, thereby forming a dry hot spot. Such localized dryout phenomena cannot be accurately predicted by current core design methods based on subchannel analysis techniques coupled with empirical dryout correlations. To this end, this effort has been undertaken to develop a mechanistic numerical model by which the detailed three-dimensional behavior of the liquid film along a specific axial node of a specific fuel rod can be mechanistically modeled. The model would supplement current subchannel analysis methods by allowing core designers to focus closely on specific areas of potential concern. It would allow designers to assess the potential for localized fuel failure due to hot spot formation caused by film instability. Such a computational

tool can be used to evaluate various design modifications or operational strategies to prevent occurrence of such un-anticipated dryout conditions.

Various wall heat flux conditions have been applied at the cylindrical solid wall; both uniform and non-uniform heat flux in the axial and azimuthal directions have been used. The heat flux condition at the cylindrical wall is given by:

$$q_w(\theta, z) = q_o(1 + A\cos\theta)\left[1 + B\left(z - \frac{L_z}{2}\right)\right]. \qquad (4.14)$$

where q_o is the reference heat flux, while A and B are the fractional perturbation magnitudes of heat flux in the axial and azimuthal directions.

Saturated water and steam at 6.9 MPa (1000 psia) are used as the working fluids; the liquid density, viscosity, conductivity, and specific heat are 741.7 kg/m^3, 9.17×10^{-5} kg/ms, 0.5613 W/m^{o}C, and 4973 J/kg^{o}C, respectively; the corresponding values for steam are 35.95 kg/m^3, 1.89×10^{-5} kg/ms, 0.0573 W/m^{o}C, and 2684 J/kg^{o}C, respectively. The latent heat of vaporization, surface tension coefficient, and saturation temperature are assumed to be constant and equal to 1.512×10^6 J/kg, 0.01785 N/m, and 558.8 K, respectively.

The inner rod diameter is assumed to be 1.0×10^{-2}m and the outer "wall" diameter is assumed to be 1.693×10^{-2}m. The outer diameter has been selected to produce a channel hydraulic diameter comparable to that for typical BWR bundles. The liquid film is assumed to have a uniform initial thickness around the rod. In all cases, the initial film thickness is assumed to be 1.0×10^{-3} m, while the axial velocity of the "outer wall" is assumed to be 10 m/sec. The BFECC method is used with mesh $5\times20\times50$.

Figure 4.46 shows the calculated minimum liquid film thickness for different non-uniform heating profiles. In some cases, the liquid film may momentarily dries out before recovering and reaching a steady state value as is the case for non-uniform heating with variation amplitude of 20% and 30% of the normal heat flux. For non-uniform heating with variation amplitude of 50%, the liquid film dries out at time 0.32 sec and does not recover. Figure 4.47 shows the detail liquid film evolvement. As can be seen in Figure 4.47, a dry patch is formed at the top of the rod at 0.4, 0.48, and 0.56 sec for the non-uniform heating with variation amplitude of 50%. Figure 4.48 shows the minimum liquid film thickness when cross flow is imposed on the primary axial flow. At cross flow 0.1% (velocity 0.01 m/s), the liquid film does not dry out. At cross flow 1% (velocity 0.1 m/s) and 2% (velocity 0.2 m/s), the liquid film dries out quickly. Figure 4.49 shows that a dry patch is formed on the rod with cross flow 2%. The results shown in Figure 4.46 through 4.49 show that both localized non-uniform heating and cross flow can lead to film instability and "premature" dryout in BWRs.

The results presented here clearly indicate that localized heat flux gradients and cross flow can lead to film breakdown and dry spot formation. Such mechanism may have contribute to the recently observed BWR fuel failures following control rod maneuvers while the control blade tip was located near the top of part-length rods. The method developed in this investigation offers the means to assess the potential for such effects in Boiling Water Reactors.

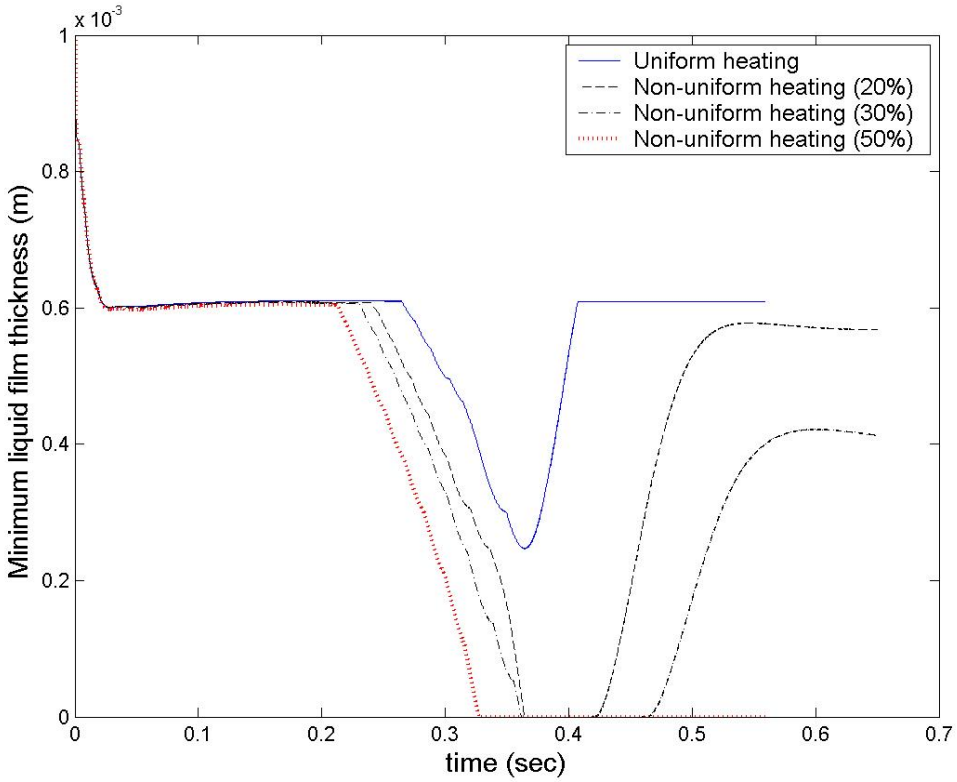

Figure 4.46: Variation of the calculated minimum film thickness with time for different non-uniform heating conditions (BFECC method, mesh $5\times20\times50$, and $\Delta t=1.0\times10^{-5}$sec, q_w of 1.6×10^5 W/m^2, the axial "outer" wall velocity is 10.0 m/s)

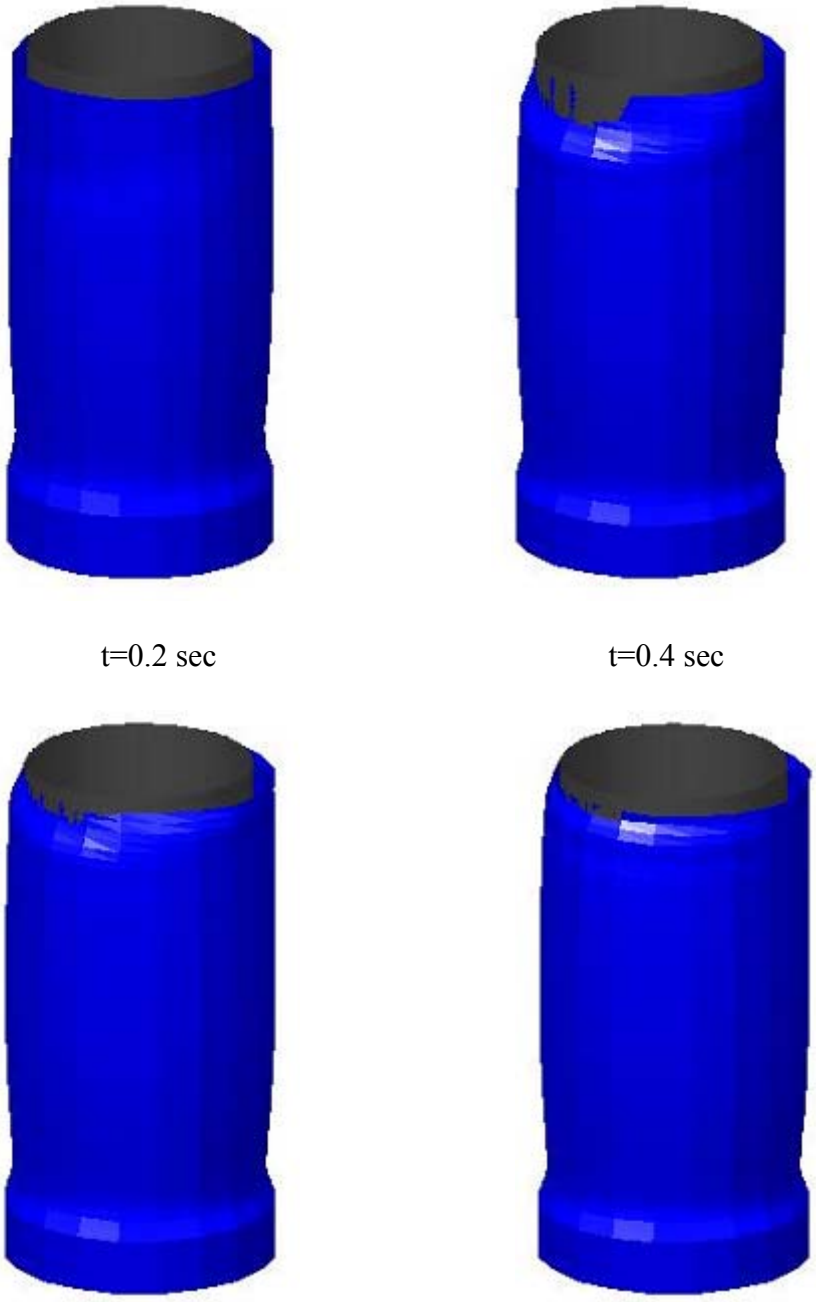

Figure 4.47: Detailed interfacial structure for non-uniform 50% for turbulent flow (Note: This figure is not to scale; the z-dimension has been compressed by a factor of 5 for easier viewing. BFECC method, $\Delta t=1.0\times10^{-5}$sec, mesh $5\times20\times50$, and, q_w of 1.6×10^5 W/m^2, the axial "outer" wall velocity is 10.0 m/s)

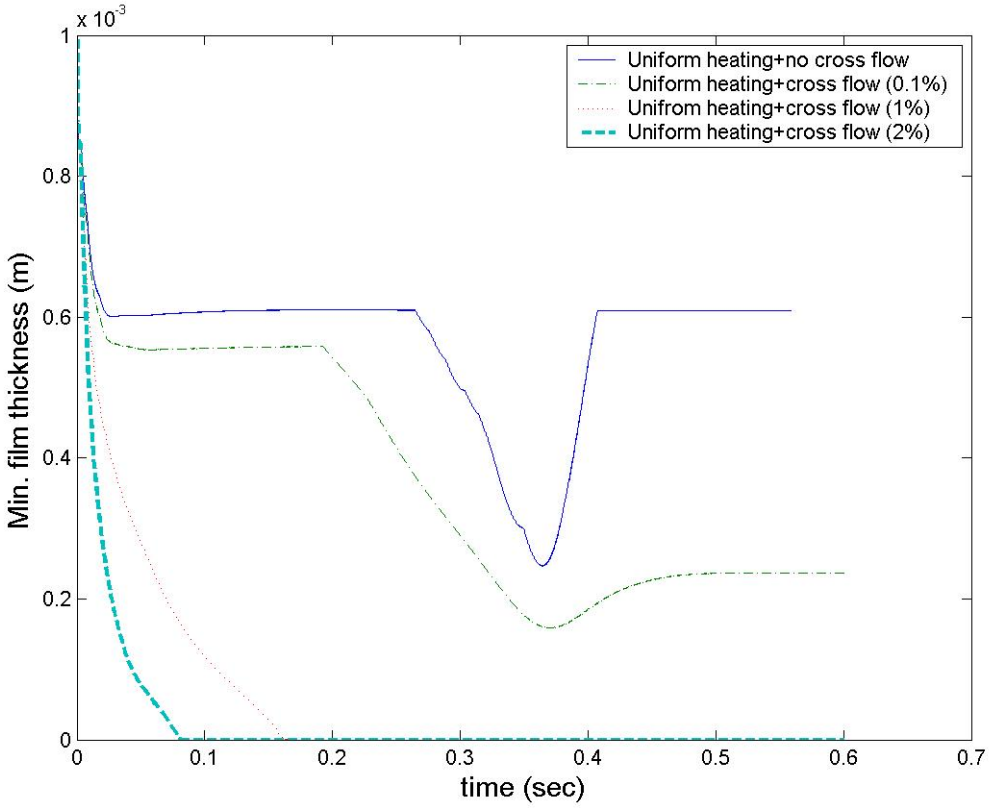

Figure 4.48: Variation of the calculated minimum film thickness with time for different cross flow conditions (BFECC method, $\Delta t=1.0\times10^{-5}$sec, mesh $5\times20\times50$, and, q_w of 1.6×10^5 W/m^2, the axial "outer" wall velocity is 10.0 m/s)

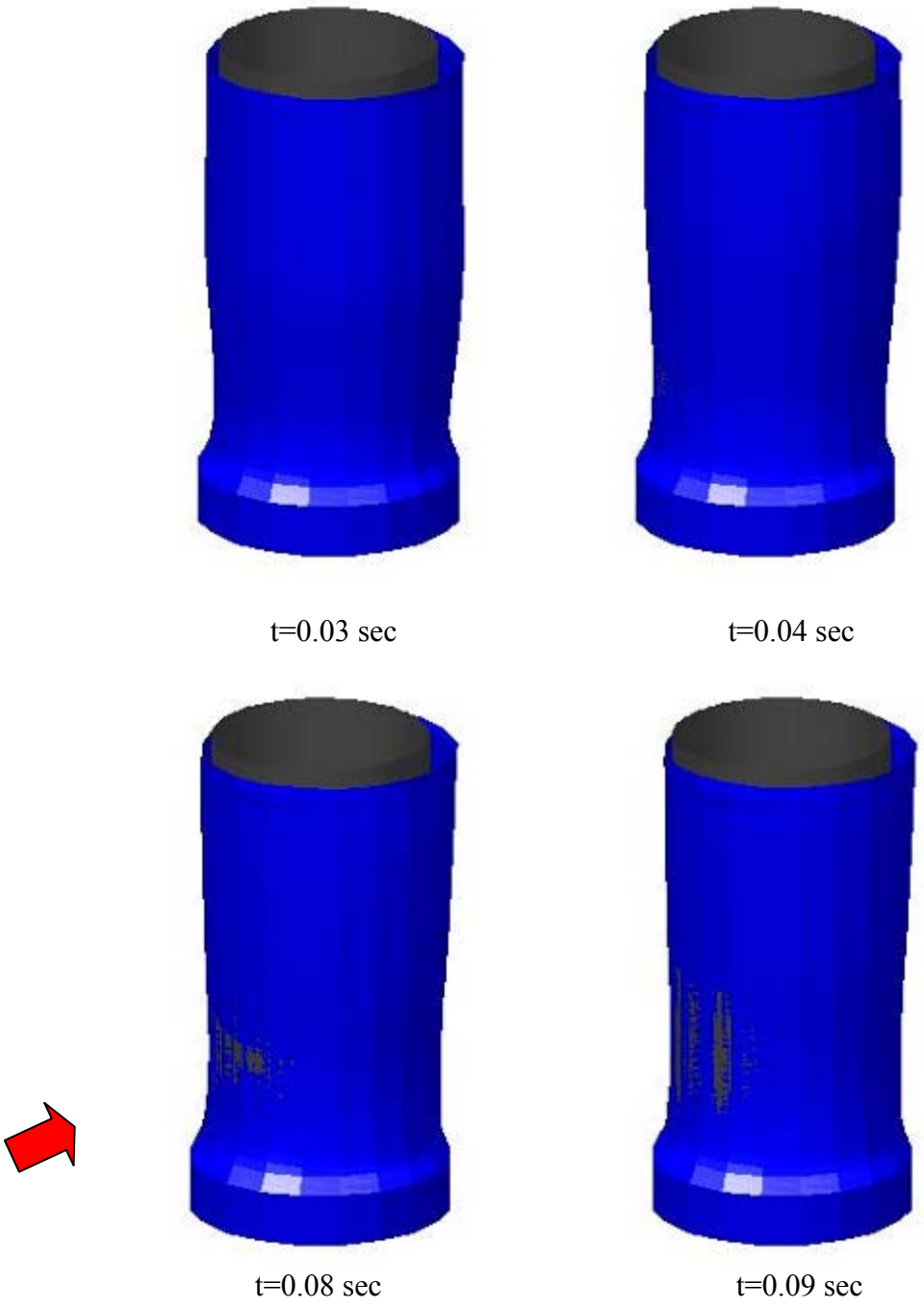

Figure 4.49: Detailed interfacial structure for cross flow 2% (Note: This figure is not to scale; the z-dimension has been compressed by a factor of 5 for easier viewing. BFECC method, $\Delta t=1.0\times10^{-5}$sec, mesh $5\times20\times50$, and, q_w of 1.6×10^{5} W/m^2, the axial "outer" wall velocity is 10.0 m/s)

CHAPTER 5

CONCLUSIONS AND RECOMMENDATIONS

This work has been aimed at developing a mechanistic, transient, 3-D numerical model to predict the behavior of an evaporating thin liquid film on a nonuniformly heated cylindrical rod with simultaneous parallel and cross flow of vapor. To this end, a numerical model based on the Level Contour Reconstruction Method was developed. The Standard k-ε turbulence model is included. A cylindrical coordinate system has been used to enhance the resolution of the Level Contour Reconstruction Model. Comparison has been made between the model predictions and experimental data. A model of this type is necessary to supplement current state-of-the-art BWR core thermal-hydraulic design methods based on subchannel analysis techniques coupled with empirical dry out correlations. In essence, such a model would provide the core designer with a "magnifying glass" by which the behavior of the liquid film at specific locations within the core (specific axial node on a specific locations within a specific bundle in the subchannel analysis model) can be closely examined. The boundary conditions for such a detailed model would be provided by the more global subchannel analysis results. A tool of this type would allow the designer to examine the effectiveness of possible design changes and/or modified control strategies to prevent conditions leading to localized film instability and possible fuel failure.

The main work in this thesis involves expansion of the method originally proposed by Shin and Abdel-Khalik (2007) to include turbulence effects and use of

cylindrical coordinates for the fixed Eulerian grid. These modifications are necessary for proper modeling of the problem of interest, namely prediction of dryout in a BWR fuel rod with axial and azimuthal heat flux gradients and cross flow from neighboring subchannels. In a BWR reactor core, the Reynolds number of the flow is nearly 10^6; hence, the flow is highly turbulent. There are numerous eddies in the flow ranging in size from "large" eddies to "small" eddies in the flow. In addition to eddies, large scale motion exists in turbulent flow. To model the physics of the flow and dryout on a fuel rod, it is critical to account for turbulent effects on the various transport processes. Without accounting for turbulence and the corresponding enhancement in film vaporation, our simulation shows that the calculated dryout heat flux will likely be considerably higher than the actual value, i.e. non-conservative. The complex movement present in turbulent flow greatly enhances the transport of mass, momentum and energy, well above the rates achieved in laminar flow. Heat transfer and evaporation rate in turbulent flow are much higher than the rate in laminar flow. Thus the critical heat flux for turbulent flow is much lower than the value to be predicted for the same conditions without accounting for turbulence.

In addition to simulating turbulence effects, we have solved the governing equations using a cylindrical coordinate system rather than the Cartesian coordinate system used in the original LCRM (Shin and Juric, 2002). Using a Cartesian coordinate system to simulate a cylindrical BWR fuel rod requires use of an immersed boundary method to approximate the boundary condition on the rod surface. While numerical schemes such as the immersed boundary method have gained some success in the past, the use of cylindrical coordinates for the problem at hand makes it considerably easier to

specify the boundary conditions without any approximation. This is particularly important to our simulation since the liquid film on the rod is expected to be very thin and its movement is very sensitive to the boundary condition on the surface. Using a cylindrical coordinate system eliminates any unnecessary approximations.

Experimental data sets obtained by Becker and Hernborg (1964) and Mortimore and Beus (1979) has been used to compare with the model predictions of critical heat flux. The Level Contour Reconstruction Method is applied to the last 10 cm of the test section. With a vapor slip empirical correction factor of 1.4, the CHF prediction error ranges from 3 to 40%. Use of the BFECC method improves the CHF prediction by 11-20%.

The mechanistic model developed in this investigation allows one to quantify the effects of transient conditions on CHF. In nearly all transient analyses performed for reactor core design, steady state dry out correlations are used to establish safety limits. This approach is used even in BWR stability transients where both reactor power and core flow undergo rapid oscillatory behavior. This practice is usually justified by the assertion that the use of such steady state correlations should yield conservative results. Experimental data supporting such an assertion are not available. Our simulations confirmed the validity of this assertion, namely, the use of steady state correlations to predict dryout under transient conditions is indeed conservative. Additionally, the extent of conservation increases as the rate of change of either the heat flux or mass flux increases.

5.1 Contributions

The work presented in this thesis is the first in the open literature to predict the critical heat flux for internally heated annuli using the Level Contour Reconstruction Method; the model has been expanded to include turbulent effects and use cylindrical coordinates for the fixed Eulerian grid. The main contributions of this doctoral thesis are

1. Expansion of the Level Contour Reconstruction Method to include turbulence effects using the Standard $k-\varepsilon$ model since the flow in a BWR core is highly turbulent.
2. Use of the cylindrical coordinate system for the fixed Eulerian grid rather than the Cartesian coordinate system in the original LCRM. The boundary condition the rod surface can be set naturally and easily.
3. Validation of the Level Contour Reconstruction Method in the prediction of the critical heat flux for internally heated annuli.
4. Validation of the conservative nature of the practice of using steady state CHF correlations to establish safety limits under transient conditions.

5.2 Recommendations

Based on the results of this investigation, additional work is needed to enhance the accuracy of the model.

1. To determine the initial liquid film thickness in the LCRM model, a validated correlation of void fraction for water and steam in annuli is necessary. While these correlations are not available in the open literature, proprietary correlations have been developed and validated by reactor

vendors. Using the validated correlations with the permission from the vendors would significantly improve our ability to establish the initial conditions for various operating parameters.

2. Our code has not been optimized for computational efficiency and we believe there is much room for improvement regarding simulation speed. However, ultimately we would need to parallelize the code in order to achieve the higher resolution simulations necessary to resolve the detailed features of turbulent flows.
3. To simulate a square subchannel in a BWR core using a cylindrical coordinate system, advanced numerical technique must be employed to model the "square wall".
4. Future efforts will also include development of methods aimed at enhancing the interface model by incorporating such effects as disjoining pressure, non-equilibrium distribution of phase interface temperature, and contact line dynamics to provide a more complete analysis and to capture film behavior after rupture.
5. The use of other turbulence models, particularly for the liquid film region, should be explored.

APPENDIX A

FINITE DIFFERENCE DISCRETIZATION OF THE SHEAR STRESS TERMS IN THE RANS EQUATION

The common central difference scheme to discretize the shear tress terms in the RANS equations is employed. This central difference scheme is introduced by the following examples on the 2D r-θ plane. Then the finite difference scheme on the 3D r-θ-z plane is presented.

Example A.1: Finite difference discretization $\left.\frac{1}{r}\frac{\partial}{\partial r}(r\cdot\tau_{rr})\right|_A = \left.\frac{1}{r}\frac{\partial}{\partial r}(r\cdot\mu\cdot 2\frac{\partial u}{\partial r})\right|_A$

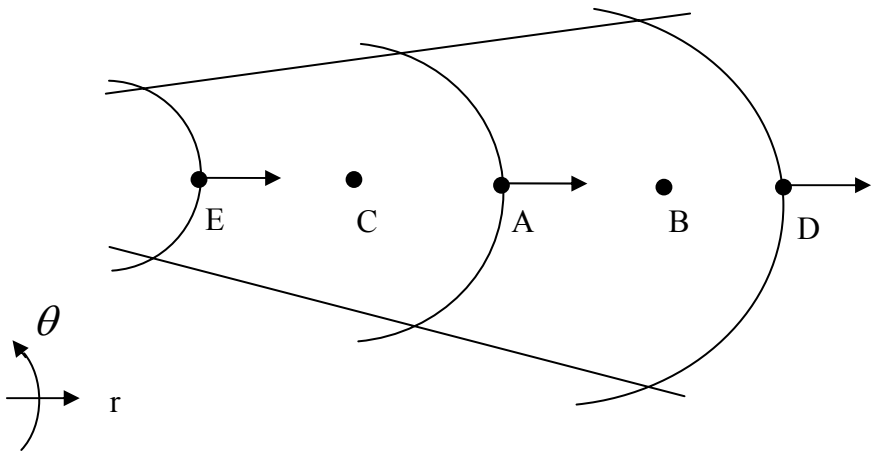

Figure A.1: Finite difference scheme of Example A.1

$$\left.\frac{1}{r}\frac{\partial}{\partial r}(r\cdot\mu\cdot 2\frac{\partial u}{\partial r})\right|_A \approx$$

$$\frac{1}{r(A)}\frac{1}{\Delta r}\left\{r(B)\cdot\mu(B)\cdot 2\cdot\frac{u(D)-u(A)}{\Delta r}\right.$$

$$\left.-\,r(C)\cdot\mu(C)\cdot 2\frac{u(A)-uE)}{\Delta r}\right\} \qquad \text{(A.1)}$$

Example A.2

Finite difference discretization

$$\frac{1}{r^2}\frac{\partial}{\partial r}\left\{r^2\tau_{r\theta}\right\}\Big|_A = \frac{1}{r^2}\frac{\partial}{\partial r}\left\{r^2\mu\left[r\frac{\partial}{\partial r}\left(\frac{v}{r}\right)+\frac{1}{r}\frac{\partial u}{\partial \theta}\right]\right\}\Big|_A$$

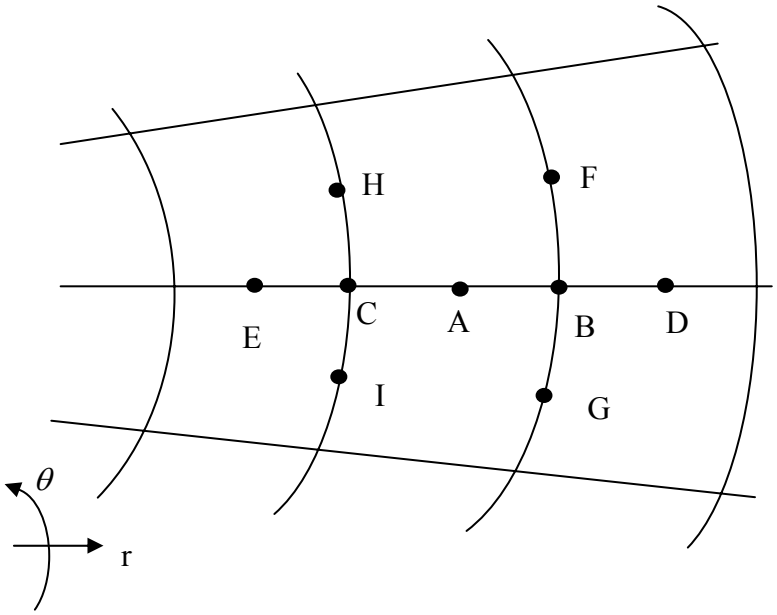

Figure A.2: Finite difference discretization of Example A.2

$$\frac{1}{r^2}\frac{\partial}{\partial r}\left\{r^2\mu\left[r\frac{\partial}{\partial r}\left(\frac{v}{r}\right)+\frac{1}{r}\frac{\partial u}{\partial \theta}\right]\right\}\Bigg|_A$$

$$\approx \frac{1}{r(A)^2}\frac{1}{\Delta r}\left\{r^2\mu\left[r\frac{\partial}{\partial r}\left(\frac{v}{r}\right)+\frac{1}{r}\frac{\partial u}{\partial \theta}\right]\Bigg|_B - r^2\mu\left[r\frac{\partial}{\partial r}\left(\frac{v}{r}\right)+\frac{1}{r}\frac{\partial u}{\partial \theta}\right]\Bigg|_C\right\}$$

$$\approx \frac{1}{r(A)^2}\frac{1}{\Delta r}\left\{\begin{array}{l} r^2(B)\mu(B)\left[r(B)\dfrac{1}{\Delta r}\left(\dfrac{v(D)}{r(D)}-\dfrac{v(A)}{r(A)}\right)+\dfrac{1}{r(B)}\dfrac{1}{\Delta\theta}\left(u(F)-u(G)\right)\right] \\ -r^2(C)\mu(C)\left[r(C)\dfrac{1}{\Delta r}\left(\dfrac{v(A)}{r(A)}-\dfrac{v(E)}{r(E)}\right)+\dfrac{1}{r(C)}\dfrac{1}{\Delta\theta}\left(u(H)-u(I)\right)\right] \end{array}\right\} . \quad \text{(A.2)}$$

In the following, on the 3D r-θ-z plane, the finite difference discretization of the shear stress terms in the RANS equation is presented. The definitions of the symbol we used in the program are the following:

hr: Δr

hs: $\Delta\theta$

hz: Δz

rs(i): radius r at the location of scalar quantities

r(i): radius r at the location of vector u

vs: molecular viscosity

ve: eddy viscosity

**: square

one : number 1

two: number 2

three: number 3

four : number 4

$$\tau_{rr} = (\mu_L + \mu_T)\left[2\frac{\partial u}{\partial r}\right]$$

$$\tau_{\theta\theta} = (\mu_L + \mu_T)\left[2\left(\frac{1}{r}\frac{\partial v}{\partial \theta} + \frac{u}{r}\right)\right]$$

$$\tau_{zz} = (\mu_L + \mu_T)\left[2\frac{\partial w}{\partial z}\right]$$

$$\tau_{r\theta} = \tau_{\theta r} = (\mu_L + \mu_T)\left[r\frac{\partial}{\partial r}(\frac{v}{r}) + \frac{1}{r}\frac{\partial u}{\partial \theta}\right] \qquad \text{(A.3)}$$

$$\tau_{\theta z} = \tau_{z\theta} = (\mu_L + \mu_T)\left[\frac{\partial v}{\partial z} + \frac{1}{r}\frac{\partial w}{\partial \theta}\right]$$

$$\tau_{zr} = \tau_{rz} = (\mu_L + \mu_T)\left[\frac{\partial w}{\partial r} + \frac{\partial u}{\partial z}\right]$$

$$\frac{1}{r}\frac{\partial}{\partial r}(r\tau_{rr}) \approx \text{ one/r(i)/hr**two*(rs(i+1)*(vs(i+1,j,k)+ve(i+1,j,k))}$$

$$\text{*two*(u(i+1,j,k)- u(i ,j,k))-rs(i)} \qquad \text{(A.4)}$$

$$\text{*(vs(i,j,k)+ve(i,j,k))*two*(u(i ,j,k)- u(i-1,j,k)))}$$

$$\frac{1}{r}\frac{\partial}{\partial \theta}\tau_{\theta r} \approx \text{ one/r(i)/hs*((vs(i,j,k)+vs(i+1,j,k)+vs(i,j+1,k)+vs(i+1,j+1,k)}$$

$$\text{+ve(i,j,k)+ve(i+1,j,k)+ve(i,j+1,k)+ve(i+1,j+1,k))/four}$$

$$\text{*(r(i)/hr*(v(i+1,j, k)/rs(i+1)-v(i,j, k)/rs(i))}$$

$$\text{+one/r(i)*(u(i ,j+1,k)-u(i,j,k))/hs)-(vs(i,j,k)+vs(i+1,j,k)} \qquad \text{(A.5)}$$

$$\text{+vs(i,j-1,k)+vs(i+1,j-1,k) +ve(i,j,k)+ve(i+1,j,k)}$$

$$\text{+ve(i,j-1,k)+ve(i+1,j-1,k))/four *(r(i)/hr*(}$$

$$\text{v(i+1,j-1,k)/rs(i+1)-v(i, j-1,k)/rs(i))+one/r(i)*(u(i,j,k)-u(i,j-1,k))/hs))}$$

$$\frac{\partial}{\partial z}\tau_{zr} \approx \text{one/hz*((vs(i,j,k)+vs(i+1,j,k)+vs(i,j,k+1)+vs(i+1,j,k+1)}$$

+ve(i,j,k)+ve(i+1,j,k)+ve(i,j,k+1)+ve(i+1,j,k+1))/four*((w(i+1,j,k)-

w(i,j,k))/hr+(u(i,j,k+1)-u(i,j,k))/hz)-(vs(i,j,k)+vs(i+1,j,k) (A.6)

+vs(i,j,k-1)+vs(i+1,j,k-1) +ve(i,j,k)+ve(i+1,j,k)+ve(i,j,k-1)

+ve(i+1,j,k-1))/four*((w(i+1,j,k-1)-w(i,j,k-1))/hr +(u(i,j,k)-u(i,j,k-1))/hz))

$$\frac{\tau_{\theta\theta}}{r} \approx$$ (vs(i,j,k)+vs(i+1,j,k)+ve(i,j,k)+ve(i+1,j,k))/two/r(i) (A.7)

two(one/two/r(i)/hs*(v(i,j,k)+v(i+1,j,k)-v(i,j-1,k)-v(i+1,j-1,k)) +u(i,j,k)/r(i))

$$\frac{1}{r^2}\frac{\partial}{\partial r}(r^2\tau_{r\theta}) \approx$$ one/rs(i)**two/hr*(r(i)**two*

(vs(i,j,k)+vs(i+1,j,k)+vs(i,j+1,k)

+vs(i+1,j+1,k) +ve(i,j,k)+ve(i+1,j,k)+ve(i,j+1,k)+ve(i+1,j+1,k))/four

(r(i)/hr(v(i+1,j,k)/rs(i+1)-v(i,j,k)/rs(i))+one/r(i)/hs

*(u(i,j+1,k)-u(i,j,k))) (A.8)

-r(i-1)**two*(vs(i-1,j+1,k)+vs(i,j+1,k)+vs(i-1,j,k)+vs(i,j,k)

+ve(i-1,j+1,k)+ve(i,j+1,k)+ve(i-1,j,k)+ve(i,j,k))/four*(r(i-1)/hr*(v(i,j,k)/rs(i)

-v(i-1,j,k)/rs(i-1)) +one/r(i-1)/hs*(u(i-1,j+1,k)-u(i-1,j,k))))

$$\frac{1}{r}\frac{\partial}{\partial\theta}\tau_{\theta\theta} \approx$$ one/rs(i)/hs*(two*(vs(i,j+1,k)+ve(i,j+1,k))*(one/rs(i)/hs*

(v(i,j+1,k)-v(i,j,k))+(u(i,j+1,k)+u(i-1,j+1,k))/two/rs(i)) –two (A.9)

(vs(i,j,k)+ve(i,j,k))(one/rs(i)/hs*(v(i,j,k)-v(i,j-1,k))

+(u(i,j,k)+u(i-1,j,k))/two/rs(i)))

$$\frac{\partial}{\partial z}\tau_{z\theta} \approx \text{one/hz*((vs(i,j,k)+vs(i,j+1,k)+vs(i,j,k+1)+vs(i,j+1,k+1)}$$

$$\text{+ve(i,j,k)+ve(i,j+1,k)+ve(i,j,k+1)+ve(i,j+1,k+1))/four}$$

$$\text{*((v(i,j,k+1)-v(i,j,k))/hz +one/rs(i)/hs*(w(i,j+1,k)-w(i,j,k)))-} \qquad \text{(A.10)}$$

$$\text{(vs(i,j,k)+vs(i,j+1,k)+vs(i,j,k-1)+vs(i,j+1,k-1) +ve(i,j,k)}$$

$$\text{+ve(i,j+1,k)+ve(i,j,k-1)+ve(i,j+1,k-1))/four *((v(i,j,k)-v(i,j,k-1))/hz}$$

$$\text{+one/rs(i)/hs*(w(i,j+1,k-1)-w(i,j,k-1))))}$$

$$\frac{1}{r}\frac{\partial}{\partial r}(r\tau_{rz}) \approx \text{one/rs(i)/hr*(r(i)*(vs(i,j,k)+vs(i+1,j,k)}$$

$$\text{+vs(i,j,k+1)+vs(i+1,j,k+1) +ve(i,j,k)+ve(i+1,j,k)}$$

$$\text{+ve(i,j,k+1)+ve(i+1,j,k+1))/four} \qquad \text{(A.11)}$$

$$\text{*((w(i+1,j,k)-w(i,j,k))/hr+(u(i,j,k+1)-u(i,j,k))/hz)}$$

$$\text{-r(i-1)*(vs(i,j,k)+vs(i-1,j,k)+vs(i,j,k+1)+vs(i-1,j,k+1)}$$

$$\text{+ve(i,j,k)+ve(i-1,j,k)+ve(i,j,k+1)+ve(i-1,j,k+1))/four}$$

$$\text{*((w(i,j,k)-w(i-1,j,k))/hr}$$

$$\text{+(u(i-1,j,k+1)-u(i-1,j,k))/hz))}$$

$$\frac{1}{r}\frac{\partial}{\partial \theta}\tau_{\theta z} \approx \text{ one/rs(i)/hs*((vs(i,j,k)+vs(i,j,k+1)+vs(i,j+1,k)+vs(i,j+1,k+1)}$$

$$\text{+ve(i,j,k)+ve(i,j,k+1)+ve(i,j+1,k)+ve(i,j+1,k+1))/four}$$

$$\text{*((v(i,j,k+1)-v(i,j,k))/hz}$$

$$\text{+one/rs(i)/hs*(w(i,j+1,k)-w(i,j,k)))} \qquad \text{(A.12)}$$

$$\text{-(vs(i,j,k)+vs(i,j,k+1)+vs(i,j-1,k)+vs(i,j-1,k)}$$

$$\text{+ve(i,j,k)+ve(i,j,k+1)+ve(i,j-1,k)+ve(i,j-1,k))/four}$$

$$\text{*((v(i,j-1,k+1)-v(i,j-1,k))/hz}$$

+one/rs(i)/hs*(w(i,j,k)-w(i,j-1,k))))

$$\frac{\partial}{\partial z}\tau_{zz} \approx \text{one/hz*((vs(i,j,k+1)+ve(i,j,k+1))*two*(w(i,j,k+1)-w(i,j,k))/hz} \qquad \text{(A.13)}$$

-(vs(i,j,k)+ve(i,j,k))*two*(w(i,j,k)-w(i,j,k-1))/hz)

REFERENCES

E. Aulisa, S. Manservisi, R. Scardovelli, A mixed markers and volume-of-fluid method for the reconstruction and advection of interfaces in twp-phase and free-boundary flows, *J. Comput. Phys.* 188, 611-639 (2003)

B. S. Baldwin and H. Lomax, Thin-layer approximation and algebraic model for separated turbulent flows, *AIAA Paper* 78-257 (1978)

K.M. Becker and G. Hernborg, Measurements of burnout conditions for flow of boiling water in vertical annulus, *J. Heat Transfer*, **86**, 393-407 (1964)

C.-J. Chen and S.-Y. Jaw, Fundamentals of turbulence modeling, Taylor & Francis (1998)

R. Courant, E. Isaacson, M. Rees, On the solution of nonlinear hyperbolic differential equations by finite differences, *Comm. Pure Appl. Math*., **5**, 243-255 (1952)

Y. C. Chang, T. Y. Hou, B. Merriman, S. Osher, A level set formulation of Eulerian interface capturing methods for incompressible fluid flows, *J. Comput. Phys*. **124**, 449-464 (2001)

A. J. Chorin, Numerical solution of the Navier-Stokes equations, *Math. Comput*. **22**, 745-762 (1968)

D. Enright, R. Fedkiw, J. Ferziger, and I. Mitchell, A hybrid particle level set method for improved interface capturing, *J. Comput. Phys*. **183**, 83-116 (2002)

A. J. Chorin, Flame Advection and Propagation Algorithms, *J. Comput. Physis*, **35**, 1-11 (1980)

T. F. Dupont, Y. Liu, Back and forth error compensation and correction methods for removing errors induced by uneven gradients of the level set function, *J. Comput. Physis*, **190**, 311-324 (2003)

T. L. Durbin, Modeling dissolution in aluminum alloy, *Ph.D. Thesis*, Georgia Institute of Technology (2005)

J. H. Ferziger and M. Peric, Computational methods for fluid dynamics, 3rd edition, Springer (2002)

T. Fukano, T. Inatomi, Analysis of liquid film formation in a horizontal annular flow by DNS, *Int. J. Multiphase flow*, **29**, 1413-1430 (2003)

T. Furukawa and K. Sekoguchi, Phase distribution for air-water two-phase flow in annuli, *Bulletin of the JSME*, **29(**255), 3007-3014 (1986)

G. F. Hewitt and A. H. Govan, Phenomenological modeling of non-equilibrium flows with phase change, *Int. J. Heat Mass Transfer*, **33 (**2), 229-242 (1990)

J. Glimm, J. W. Grove, X. L. Li, K.-M. Shyue, Y. Zeng and Q. Zhang, Three dimensional front tracking, *SIAM J. Sci. Comput*. **19**, 703-727 (1998)

B. T. Helenbrook, L. Martinelli, and C. K. Law, A numerical method for solving incompressible flow problems with a surface of discontinuity, *J. Comput. Phys*. **148,** 366-396 (1999)

D. Jamet, O. Lebaigue, N. Coutris and J.M. Delhaye, The second gradient method for the direct numerical simulation of liquid-vapor flows with phase-change, *J. Comput. Phys*. **169**, 624-651 (2001)

W.P. Jones and B.E. Launder, The prediction of laminarization with a two-equation model of turbulence, *Int. J. of Heat and Mass Transfer*, **15**, 301-314 (1972)

D. Juric and G. Tryggvason, Computations of boiling flows, *Int. J. Multiphase Flow* **24,** 387-410 (1998)

I. Kataoka, S.Kodama, A.Tomiyama, A. Serizawa, Study on analytical prediction of forced convective CHF based on multi-fluid model, *Nuclear Engineering and Design*, **175**, 107-117 (1997)

T.Kim and M. Carlson, A simple boiling module, Eurographics/ACM SIGGRAPH Symposium on Computer Animation (2007)

P. Knabe and F. Wehle, Prediction of dryout performance for boiling water reactor fuel assemblies based on subchannel analysis with RINGS code, *Nuclear Technology*, **112**, 315-323 (1995)

B. E. Launder and B. I. Sharma, Application of the energy dissipation model of turbulence to the calculation of flow near a spinning disk, *Letters in Heat and Mass Transfer*, **1** (2), 131-138 (1974)

B. E. Launder and D. B. Spalding, *Mathematical models of turbulence*, Academic Press, London (1972)

F. R. Menter, Improved two-equation $k-\omega$ turbulence models for aerodynamic flows, NASA TM-103975 (1992)

F. R. Menter, Eddy viscosity transport equations and their relationships to the $k-\varepsilon$ model, NASA TM-108854 (1994)

T. Mitsutake, H. Terasaka, K. Yoshimura, M. Oishi, A. Inoue and M. Akiyama, Subchannel analysis of a critical power test, using simulated BWR 8X8 fuel assembly, *Nuclear Engineering and Design*, **122,** 235-254 (1990)

E.P. Mortimore and S.G. Beus, Critical heat flux experiments with a local heat patch in an internally heated annulus, WAPD-TM-1419 (1979)

J.Monaghan, Particle methods for hydrodynamics, *Comput. Phys. Rev*. 3, 71-124 (1985)

M. Naitoh, T. Ikeda, K. Nishida, T. Okawa and I. Kataoka, Critical power analysis with mechanistic models for nuclear fuel bundles, (I) models and verification for boiling water reactor application, *J. Nuclear Science and Technology,* **39**(1), 40-52 (2002)

W. Noh and P. Woodward, A simple line interface calculation, Proceedings, Fifth International Conference on Fluid Dynamics, Eds. A.I. vn de Vooran and P.J. Zandberger, Springer-Verlag, 1976

T. Okawa, A. Kotani, I. Kataoka, and M. Naito, Prediction of critical heat flux in annular flow using a film flow model, *J. of Nuclear Science and Technology*, **40**, No. 6, 388-396 (2003)

S. Osher and R.P. Fedkiw, Level set methods: An overview and some recent results, *J. Comput. Phys.* **169**, 463-502 (2001)

S. Osher and R. Fedkiw, Level set methods and dynamic implicit surfaces, Springer-Verlag, New York (2003)

S. Osher and J.A. Sethian, Fronts propagating with curvature-dependent speed: algorithms based on Hamilton-Jacobi formulations, *J. Coumput. Phys.* **79**, 12-49 (1988)

C.S. Peskin, Numerical analysis of blood flow in the heart, *J. Comput. Phys*. **25**, 220-252 (1977).

C.S. Peskin and D.M.McQueen, A general method for the computer simulation of biological systems interacting with fluids, *In SEB Symposium on Biological Fluid Dynamics*. Leeds, England (1994)

S. B. Pope, Turbulent flows, Cambridge University Press (2000)

L. Prandtl, Uber die ausgebildete turbulenz, *ZAMM* **5**, 136-139 (1925)

L. Prandtl, Ube rein neues Formelsystem fur die ausgebildete turbulenz, *Nacr. Akad. Wiss. Gottingen, Math-Phys, Kl*., 6-19 (1945)

E. G. Puckett, A volume-of-fluid interface tracking algorithm with applications to computing shock wave refraction, *Proceedings of the 4th international symposium on computational fluid dynamics*, Davis, California (1991)

J. Qian, G. Tryggvason, and C. K. Law, A front tracking method for the motion of premixed flames, *J. Comput. Phys*. **144,** 52-69 (1998)

R. Scardovelli and S. Zaleski, Direct numerical simulation of free-surface and interfacial flow*, Ann. Rev. Fluid Mech*. **31**, 567-603 (1999)

J.A.Sethian, Turbulent combustion in open and closed vessels, *J. Comput. Phys*. **54**, 425-456 (1984)

J.A. Sethian, Level set methods and fast marching methods, Cambridge University Press (1999)

S. Shin and D. Juric, Modeling three-dimensional multiphase flow using a level contour reconstruction method for front tracking without connectivity, *J. Comput. Phys*. **180**, 427-470 (2002).

S. Shin, S. I. Abdel-Khalik, V. Daru, and D. Juric, Accurate representation of surface tension using level contour reconstruction method, *J. Comput. Phys*, **203**, 493-516 (2005a)

S. Shin, S. I. Abdel-Khalik, and D. Juric, Direct three-dimensional numerical simulation of nucleate boiling using level contour reconstruction method, *Int. J. Multiphase Flow*, **31**, 1231-1242 (2005b)

S. Shin and S. I. Abdel-Khalik, Numerical modeling of evaporating thin liquid film instability on a heated cylindrical rod with parallel and cross vapor flow, *Nuclear Science and Engineering*, **156**, 24-39 (2007)

A.M.O. Smith and T. Cebeci, Numerical solution of the turbulent boundary-layer equations, Douglas Aircraft Division Report DAC 33735 (1967)

G. Son and V.K. Dhir, Numerical simulation of saturated film boiling near critical pressures with level set method, *J. Heat Trans.* **120,** 183-192 (1998)

P.R. Spalart and S. R. Allmaras, A one-equation turbulence model for aerodynamic flows, *AIAA Paper*, 92-439 (1992)

S. Sugawara and Y. Miyamoto, FIDAS: Detailed subchannel analysis code based on the three-fluid and three field model, *Nuclear Engineering and Design,* **120,** 147-161 (1990)

M. Sussman, E.G. Puckett, A coupled level set and volume-of-fluid method for computing 3D and axisymmetric incompressible two-phase flows, *J. Comput. Phys.* **162**, 301-337 (2000)

M. Sussman, P. Smereka and S. Osher, A level set method for computing solutions to incompressible two-phase flow, *J. Comput. Phys*. **114**, 146-159 (1994)

J. C. Tannehill, D. A. Anderson and R. H. Pletcher, Computational fluid mechanics and heat transfer, 2nd edition, Taylor & Francis (1997)

D. J. Torres and J. U. Brackbill, The point-set method: front tracking without connectivity, *J. Comput. Phys*. **165,** 620-644 (2000)

G. Tryggvason, B. Bunner, A. Esmaeeli, D. Juric, N. Al-Rawashi, W. Tauber, J. Han, S. Nas, and Y.- J. Jan, A front tracking method for the computations of multiphase flow, *J. Comput. Phys.* **169**, 708-759 (2001)

H. A. van der Vorst. Bi-CGSTAB: A fast and smoothly converging variant of Bi-CG for the solution of non-symmetric linear systems. *SIAM J. Sci. Statist. Comput.* **13**, 631-644 (1992)

E. R. Van Driest, On turbulent flow near a wall, *J. Aeronautical Sciences,***23,** 1007 (1956)

S. Welch and J. Wilson, A volume of fluid based method for fluid flows with phase change, *J. Comput. Phys*. **160,** 662-682 (2000)

D.C. Wilcox, Reassessment of the scale determining equation for advanced turbulence models, *AIAA Journal*, **26** (11), 1299-1310 (1988)

D. C. Wilcox, Turbulence modeling for CFD, 3rd Edition, DCW industries (2006)